ISSN: 2160-8881 Vol. 2, No. 3, September 2012

Scientific Research

Optics and Photonics Journal

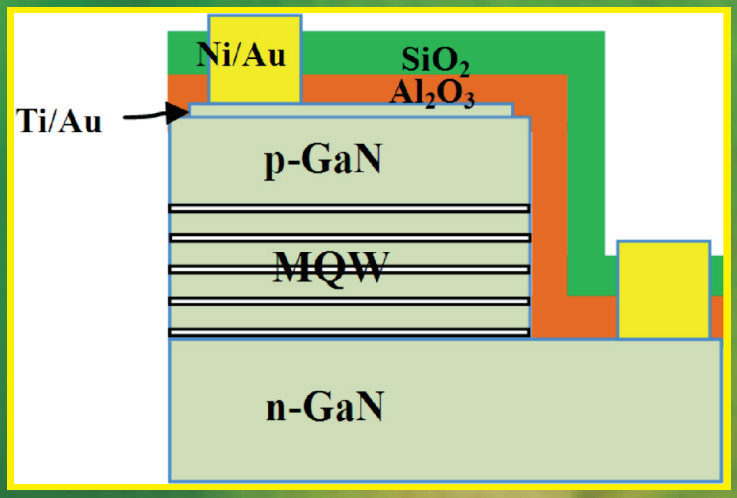

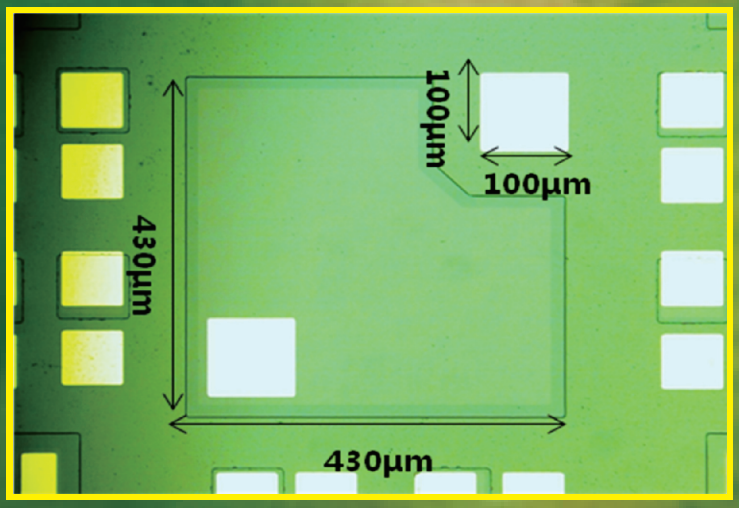

ISSN: 2160-8881

www.scirp.org/journal/opj

Journal Editorial Board

ISSN: 2160-8881 (Print), 2160-889X (Online)
http://www.scirp.org/journal/opj

Editor-in-Chief

Prof. Bouzid Menaa Fluorotronics Inc.,USA

Editorial Board

Dr. Claire Brown McGill University, Canada
Dr. Josep Canet-Ferrer Universitat de Valencia, Spain
Dr. Sharmistha Dutta Choudhury Bhabha Atomic Research Centre, India
Dr. Paul B. Crilly United States Coast Guard Academy, USA
Prof. Antonella D'Orazio Politecnico di Bari, Italy
Dr. Jacob Dunningham University of Leeds, UK
Dr. Tony Jun Huang Pennsylvania State University, USA
Prof. Mark Humphrey Australian National University, Australia
Dr. Rohan D. Kekatpure Sandia National Laboratories, Mexico
Prof. Sakhrat Khizroev Florida International University, USA
Dr. Sergey Kobtsev Novosibirsk State University, Russia
Prof. Sang Hak Lee Kyungpook National University, South Korea
Prof. Lev B. Levitin Boston University, USA
Dr. Jiang Li The Ohio State University, USA
Dr. Abbas Ali Lotfi-Nayestanak Telecommunication Engineering and IT Department, Iran
Prof. Mohd Adzir Mahdi Universiti Putra Malaysia, Malaysia
Prof. Patrick Meyrueis University of Strasbourg, France
Dr. Lim Nguyen University of Nebraska-Lincoln, USA
Dr. Frédéric Paul University of Rennes 1, France
Dr. Vincenzo Petruzzelli Politecnico di Bari, Italy
Dr. Neal T. Pfeiffenberger Virginia Tech, USA
Prof. Kuppuswamy Porsezian Pondicherry University, India
Dr. Chenggen Quan National University of Singapore, Singapore
Dr. Martins Rutkis Institute of Solid State Physics University of Latvia, Latvia
Prof. Victor I. Ryzhii University of Aizu, Japan
Dr. Felix Jaetae Seo Hampton University, USA
Dr. Alexey Yurievich Seteikin Amur State University, Russia
Dr. Haixia Shang University of Washington, USA
Dr. Mengtao Sun Institute of Physics, Chinese Academy of Sciences, China
Dr. Shuping Wang College of Engineering, University of North Texas, Denton, USA
Dr. Yong Wang CanaLaser Technologies Co., Ltd., China

Optics and Photonics Journal, 2012, 2, 135-199
Published Online September 2012 in SciRes (http://www.SciRP.org/journal/opj/)

TABLE OF CONTENTS

Volume 2 Number 3 September 2012

The figure on the front cover is from the article published in Optics and Photonics Journal, 2012, Vol. 2, No. 3, pp. 185-192 by Chung-Mo Yang, *et al.*

Copyright © 2012 SciRes.

Optics and Photonics Journal (OPJ)
Journal Information

SUBSCRIPTIONS

The *Optics and Photonics Journal* (Online at Scientific Research Publishing, www.SciRP.org) is published quarterly by Scientific Research Publishing, Inc., USA.

Subscription rates:

Print: $39 per issue.
To subscribe, please contact Journals Subscriptions Department, E-mail: sub@scirp.org

SERVICES

Advertisements
Advertisement Sales Department, E-mail: service@scirp.org

Reprints (minimum quantity 100 copies)
Reprints Co-ordinator, Scientific Research Publishing, Inc., USA.
E-mail: sub@scirp.org

COPYRIGHT

Copyright©2012 Scientific Research Publishing, Inc.

All Rights Reserved. No part of this publication may be reproduced, stored in a retrieval system, or transmitted, in any form or by any means, electronic, mechanical, photocopying, recording, scanning or otherwise, except as described below, without the permission in writing of the Publisher.

Copying of articles is not permitted except for personal and internal use, to the extent permitted by national copyright law, or under the terms of a license issued by the national Reproduction Rights Organization.

Requests for permission for other kinds of copying, such as copying for general distribution, for advertising or promotional purposes, for creating new collective works or for resale, and other enquiries should be addressed to the Publisher.

Statements and opinions expressed in the articles and communications are those of the individual contributors and not the statements and opinion of Scientific Research Publishing, Inc. We assumes no responsibility or liability for any damage or injury to persons or property arising out of the use of any materials, instructions, methods or ideas contained herein. We expressly disclaim any implied warranties of merchantability or fitness for a particular purpose. If expert assistance is required, the services of a competent professional person should be sought.

PRODUCTION INFORMATION

For manuscripts that have been accepted for publication, please contact:
E-mail: opj@scirp.org

Optics and Photonics Journal, **2012, 2, 135-139**
doi:10.4236/opj.2012.23019 Published Online September 2012 (http://www.SciRP.org/journal/opj)

Nonlinear Optical Studies of DNA Doped Rhodamine 6G-PVA Films Using Picosecond Pulses

Sasidharan Sreeja[1], Balan Nityaja[1], Debasis Swain[2], Vadakkedathu Parameswaran Narayana Nampoori[1], Padmanabhan Radhakrishnan[1], Soma Venugopal Rao[2*]

[1]International School of Photonics, Cochin University of Science and Technology, Cochin, India
[2]Advanced Centre of Research in High Energy Materials (ACRHEM), University of Hyderabad, Hyderabad, India
Email: [*]svrsp@uohyd.ernet.in, soma_venu@yahoo.com

Received May 30, 2012; revised June 28, 2012; accepted July 10, 2012

ABSTRACT

We present our results from the measurements of third-order optical nonlinearity in DNA doped Rhodamine 6G/PVA films achieved through Z-scan measurements using ~2 picosecond (ps) pulses at a wavelength of 800 nm. The films demonstrated negative nonlinear refractive index (n_2) with magnitudes of (0.065 - 2.89) × 10^{-14} cm^2/W with varying concentration of DNA. Open aperture data demonstrated strong two-photon absorption with a magnitude of ~1.6 cm/GW for films doped with 2 wt% of DNA. The recovery time of excited state population, retrieved from the degenerate pump-probe experimental data, was <4 ps. These data suggests that DNA is promising material for applications such as optical switching.

Keywords: DNA; Thin Films; Z-Scan; Picosecond; Two-Photon Absorption

1. Introduction

Deoxyribonucleic acid (DNA), a highly nonlinear bio-organic polymer, has been investigated as a photonic material recently with adequate success [1-14]. Biomaterials are interesting due to their remarkable properties which are not easily replicated with conventional organic or inorganic materials in the laboratory. Furthermore, natural biomaterials are a renewable resource and are inherently biodegradable [1]. Two DNA strands organize a DNA double helix through hydrogen bonds between the bases and are stabilized by π-π interactions [2]. DNA in solid-state (thin-film) form has unique combination of optical and electronic properties, which forms the foundation of DNA photonics [3,4]. This potentially viable organic polymer has established various applications in organic light emitting diodes (OLED), organic thin film transistors, polymer electro-optic modulators, polymer lasers etc. [5,6]. OLEDs containing DNA electron blocking layers have been recently reported [7] to exhibit significant enhancement in luminance and luminous efficiency [8]. DNA-CTMA thin films doped with Sulphorhodamine (SRh) have been reported to exhibit photoluminescence intensity more than an order of magnitude higher than that of SRh in PMMA [10]. Dye doped DNA media have demonstrated amplified spontaneous emission with pulsed laser excitation [11]. Sznitko *et al.* [13] successfully demonstrated amplified spontaneous emission and lasing action in deoxyribonucleic acid blended with cetyltrimethyl-ammonium chloride surfactant and doped with 3-(1,1-dicyanoethenyl1)-1phenyl-4,5dihydro-1H-pyrazole organic dye. Hanczyc *et al.* [14] observed remarkable multiphoton absorption properties of DNA intercalating ruthenium complexes: 1) [Ru(phen)2 dppz]2^+; 2) [(11,11'-bidppz)(phen)4Ru2]4^+; 3) [11,11'-bipb(phen)4Ru2]4^+ in the spectral range of 460 to 1100 nm. Nonlinear optical (NLO) properties of DNA in solution form [15] and in silica films [16] has been investigated recently. Our group recently reported the NLO properties of Rhodamine 6G-PVA solutions doped with DNA where we observed saturable absorption (SA) at lower concentration of DNA and switching behavior at higher concentrations [17]. We expect completely different performance in thin film form and with shorter pulse excitation since the intersystem crossing rates are much slower compared to the pulse duration [18]. Moreover, for any novel nonlinear optical (NLO) materials investigated, one needs to apprehend the linear absorption, nonlinear absorption, and nonlinear refractive index magnitudes (in various forms such as thin films) to establish their potential in appropriate fields of interest. Herein, we present results on the NLO properties of DNA doped Rh6G-PVA films with Z-scan technique using ~2 ps pulses recorded at a wavelength

[*]Corresponding author.

Copyright © 2012 SciRes.

of 800 nm. The sign and magnitude of nonlinear refractive index were derived from closed aperture Z-scan data. Open aperture Z-scan data revealed strong two photon absorption (TPA) in these films. Degenerate pumpprobe studies disclosed a fast response time of ~few ps.

2. Materials and Methods

We had used poly vinyl alcohol (PVA, Merck) for dissolving DNA and Rh6G. Since DNA and PVA are water soluble it is very easy to make thin films of DNA-PVA mixture. PVA solution acts a good matrix for hybridization of functional molecules and has excellent film forming, emulsifying, and adhesive properties. In the DNA-PVA system we have incorporated Rhodamine 6G owing to its high fluorescence quantum yield, low intersystem crossing rate, and little excited state absorption [18]. PVA solutions (8 wt%) were prepared by dissolving appropriate amount of PVA in distilled water at 800˚C under continuous stirring for 3 hr. Weighed DNA powder (SRL, extracted from herring sperm) was added to the prepared PVA solution. Rhodamine 6G dye was then added to PVA-DNA solution in desired concentration. After mixing (stirring) the solutions for 4 hr, thin films were fabricated on glass substrates using dip coating technique. Obtained films exhibited good optical transparency in the visible spectral range. The absorption spectra of prepared DNA films were characterized by using UV-VIS NIR spectrophotometer (Jasco V-570). Herewith, pure Rh6G-PVA films are denoted as R6GPVA, DNA 1 wt% doped films are denoted as DNA1, and DNA 2 wt% doped films are denoted as DNA2.

3. Experimental Techniques

NLO measurements were performed on DNA1, DNA2 films with thickness of ~100 μm. The Z-scan measurements [19] were performed using ~2 ps (FWHM, confirmed from independent autocorrelation experiments), 800 nm pulses with a repetition rate of 1 kHz from an amplified Ti:sapphire system (Legend, Coherent). The beam waist ($2\omega_0$) at focal plane was estimated to be ~60 μm (FW1/e^2M) with a corresponding Rayleigh range (Zr) of 3.5 ± 0.4 mm ensuring the validity of thin sample approximation. Complete details of the experimental set up can be found in our earlier publications [20-26].

4. Results and Discussion

Figure 1 illustrates the linear absorption spectra of DNA1 film and R6GPVA film. **Figure 1(a)** shows the presence absorption peak near 260 nm which is the characteristic of DNA. The peak is due to π-π^* (where π represents bonding orbitals and π^* represents anti-bonding orbitals) transition of the electrons of C=C bond in DNA bases [10]. The prominent absorption peak of Rh6G, near 532 nm, is evident from **Figure 1(b)**.

Figure 2 illustrates the open aperture Z-scan data for DNA1 [(a) and (b)] and DNA2 [(c) and (d)] with different peak intensities [110 GW/cm^2 for (a) and (c) 124 GW/cm^2 for (b) and (d)]. We observed strong reverse saturable absorption (RSA) kind of behavior in the intensity range mentioned above. For higher peak intensities the sample was damaged (confirmed through the discoloring of the film). Obtained experimental data were fitted using equations for two-photon absorption (2PA, β) [20-25]. Solid (blue) lines in all the figures indicate theoretical fits. The fits from **Figure 2(a)** (110 GW/cm^2) provided a 2PA coefficient of 0.45 cm/GW and **Figure 2(b)** (124 GW/cm^2) provided 2PA coefficient of 1.10 cm/GW for DNA1. The magnitude of β for DNA2 retrieved from the fits was 0.635 cm/GW for 110 GW/cm^2 and 1.61 cm/GW for 124 GW/cm^2. The magnitude of β in R6GPVA film was < 0.25 cm/GW.

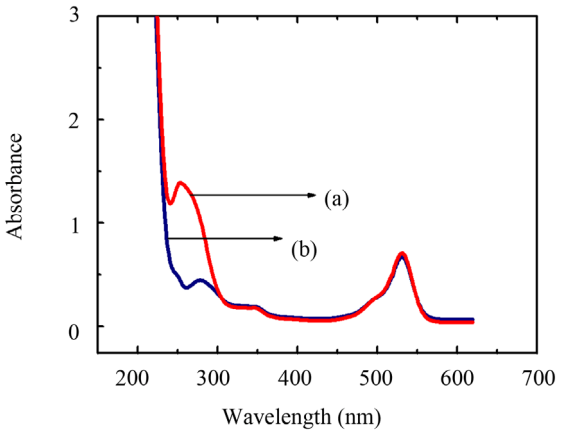

Figure 1. Absorption spectra and (a) DNA1 film (b) R6GPVA film.

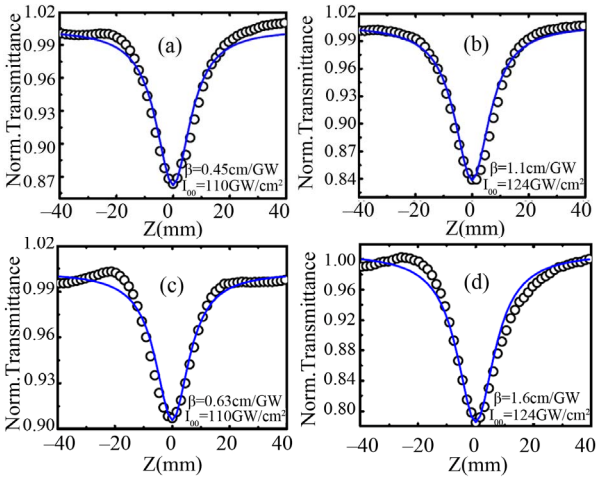

Figure 2. Open aperture Z scan curves for (a) DNA1, 110 GW/cm^2; (b) DNA1, 124 GW/cm^2; (c) DNA2, 110 GW/cm^2; and (d) DNA2, 124 GW/cm^2. Open circles indicate the experimental data while the solid (blue) lines indicate theoretical fits.

Copyright © 2012 SciRes.

Figures 3(a)-(c) demonstrate the typical closed aperture Z-scan curves obtained for DNA1, DNA2, and R6GPVA, respectively, recorded with a peak intensity of ~110 GW/cm^2. The data were fitted using standard equations [20-26]. It is apparent that all the samples demonstrated negative nonlinearity as indicated by the peak-valley signature. The magnitude of n_2 was ~4.61× 10^{-16} cm^2·W^{-1} for Rh6G doped PVA film. The magnitude of n_2 for DNA1 was ~6.5 × 10^{-15} cm^2·W^{-1} while for that of DNA2 was ~2.89 × 10^{-14} cm^2·W^{-1}. Both the magnitudes were higher than that of n_2 recorded in R6GPVA. Enhancement in n_2 can be attributed to increase of charge transfer, which takes place in the system and is due to the presence of many highly polarizable conjugated π electrons of DNA [17]. Moreover, the interactions due to intercalation into base pair stack at the core of double helix and/or insertion into the minor groove of DNA are documented to have strong impact on the optical characteristics. The magnitudes of n_2 (10^{-14} cm^2·W^{-1}) obtained here are at least one order higher than those obtained in solution form (10^{-14} cm^2·W^{-1}) using femtosecond pulses [15]. The magnitudes of 2PA coefficient obtained (1.61 cm/GW) are again higher than those obtained (0.2 cm/GW) in solutions [15]. Krupka *et al.* [27] obtained purely electronic, fast NLO susceptibility in a DNA-CTMA complex thin film with a third-order nonlinear optical susceptibility magnitude of 10^{-14} e.s.u. In our case the magnitudes of $\chi^{(3)}$ (third order nonlinear optical susceptibility) were estimated to be 8.45 × 10^{-13} e.s.u. for DNA1 and 2.72 × 10^{-12} e.s.u. for DNA2, respectively.

We had also performed the degenerate pump probe studies of DNA doped Rh6G + PVA films using ~2 ps pulses to evaluate the time response of the nonlinearity. Details of the experimental setup can be found in our earlier reference [23]. **Figure 4** shows the data obtained indicating photo-induced absorption. A sharp fall in ΔT was observed near zero delay followed by a quick recovery. The recovery time of population from the excited states was estimated to be ~4.2 ps. The obtained lifetime is in agreement with the non-radiative decay times observed in DNA model systems measured by Kohler *et al.* [28] using ultrashort pulses. Our future studies will focus on evaluating the nonlinearities at different wavelengths in the visible/near-IR spectral regions.

5. Conclusion

To summarize, we deliberated the NLO properties of thin films of Rhodamine 6G, doped with DNA, obtained using ps pulses. The addition of DNA enhanced the NLO properties of thin films. We identified that the films demonstrated negative n_2 with a highest magnitude of 2.89 × 10^{-14} cm^2/W for DNA2 films. Open aperture data demonstrated strong 2PA with a highest magnitude of ~1.6 cm/GW, again for DNA2 films. Ultrafast response obtained from pump-probe experiments suggests that this-material has potential for applications in photonics. We conclude that PVA is a good matrix for fluorescent dyes incorporated into the double helix of DNA molecule enabling them suitable for practical applications in optical devices.

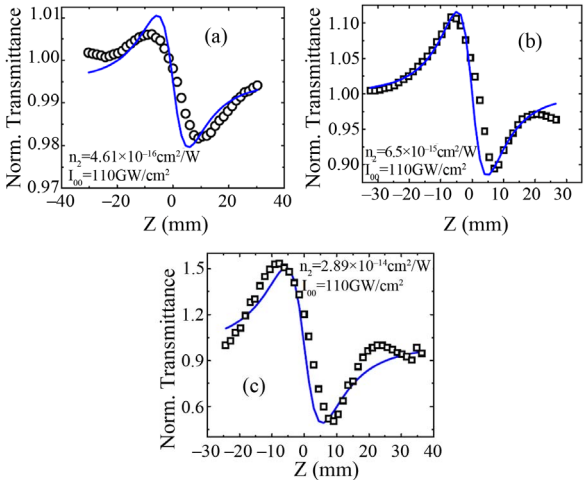

Figure 3. Closed aperture Z-scan curves for (a) R6GPVA film, (b) DNA1 film, and (c) DNA2 film. Circles/squares represent the data while the solid (blue) lines indicate theoretical fits.

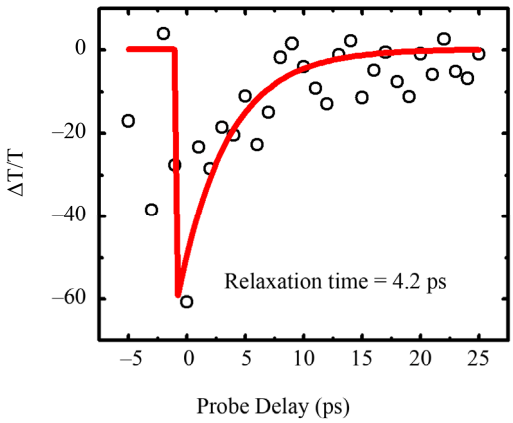

Figure 4. Degenerate pump-probe data of DNA2 film recorded at 800 nm.

6. Acknowledgements

Financial support from DRDO is greatly acknowledged. S. Sreeja acknowledges UGC for the financial assistance.

REFERENCES

[1] P. N. Prasad, "Introduction to Bio-Photonics," Wiley, New York, 2003.

[2] N. Kitazawa, S. Miyagawa, K. Date, W. Aroonjaeng, M. Aono and Y. Watanabe, "Optical Properties of Dye-Doped Deoxyribonucleic Acid Films," *Journal of Materials Science*, Vol. 44, No. 18, 2009, pp. 4999-5003.

Copyright © 2012 SciRes.

doi:10.1007/s10853-009-3764-5

[3] A. J. Steckl, "DNA—A New Material for Photonics?" *Nature Photonics*, Vol. 1, No. 1, 2007, pp. 3-5. doi:10.1038/nphoton.2006.56

[4] J. G. Grote, E. M. Heckman, D. Diggs, J. A. Hagen, P. Yaney, A. J. Steckl, G. S. He, Q. Zheng, P. N. Prasad, J. Zetts and F. K. Hopkins, "DNA-Based Materials for Electro-Optic Applications," *Proceedings of SPIE*, Vol. 5934, 2005, pp. 38-43. doi:10.1117/12.615206

[5] A. J. Steckl, H. Spaeth, H. You, E. Gomez and J. Grote, "DNA as an Optical Material," *Optics and Photonics News*, Vol. 22, No. 7, 2011, pp. 34-39. doi:10.1364/OPN.22.7.000034

[6] A. J. Steckl, A. Hagen, Z. Yu, R. A. Jones, W. Li, D. Han, D. Y. Kim and H. Spaeth, "Challenges and Opportunities for Biophotonic Devices in the Liquid State and the Solid State," *IEEE Nanotechnology Conference*, Vol. 1, 2006, pp. 159-161. doi:10.1109/NANO.2006.247596

[7] J. A. Hagen, W. Li and A. J. Steckl and J. G. Grote, "Enhanced Emission Efficiency in Organic Light-Emitting Diodes Using Deoxyribonucleic Acid Complex as an Electron Blocking Layer," *Applied Physics Letters*, Vol. 88, No. 17, 2006, Article ID: 171109. doi:10.1063/1.2197973

[8] Z. Yu, W. Li, J. A. Hagen, Y. Zhou, D. Klotzkin, J. G. Grote and A. J. Steckl, "Photoluminescence and Lasing from Deoxyribonucleic Acid (DNA) Thin Films Doped with Sulforhodamine," *Applied Optics*, Vol. 46, No. 9, 2007, pp. 1507-1513. doi:10.1364/AO.46.001507

[9] Y. Kawabe, L. Wang, S. Horinouchi and N. Ogata, "Amplified Spontaneous Emission from Fluorescent-Dye-Doped DNA—Surfactant Complex Films," *Advanced Materials*, Vol. 12, No. 17, 2000, pp. 1281-1283. doi:10.1002/1521-4095(200009)12:17<1281::AID-ADMA1281>3.0.CO;2-0

[10] J. Grote, D. Y. Zang, F. Ouchen, G. Subramanyam, P. Yaney, C. Bartsch, E. Heckman and R. Naik, "Progress of DNA Photonics," *Proceedings of SPIE*, Vol. 7765, 2010, Article ID: 776502. doi:10.1117/12.862160

[11] N. Balan, M. Hari and V. P. N. Nampoori, "Selective Mode Excitation in Dye-Doped DNA Polyvinyl Alcohol Thin Film," *Applied Optics*, Vol. 48, No. 19, 2009, pp. 3521-3525. doi:10.1364/AO.48.003521

[12] B. Sahraoui, M. Pranaitis, D. Gindre, J. Niziol and V. Kažukauskas, "Opportunities of Deoxyribonucleic Acid Complexes Composites for Nonlinear Optical Applications," *Journal of Applied Physics*, Vol. 110, No. 8, 2011, Article ID: 083117. doi:10.1063/1.3655985

[13] L. Sznitko, J. Mysliwiec, P. Karpinski, K. Palewska, K. Parafiniuk, S. Bartkiewicz, I. Rau, F. Kajzar and A. Miniewicz, "Biopolymer Based System Doped with Non-Linear Optical Dye as a Medium for Amplified Spontaneous Emission and Lasing," *Applied Physics Letters*, Vol. 99, No. 3, 2011, Article ID: 031107. doi:10.1063/1.3610566

[14] P. Hanczyc, B. Norden and M. Samoc, "Two-Photon Absorption of Metal-Organic DNA-Probes," *Dalton Transactions*, Vol. 41, No. 11, 2012, pp. 3123-3125. doi:10.1039/c2dt12264b

[15] M. Samoc, A. Samoc and J. G. Grote, "Complex Nonlinear Refractive Index of DNA," *Chemical Physics Letters*, Vol. 431, No. 1-3, 2006, pp. 132-134. doi:10.1016/j.cplett.2006.09.057

[16] B. Sahraoui, M. Pranaitis, K. Iliopoulos, M. Mihaly, A. F. Comanescu, M. Moldoveanu, I. Rau and V. Kažukauskas, "Enhancement of Linear and Nonlinear Optical Properties of Deoxyribonucleic Acid-Silica Thin Films Doped with Rhodamine," *Applied Physics Letters*, Vol. 99, No. 24, 2011, Article ID: 243304. doi:10.1063/1.3669406

[17] B. Nithyaja, H. Misha, P. Radhakrishnan and V. P. N. Nampoori, "Effect of Deoxyribonucleic Acid on Nonlinear Optical Properties of Rhodamine 6G-Polyvinyl Alcohol Solution," *Journal of Applied Physics*, Vol. 109, No. 2, 2011, Article ID: 023110. doi:10.1063/1.3520657

[18] C. V. Bindhu, S. S. Harilal, V. P. N. Nampoori and C. P. G. Vallabhan, "Studies of Nonlinear Absorption and Aggregation in Aqueous Solutions of Rhodamine 6G Using Transient Thermal Lens Technique," *Journal of Physics D*: *Applied Physics*, Vol. 32, No. 4, 1999, pp. 407-411. doi:10.1088/0022-3727/32/4/009

[19] M. Sheik-Bahae, A. A. Said, T. H. Wei, D. J. Hagan and E. W. Van Stryland, "Sensitive Measurement of Optical Nonlinearities Using a Single Beam," *IEEE Journal of Quantum Electronics*, Vol. 26, No. 4, 1999, pp. 760-769. doi:10.1109/3.53394

[20] S. Venugopal Rao, T. Shuvan Prashant, T. Sarma, P. K. Panda, D. Swain and S. P. Tewari, "Two-Photon and Three-Photon Absorption in Dinapthoporphycenes," *Chemical Physics Letters*, Vol. 514, No. 1-3, 2011, pp. 98-103. doi:10.1016/j.cplett.2011.08.021

[21] S. Venugopal Rao, "Large Picosecond Nonlinearity in Gold Nanoparticles Synthesized Using Coriander Leaves (*Coriandrum sativum*)," *Journal of Modern Optics*, Vol. 58, No. 12, 2011, pp. 1024-1049. doi:10.1080/09500340.2011.590903

[22] P. T. Anusha, P. Silviya Reeta, L. Giribabu, S. P. Tewari and S. Venugopal Rao, "Picosecond Optical Nonlinearities of Unsymmetrical Alkyl and Alkoxy Phthalocyanines Studied Using the Z-Scan Technique," *Materials Letters*, Vol. 64, No. 17, 2010, pp. 1915-1917. doi:10.1016/j.matlet.2010.06.004

[23] D. Swain, P. T. Anusha, T. Shuvan Prashant, S. P. Tewari, T. Sarma, P. K. Panda and S. Venugopal Rao, "Ultrafast Excited State Dynamics and Dispersion Studies of Nonlinear Optical Properties in Dinaphthoporphycenes," *Applied Physics Letters*, Vol. 100, No. 14, 2012, Article ID: 141109. doi:10.1063/1.3701274

[24] S. Hamad, S. P. Tewari, L. Giribabu and S. Venugopal Rao, "Picosecond and Femtosecond Optical Nonlinearities of Novel Corroles," *Journal of Porphyrins and Phthalocyanines*, Vol. 16, No. 1, 2012, pp. 140-148. doi:10.1063/1.3643648

[25] K. Venkata Saravanan, K. C. James Raju, M. Ghanashyam Krishna, S. P. Tewari and S. Venugopal Rao, "Large Three-Photon Absorption in $Ba_{0.5}Sr_{0.5}TiO_3$ Films Studied Using Z-Scan Technique," *Applied Physics Letters*, Vol. 96, No. 23, 2010, Article ID: 232905. doi:10.1063/1.3447930

Copyright © 2012 SciRes.

[26] G. Krishna Podagatlapalli, S. Hamad, S. Sreedhar, S. P. Tewari and S. Venugopal Rao, "Fabrication and Characterization of Aluminum Nanostructures and Nanoparticles Obtained Using Femtosecond Ablation Technique," *Chemical Physics Letters*, Vol. 530, 2012, pp. 93-97. doi:10.1016/j.cplett.2012.01.081

[27] O. Krupka, A. El-Ghayoury, I. Rau, B. Sahraoui, J. G. Grote and F. Kajzar, "NLO Properties of Functionalized DNA Thin Films," *Thin Solid Films*, Vol. 516, No. 24, 2008, pp. 8932-8936. doi:10.1016/j.tsf.2007.11.089

[28] B. Kohler, "Nonradiative Decay Mechanisms in DNA Model Systems," *Journal of Physical Chemistry Letters*, 1, No. 13, 2010, pp. 2047-2053. doi:10.1021/jz100491x

Copyright © 2012 SciRes.

Optics and Photonics Journal, **2012, 2, 140-144**
doi:10.4236/opj.2012.23020 Published Online September 2012 (http://www.SciRP.org/journal/opj)

Effect of the Doping Layer Concentration on Optical Absorption in Si δ-Doped GaAs Layer

Hassen Dakhlaoui
Department of Physics, Faculty of Science Bizerte, Bizerte City, Tunsia
Email: h_dakhlaoui@yahoo.fr

Received June 15, 2012; revised July 19, 2012; accepted July 29, 2012

ABSTRACT

We study in this paper the intersubband optical absorption of Si δ-doped GaAs layer for different applied electric fields and donors concentration. The electronic structure has been calculated by solving the Schrödinger and Poisson equations self-consistently. From our results, it is clear that the subband energies and intersubband optical absorption are quite sensitive to the applied electric field. Also our results indicate that the optical absorption depends not only on the electric field but also on the donor's concentration. The results of this work should provide useful guidance for the design of optically pumped quantum well lasers and quantum well infrared photo detectors (QWIPs).

Keywords: δ-Doped GaAs; Self-Consistently; The Intersubband Absorption

1. Introduction

Si δ-doped semiconductor structures have been of great interest because of their technological utility in electronic and photonic devices [1,2]. In these structures, a layer of Si atoms provides electron and gives rise to quantum subbands. By this means, a two-dimensional electron gaz can be obtained by planar doping of GaAs at high donors concentration. Hence there is great interest in a good understanding of Si δ-doped as a representative example of those devices. Theoretical studies of the above systems usually neglect possible effects of disorder due to the random distribution of impurities in order to simplify the analysis. Indeed, currently available techniques allow for an optimal control of the growing heterostructures, thus justifying the assumption that the ionized impurity atoms are homogeneously distributed inside the δ-doped layers. This approximation has recently been shown to be correct in the high density limit [3]. A number of researches have considered this limit within different approaches, like the Thomas-Fermi [4], local density approximation (LDA) [5] and Hartree methods [6]. These previous works show that in the absence of external fields the Thomas-Fermi semiclassical approach is equivalent to a self-consistent formulation over a wide range of doping concentrations [4]. The effects of applied electric field have recently been considered in the case of single and periodically Si δ-doped GaAs [7,8] by using a generalized Thomas-Fermi formalism. The electric field dependence of the intersubband optical absorption is also interesting for potential device applications. Intersubband absorption in quantum wells have been proposed or demonstrated experimentally to be very useful for far-infrared detectors [9,10], electro-optical modulators [11,12], and infrared lasers [13]. One of the most remarkable feature of 2DEG is the intersubband optical transitions between the size quantized subbands in the same band. The behavior of an excited quantum well under the influence of an external electric field has been studied before [14, 15]. Also for intersubband absorption, doping is very important to provide the carriers for the ground subband. The intersubband optical absorption in quantum well structures [16,17] and in δ-doped semiconductors has been studied before [18-20].

In the present paper, we investigate theoretically the electronic structure of Si δ-doped GaAs using a self-consistent procedure to solve Schrödinger and Poisson equations simultaneously. We have studied the influence of the electric field on the intersubband optical absorption. In addition to the electric field we studied the effect of the donor's concentration on the optical absorption; we conclude that the intersubband transitions are quite sensitive not only to the applied electric field but also to the donor's concentrations.

2. The Model

For calculations which describe the structure, the self-consistent solution of the Schrödinger and Poissson equations in the effective mass approximation was used. The material studied was GaAs with Si δ-doped layer. The wave function of electrons were decoupled into free par-

Copyright © 2012 SciRes.

ticule waves in the plane (x, y) and the bound state in the z-direction. The structure was modelled assuming uniform distribution of the donors in the δ- doped layer. Free electrons are captured in the neighbourhood of parent ions by electrostatic interaction. The result of this interaction is the formation of quasi-two-dimensional electron gas around the dopant slab where electrons are free to move in the planes of doping and their motion is bound and quantized in the perpendicular direction. We assume the validity of the effective-mass approximation and take an isotropic and parabolic conduction band in the growth direction. This approximation usually works fine in GaAs. In the envelope function approach, the electronic wavefunction corresponding to the jth subband may be factorized as follows [21]:

$$\psi_j(r) = \frac{1}{\sqrt{S}} \exp(ik_\perp \cdot r_\perp) \psi_j(z) \tag{1}$$

where $k_\perp$ and $r_\perp$ are the in-plane wave vector and spatial coordinates, respectively. Here S is the area of the layer. The subband energy follows the parabolic dispersion law $E_j + \hbar^2 k_\perp^2 / 2m^*$, m^* being the electron effective mass at the bottom of the conduction band (Γ valley). The quantized energy levels E_j and their corresponding envelope functions $\psi_j(z)$ satisfy the following Schrodinguer-like equation:

$$\left(-\frac{\hbar^2}{2m^*} \frac{\mathrm{d}^2}{\mathrm{d}z^2} + v(z) \right) \psi_j(z) = E_j \psi_j(z). \tag{2}$$

The one electron potential splits into three different contributions:

$$V(z) = V_H(z) + Vxc(z) + eFz. \tag{3}$$

The last term in equation is the potential of an external electrical field. The Hartree potential is a result of the electrostatic interaction of electrons with themselves and with ionized dopants. It can be found by solving the one dimensional Poisson-equation,

$$\frac{\mathrm{d}^2 V_H(z)}{\mathrm{d}z^2} = \frac{e}{\varepsilon_0 \varepsilon_k} \left[N_D - n(z) \right] \tag{4}$$

where the elecron density $n(z)$ is given as

$$n(z) = \sum_J n_j \left| \psi_j(z) \right|^2. \tag{5}$$

And the sum goes over the sub-bands. The number of electrons per unit area in the jth sub-band can be calculated as

$$n_j = \frac{m^* K_B T}{\pi \hbar^2} \ln \left[1 + \exp\left(\frac{E_F - E_j}{K_B T} \right) \right], \tag{6}$$

where E_F is the Fermi energy. The exchange and correlation potential V_{xc} was found according to the Hedin and Lundquist parametrization,

$$V_{xc}(z) = -\frac{R_y^*}{10.5 \pi \alpha r} \left[1 + 0.773 r \ln\left(1 + r^{-1} \right) \right] \tag{7}$$

where $\alpha = (4/9\pi)^{1/3}$, $r = \frac{1}{21} \left[\frac{4}{3} \pi a^* n(z) \right]^{-1/3}$, and $R_y = e^2 / 8\pi\varepsilon_0 \kappa a^* \approx 5meV$ is the effective Rydberg constant and $a^* = 4\pi\varepsilon_0 \kappa \hbar^2 / m^* e^2 \approx 100$ Å is the effective Bohr radius. The solutions of these equations give us the sub-band energy levels, the effective confining potential and also the charge density profiles. The calculation also yields self-consistently the position of the Fermi level E_f, from the condition that the total number of electrons must equal the total number of donors, *i.e.* $n_i = N_D$. All donors are assumed to be ionized and are replaced by uniform distribution. We have solved the Equations (2)-(7) self consistently using the finite difference technique. After the subband energies and their corresponding wave functions is obtained, the linear absorption coefficient $\sum_i \alpha(\omega)$ for the intersubband transitions can be clearly calculated as,

$$\begin{aligned} \alpha(\omega) = {} & \frac{\omega \mu c e^2}{n_r} \left| M_{fi} \right|^2 \frac{m^* K_B T}{L_{\mathrm{eff}} \pi \hbar^2} \\ & \times \ln \left\{ \frac{1 + \exp\left[(E_F - E_i) / K_B T \right]}{1 + \exp\left[(E_F - E_f) / K_B T \right]} \right\} \\ & \times \frac{\hbar / \tau_{in}}{(E_F - E_i - \hbar\omega)^2 + (\hbar / \tau_{in})^2} \end{aligned} \tag{8}$$

with the matrix element

$$M_{fi} = \int_{-L/2}^{L/2} \psi_f^*(z) z \psi_i(z) \mathrm{d}z, \tag{9}$$

where $E_{fi} = E_f - E_i$, E_f and E_i denote the quantized energy levels for the final and initial states, respectively, μ is the permeability, C is the speed of light in free space, L_{eff} is the effective spatial extent of electrons in subbands, n_r is the refractive index, τ_{in} is the intra-subband relaxation time (where τ_{in} is a constant and used the numerical value of 0.14 ps following Ref. [14]).

3. Results and Discussion

3.1. Effect of Electric Field on Optical Absorption

In our numerical simulations, the thickness of GaAs structure is L = 50 nm. The δ-doped layer (2 nm) is assumed to be inserted into an infinite quantum well. The calculations were done for the temperature T = 295 K. The boundary conditions are $\psi(0) = \psi(L) = 0$. The effective

Copyright © 2012 SciRes.

mass of the electron has been taken as ($m^* = 0.067\, m_0$), m_0 being the free electron mass. **Figures 1(a)-(c)** show us the absorption coefficient as a function of the photon energy for different electric field intensities. It is clear from **Figure 1(a)** that in absence of electric field one notices the existence only of the following transitions: (1-2); (2-3); (3-4) and one can easily see that the (1-2) intersubband transition is dominant. However this situation changes when the electric field intensity increases. From **Figure 1(b)** the dominant transition is (3-4) and the maximum of the (1-2) transition decreases. We can note also

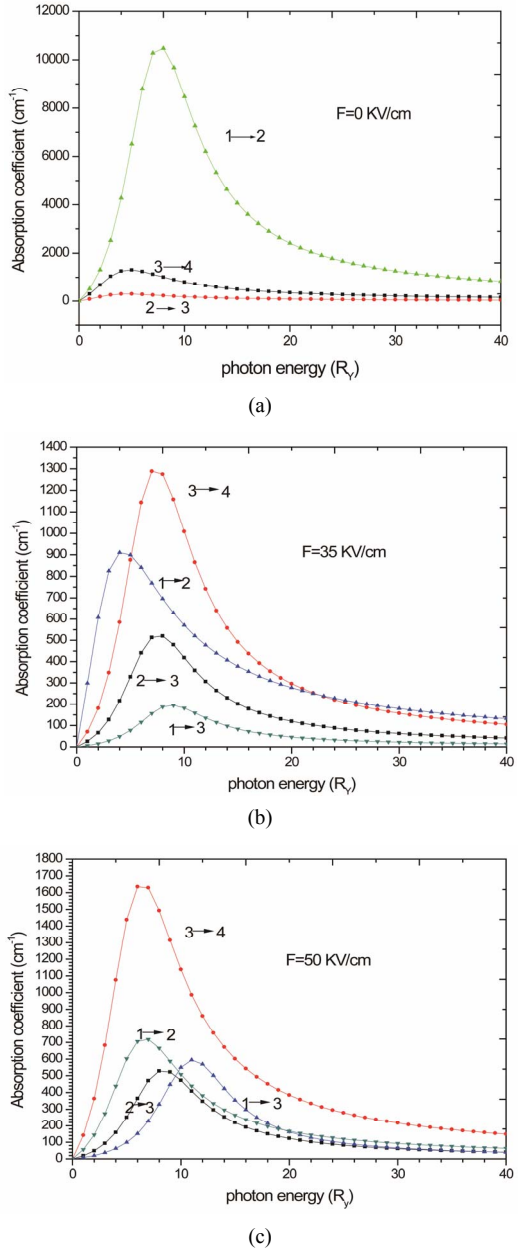

Figure 1. The variation of the absorption coefficient as a function of the photon energy for different intersubband transitions for (a) F = 0 KV/cm; (b) F = 35 KV/cm; (c) F = 50 KV/cm.

that the forbidden transition (1-3) when $F = 0$ KV/cm becomes possible when $F = 35$ KV/cm . **Figure 1(c)** show us that more and more the electric field intensity increases more that the transitions (3-4), (1-3) and (2-3) increases whereas the transition (1-2) decreases. The results stated above can be explained as follows: In absence of an applied electric field the confining potential presents V-shape profile and the envelope wavefunctions are symmetric around the doped layer, in this case the transition (1-3) is forbidden. However when the electric field intensity increases the confining potential becomes slightly asymmetric, in other words the confining potential change its shape and a secondary quantum well appears at the left (**Figure 2**) [22,23]. The excited subbands energies decrease because the asymmetric structures, the higher subband energies, which are more energetic, can easily, penetrate into the secondary quantum well and, thus their energies decrease.

Figure 3 shows the absorption coefficient (1-2) for different applied electric field intensities. It is clear from this figure that when the electric field intensity increases the maximum of absorption decreases, this decrease in

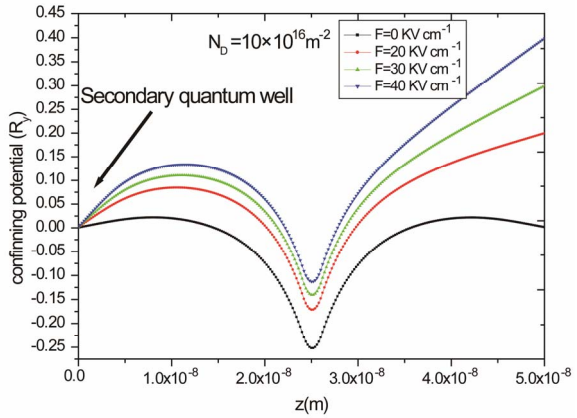

Figure 2. The self consistent confining potential for different electric field intensities.

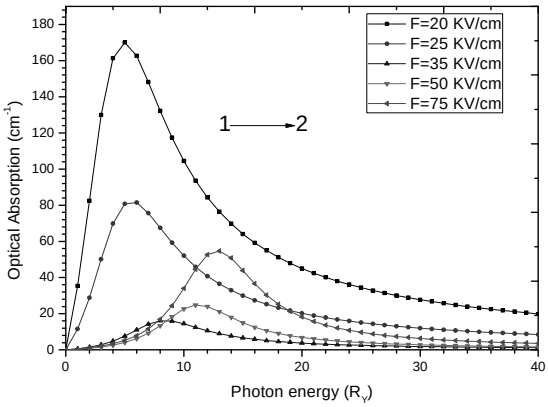

Figure 3. The absorption coefficient of (1-2) intersubband transition for different applied electric field intensities.

Copyright © 2012 SciRes.

absorption is observed for small applied electric field intensity $F < 35$ KV/cm. However for high applied electric field $F > 35$ KV/cm this maximun in absorption coefficient increases with increasing the intensity of applied electric field.

3.2. Effect of Doping Layer Concentration on Optical Absorption

To illustrate the effect of the concentration on the properties of our structure one starts with representing the confining potential for various doping layer concentration N_D (**Figure 4**). With increasing the value of the concentration N_D the potential becomes more and more deep what improves the confinement of the electrons. We have also study the effect of the concentration N_D on the absorption coefficient of the (1-2) intersubband transition (**Figure 5**). As seen from this figure, while for small concentration range ($N_D < 3\times10^{16}$ m^{-2}) the absorption peak increases with increasing the value of N_D, however for high concentration rang $N_D > 3\times10^{16}$ m^{-2} this peak decreases in magnitude with increasing electric field. Because the high N_D concentration generate a deeper potential of confinement (**Figure 4**) and therefore the levels of energies will be nearer one of the other what decreases the absorption coefficient. Therefore one can say that the concentration of the doping layer can serve to adjust the value of the desired absorption coefficient.

In **Figure 6** we plot the energy difference between the ground and the first excited subband, $\Delta E = E_2 - E_1$ as a function of the doping layer concentration N_D, from this figure we note that this difference between the two ener- gies decreases for $N_D < 3\times10^{16}$ m^{-2} range and increases for the $N_D > 3\times10^{16}$ m^{-2}. This result confirms the value of this concentration limits $N_D(\text{limit}) = 3\times10^{16}$ m^{-2} found in the previous paragraph (**Figure 5**). The results open the possibility to design devices for use as optical filters controlled by doping layer concentration.

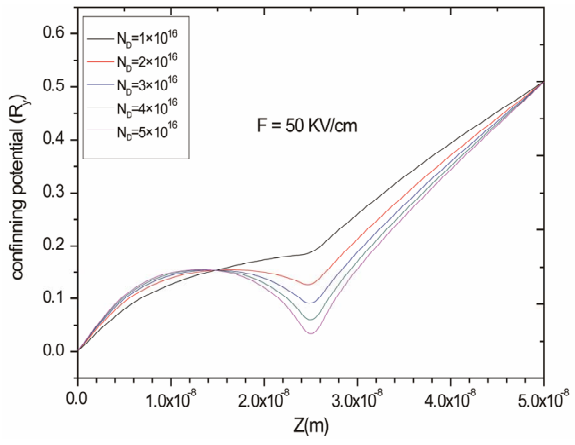

Figure 4. Confining potential for various doping layer concentration N_D.

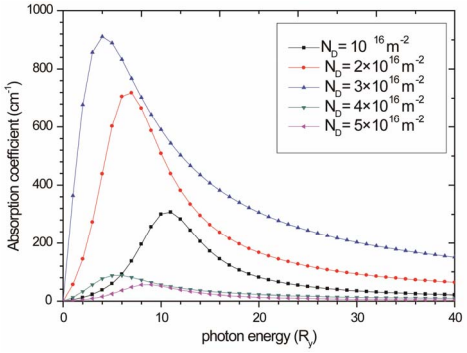

Figure 5. The absorption coefficient of (1-2) intersubband transition for different concentration N_D of the doped layer.

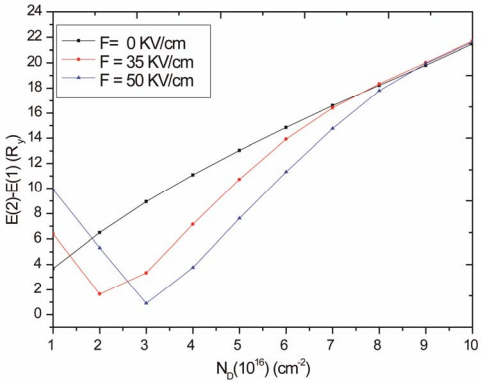

Figure 6. Energy difference between the ground and the first excited as a function of the doping layer concentration.

4. Conclusion

We have investigated the intersubband optical absorption of Si δ-doped GaAs for different applied electric fields and various concentrations of the doping layer using a self-consistent procedure to solve the Schrödinger and Poisson equations. From our results, it is clear that the subband energies and intersubband optical absorption is quite sensitive to the applied electric field. Also our results indicate that the optical absorption depends not only on the electric field but also on the doping layer concentration. Such systems are extremely attractive from the point view of both basic research and technological application, such as, optical modulators, high-power FETs, and infrared devices based on the intersubband transition of electrons.

REFERENCES

[1] E. F. Schubert, A. Fischer and K. Ploog, "The Delta-Doped Field-Effect Transistor," *IEEE Transactions on Electron Devices*, Vol. 33, No. 5, 1986, pp. 625-632. doi:10.1109/T-ED.1986.22543

[2] K. Ploog, M. Hauser and A. Fischer, "Fundamental Studies and Device Application of δ-Doping in GaAs Layers and in $Al_xGa_{1-x}As$/GaAs Heterostructures," *Applied Phy-*

Copyright © 2012 SciRes.

sics A: *Materials Science & Processing*, Vol. 45, No. 3, 1988, pp. 233-244. doi:10.1007/BF00615010

[3] J. Kortus and J. Monecke, "Formation of Subbands in δ-Doped Semiconductors," *Physical Review B*, Vol. 49, No. 24, 1994, pp. 17216-17223.

[4] L.Ioratti, "Thomas-Fermi Theory of δ-Doped Semiconductor Structures: Exact Analytical Results in the High Density Limit," *Physical Review B*, Vol. 41, No. 12, 1990, pp. 8340-8344.

[5] M. H. Degani, "Energy Electron Levels in a δ-Doped Layer in GaAs," *Physical Review B*, Vol. 44, No. 11, 1991, pp. 5580-5584.

[6] A. Zrenner, F. Koch and K. Ploog, "Subband Physics for a 'Realistic' δ-Doping Layer," *Surface Science*, Vol. 196, No. 1-3, 1988, pp. 671-676.

[7] F. Dominguez-Adame, B. Mendez and E. Macia, "Electronic Structure of Si Delta-Doped GaAs in an Electric Field," *Semiconductor Science and Technology*, Vol. 9, No. 3, 1991, p. 263.

[8] F. Dominguez-Adame and B. Mendez, "Stark Ladders in Periodically Si-δ-Doped GaAs," *Physical Review B*, Vol. 49, No. 16, 1994, p. 11471.

[9] X. Zheng, T. K. Carns, K. L. Wang and B. Wu, "Electron Mobility Enhancement from Coupled Wells in Delta-Doped GaAs," *Applied Physics Letters*, Vol. 62, No. 5, 1993, pp. 504-507. doi:10.1063/1.108893

[10] R. J. Turton and M. Jaros, "Intersubband Optical Transitions in Si-$Si_{0.5}Ge_{0.5}$," *Applied Physics Letters*, Vol. 54, No. 20, 1989, pp. 1986-1988. doi:10.1063/1.101190

[11] D. Ahn and S. L. Chuang, "Intersubband Optical Absorption in Quantum Well with an Applied Electric Field," *Physical Review B*, Vol. 35, No. 8, 1987, p. 4149. doi:10.1103/PhysRevB.35.4149

[12] D. Ahn and S. L. Chuang, "Exact Calculations of Quasi-bound States of an Isolated Quantum Well with Uniform Electric Field: Quantum-Well Stark Resonance," *Physical Review B*, Vol. 34, No. 12, 1986, pp. 9034-9037. doi:10.1103/PhysRevB.34.9034

[13] R. F. Kazarinov and R. A. Suris, "Possibility of the Amplification of Electromagnetic Waves in a Semiconductor with a Superlattice," *Soviet Physics—Semiconductors*, Vol. 5, No. 4, 1971, p. 707.

[14] D. Ahn and S. L. Chuang, "Optical Transitions in a Parabolic Quantum Well with an Applied Electric Field-Analytical Solutions," *IEEE Journal of Quantum Electronics*, Vol. 23, No. 12, 1987, p. 2196.

[15] C. T. Giner and J. L. Gondar, "Exact Wave Functions and Energy Levels for a Quantum Well with an Applied Electric Field," *Physica A & B*, Vol. 138, No. 3, 1986, pp. 287-294. doi:10.1016/0378-4363(86)90009-4

[16] N. G. Semaltianos, "Photoluminescence Studies of GaAs/AlGaAs Multiple Quantum Well Heterostructures," *Journal of Physics and Chemistry of Solids*, Vol. 63, No. 2, 2002, pp. 273-277. doi:10.1016/S0022-3697(01)00140-8

[17] V. Albe and L. J. Lewis, "Optical properties of InAs/InP Ultrathin Quantum Wells," *Physica B*: *Condensed Matter*, Vol. 301, No. 3-4, 2001, pp. 233-238. doi:10.1016/S0921-4526(01)00269-1

[18] D. Ahn, "Intersubband Transitions in Doped Semiconductor with an Applied Electric Field: Exact Solutions," *Physical Review B*, Vol. 48, No. 11, 1993, pp. 7981-7985. doi:10.1103/PhysRevB.48.7981

[19] V. A. Kul'Bachinskii, *et al.*, "Transport and Optical Properties of Tin δ-Doped GaAs Structures," *Semiconductors*, Vol. 33, No. 7, 1999, pp. 771-778.

[20] K. T. Kim, *et al.*, "Inter-Miniband Optical Absorption in a Modulation-Doped $Al_xGa_{(1-x)}As$/GaAs Superlattice," *Journal of Applied Physics*, Vol. 69, No. 9, 1991, pp. 6617-6624. doi:10.1063/1.348875

[21] J. A. Cuesta, A. Sanchez and F. Dominguez-Adame, "Self-Consistent Analysis of Electric Field Effects on Si Delta-Doped GaAs," *Semiconductor Science and Technology*, Vol. 10, No. 10, 1995, p. 1303. doi:10.1088/0268-1242/10/10/002

[22] E. Ozturk and I. Sokmen, "The Electric Field Effects on Intersubband Optical Absorption of Si δ-Doped Gaas Layer," *Solid State Communications*, Vol. 126, No. 11, 2003, pp. 605-609. doi:10.1016/S0038-1098(03)00301-6

[23] J. Osvald, "Electronic Properties of a near Surface Si δ-Doped GaAs under an Applied Electric Field," *Journal of Physics D*: *Applied Physics*, Vol. 37, No. 19, 2004, p. 2655. doi:10.1088/0022-3727/37/19/007

Copyright © 2012 SciRes.

Optics and Photonics Journal, **2012, 2, 145-151**
doi:10.4236/opj.2012.23021 Published Online September 2012 (http://www.SciRP.org/journal/opj)

Local Field Effects in the Luminescence of the Cone-Like Nanohills

V. Lozovski[1], A. Medvid[1,2], V. Piatnytsia[1]
[1]Institute of High Technologies, National Taras Shevchenko University of Kyiv, Kyiv, Ukraine
[2]Riga Technical University, Riga, Latvia
Email: pyatnyx@gmail.com

Received May 30, 2012; revised June 29, 2012; accepted July 14, 2012

ABSTRACT

The main purpose of the work is to clarify the physical mechanisms which leads to the specific spectrums of the structures [1-3]. The work is based on the ideas of the effective susceptibility. The effective susceptibility of cone-shaped nanohills located at the semiconductor surface is obtained in the frame of local-field approach. The knowledge of the effective susceptibility allows to calculate the optical absorption profiles. Using the approach similar to Levshin rule the photoluminescence spectra were calculated. Obtained results were compared with experimental luminescence spectra obtained earlier. The significant machanisms, that define the peculiarities of the spectra, is the shape of the nanoclasters and the inhomogeneity of the nanohills array are justificated. The main issue of the work is that the cause of the luminescence spectrums has electodynamical nature without spatial quantisation effects.

Keywords: Mesoparticle; Cone Shape; Effective Susceptibility; Imperfect Array; Luminescence

1. Introduction

Nowadays the experiments of luminescence of the nanohills fabricated by laser beam scanning along the silicon surface were reported [1-3]. The effect of luminescence by the nanohills in the works [1-3] was explained by existing varyband structure of the nano-rods. The spatial quantization is the cause of luminescence effect in the nanohills. This explanation seems to us rather not well-grounded and, of course, it is only for qualitative. Indeed the electron state of the quantum dot is formed in the particle as a whole. It means one should obtain the electron eigenstates inside the cone-like quantum dot and, then, calculate the transition currents, effective susceptibilities and luminescence spectra. The developing of correct microscopic model for explanation of discussed results becomes very hard problem. However, one can get round the difficulties using the mesoscopic approach using the local-field method. In the frame of so-called effective susceptibility concept [4] it is possible to calculate the luminescence spectra by the methods of the mesoscopic electrodynamics. In the frame of this approach the local-field effects can give the forthcoming result. As it is well-known, the local-field effects strongly depend on the particle shape and size [4,5]. Moreover, the effective susceptibility of the nanoparticle arrays depends on the particle shapes and size distribution. Then, taking into account the cone-like shape of the particles at the surface and its shape distribution one can calculate the absorption spectra and, then, using the widely applicable Levshin rule [6,7]—calculate the luminescence spectra. This problem was solved in this work.

2. Model and Problem Set up

The scanning by the laser beam of the semiconductor surface can lead to fabrication of the systems of the nanohills shaped as a cone, which was reported in [1-3]. It is well known, that the mechanical stresses appear when the nano-objects are fabricated at the surface [8-11]. The stress fields lead to distortion of the electron and optical properties of the nano-systems [12,13].

Specifically, these distortions become apparent in shifts of the absorption edge and transform the indirect band energy structure to the direct one [12,13]. This fact leads, in part, to ability of the luminescence observation in Si nano-particles [12]. This effect is similar to the nanoporous silicon [12]. Moreover, the complicated structure of the absorption and luminescence spectra can't be explained by the mechanical stresses [12]. Here we attempt to describe the peculiarities of the absorption and luminescence spectra of the nanohills systems in the frame of local-field approach. There are many works where the similar effects were explained with the local field interactions in the nano-particles [5,14]. It is well known, that the local-field effects are strongly defined by the shapes

Copyright © 2012 SciRes.

and dimensions of the particles [5,14,15]. Moreover the distribution of the nano-particles arrays over the shapes and the dimensions defines the optical properties of the nano-particles arrays. Just these two aspects of the system are taken into account in the present work. To describe the luminescent properties of cone-shaped nano-hills one use the so-called effective susceptibility concept [5,14]. To calculate the effective susceptibility of the nano-particles array one should to start from the dielectric function of the material from which the particle is fabricated. The dielectric function of silicon modified by the stress effects is used [13,16] in the frame of the discussed approach. One should note that one of the features of the meso-particles array is the distribution of the particles as over its shape as over its dimension. It is clear that the optical properties of the system are defined by these distributions. The distribution functions of Lifshits-Slezov-Wagner [17] and Gauss are used in the present work.

The paper is organized as follows. In Section 3 we give a brief description of the local field method and obtain the single meso-particle effective susceptibility. In Section 4 we obtain the formula of the effective susceptibility of the inhomogeneous two-dimensional array of the particles in the frame of Green function formalism. And in Section 5 the results of our calculations by semi analytical method are presented and compared with the experimental data.

3. Effective Susceptibility of Small Particle

For solving the problem of the calculation of the linear response to the external field (so-called, effective susceptibility) of the single meso-particle at the surface of a solid (**Figure 1**), one use the local-field method [5,14,15]. Let one consider the interaction of the small particle with the external electromagnetic field. The self-consistent electric field at any point inside the system obeys the equation [5,14,15,18],

$$E_i(\mathbf{R},\omega) = E_i^0(\mathbf{R},\omega) - i\omega\mu_0 \int_V G_{ij}(\mathbf{R},\mathbf{R}',\omega)\, j_j(\mathbf{R}',\omega)\,\mathrm{d}\mathbf{R}' \tag{1}$$

where $E_i^0(\mathbf{R},\omega)$ is an electric component of external field, $G_{ij}(\mathbf{R},\mathbf{R}',\omega)$ is the photon propagator, describes the electromagnetic field propagating in the medium in which the particle is embedded. This medium is the substrate with flat surface in the case under consideration.

Because of connection between the local current $j_j(\mathbf{R},\omega)$ and the local field $E_i(\mathbf{R},\omega)$ which usually named as constitutive equation,

$$\begin{aligned} j_j(\mathbf{R},\omega) &= -i\omega\chi'_{jk}(\omega)E_k(\mathbf{R},\omega), \\ \chi'_{jk}(\omega) &= \varepsilon_0\chi_{jk}(\omega) \end{aligned} \tag{2}$$

where $\chi_{jk}(\omega)$ is susceptibility of the bulk material from

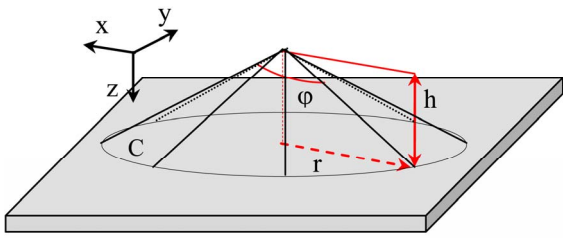

Figure 1. Setup of calculations.

which the particle is fabricated, Equation (1) transforms to self-consistent equation for local-field which usually named as Lippmann-Schwinger equation [5,14,15],

$$E_i(\mathbf{R},\omega) = E_i^0(\mathbf{R},\omega) - \frac{\omega^2}{c^2}\int_V G_{ij}(\mathbf{R},\mathbf{R}',\omega)\,\chi_{jk}(\omega)\,E_k(\mathbf{R}',\omega)\,\mathrm{d}\mathbf{R}'. \tag{3}$$

The introduction of the effective susceptibility which connects the local current $j_j(\mathbf{R},\omega)$ with the external field $E_k^0(\mathbf{R},\omega)$,

$$j_j(\mathbf{R},\omega) = -i\omega\tilde{\mathrm{X}}_{jk}^{(S)}(\mathbf{R},\omega)\,E_k^0(\mathbf{R},\omega) \tag{4}$$

allows us to write the solution of Lippmann-Schwinger equation in the form,

$$E_i(\mathbf{R},\omega) = E_i^0(\mathbf{R},\omega) - \frac{\omega^2}{c^2}\int_V G_{ij}(\mathbf{R},\mathbf{R}',\omega)\,\mathrm{X}_{jk}^{(S)}(\mathbf{R}',\omega)\,E_k^{(0)}(\mathbf{R}',\omega)\,\mathrm{d}\mathbf{R}' \tag{5}$$

with the dimensionless effective susceptibility $\mathrm{X}_{jk}^{(S)}(\mathbf{R},\omega)$: $\tilde{\mathrm{X}}_{jk}^{(S)}(\mathbf{R},\omega) = \varepsilon_0\mathrm{X}_{jk}^{(S)}(\mathbf{R},\omega)$. The effective susceptibility of the single meso-particle at the surface of the solid can be calculated according to the equation obtained in [5]

$$\mathrm{X}_{ij}^{(S)}(\mathbf{R},\omega) = \chi_{ik}(\omega)\left[\delta_{jk} - k_0^2\int_V G_{jl}(\mathbf{R}',\mathbf{R},\omega)\,\chi_{lk}(\omega)\,\mathrm{d}\mathbf{R}'\right]^{-1}, \tag{6}$$

where photon propagator corresponds to a two semi-spaces with the ideal flat interface. This expression will be initial one for calculations provided in the present work. The detail analysis of the effective susceptibility in form Equation (6) was provided in [5]. In part, it was shown that obtained expression for the effective susceptibility Equation (6) is true under condition of nonzero of imagine part of the matrix,

$$\left[\delta_{ik} - k_0^2\int_V G_{ij}(\mathbf{R},\mathbf{R}',\omega)\,\chi_{jk}(\omega)\,\mathrm{d}\mathbf{R}'\right]$$

determinant, and equation

$$\mathrm{Re}\det\left[\delta_{ik} - k_0^2\int_V G_{ij}(\mathbf{R},\mathbf{R}',\omega)\,\chi_{jk}(\omega)\,\mathrm{d}\mathbf{R}'\right] = 0, \tag{7}$$

Copyright © 2012 SciRes.

defines the eigenmodes in the system. It is clear that because integral over the particle volume in Equation (6) the behavior of the effective susceptibility of the particle will be strongly depended on the particle shape and size. The behavior of the effective susceptibility $\chi_{jk}(\mathbf{R},\omega)$ can be studied numerically. For example, the imaginary part of χ_{xx} averaged over the volume of the particle for the single cone-like particle is depicted in the **Figure 2** (colour plot). In the **Figure 3** depicted the same dependence via the curve representation. It is could be seen that the dependence of χ_{xx} on the particle shape (more correctly, on the cone height h) is strong and at any value of h the behavior of $\chi_{xx}(\omega)$ drastically changes—line is split.

4. Absorption Spectra of Two-Dimensional Cone-Like Particle Arrays

It is clear that experimentally obtained meso-particle arrays are characterized by the particles with the different

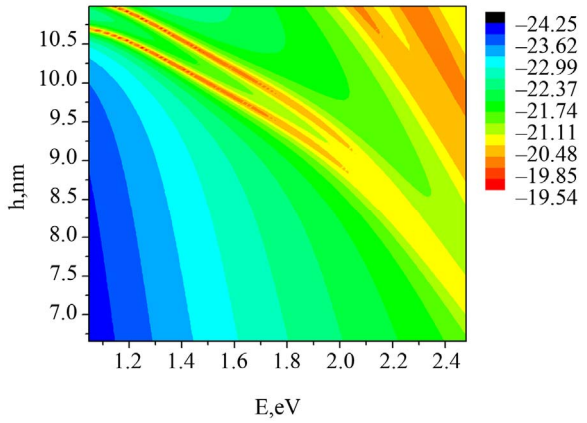

Figure 2. Effective susceptibility of single cone like Si mesoparticle (*xx*-part) as a function of photon energy and cone height (two dimensional dependence).

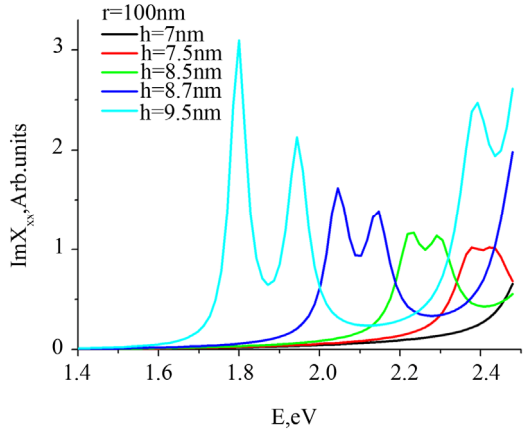

Figure 3. Effective susceptibility of single cone like Si mesoparticle (*xx*-part) as a function of photon energy at different values of the height of the cone under consideration.

shapes and dimensions. Then, using the result of previous section, one should calculate the effective susceptibility of the meso-particle array. To calculate the effective susceptibility of the meso-particles array one should consider the self-consistent equation,

$$E_i(\mathbf{R},\omega) = E_i^{(0)}(\mathbf{R},\omega) - a\sum_{\alpha=1}^{N}\int_{V_\alpha} d\mathbf{R}' G_{ij}(\mathbf{R},\mathbf{R}',\omega)\,\mathrm{X}_{jl}^{(S)}(\mathbf{R}',\omega)\,E_l(\mathbf{R}',\omega) \tag{8}$$

where the summation is over the different particles.

Let us suppose that the meso-particles form the rare array, which means that average distances between the particles are larger than linear dimensions of them. Taking into account the results of the works [14,19,20], one can consider the meso-particles as the point-like dipoles which polarises as the nonpointness object with the defined shape and dimension. Thus the second term in the right part of Equation (8) can be reduced to

$$\sum_{\alpha}\int_{V_q} d\mathbf{R}' G_{ij}(\mathbf{R},\mathbf{R}',\omega)\,\chi_{jl}(\omega)\,E_l(\mathbf{R}',\omega) \approx \sum_{\alpha} G_{ij}(\mathbf{r}-\mathbf{r}_\alpha,z,z_\alpha,\omega)\,\tilde{\chi}_{jl}(\omega)\,E_l(\mathbf{r}_\alpha,z,z_\alpha,\omega) \tag{9}$$

with

$$\tilde{\chi}_{jl}^{(\alpha)}(\omega) = (1/V_\alpha)\int_{V_\alpha} d\mathbf{R}\ \mathrm{X}_{jl}^{(S)}(\mathbf{R},\omega),$$

is the averaged polarizability of the single particle of α-th kind at the surface. In general, the mesoparticle arrays consist of the particles having different dimensions and differently shapes. It means that the sum in Equation (9) splits to the double sum, internal term of which is the sum of particles with the same parameters (named by the α-th subsystem),

$$\sum_{\alpha}(\cdots) = \sum_{\alpha}^{s}\sum_{q}^{N_\alpha}(\cdots) \tag{10}$$

where N_α is a number of particles in the α-th subsystem, and s is a number of the subsystems. It is naturally to suppose that the particles are distributed homogeneously along the surface of the substrate. Then, one should average Equation (9) over the particles positions. For this purpose one should, first, to perform Fourier transformation of Equation (8) taking into account Equation (9), due to lateral homogeneity. Let one average out Equation (9) by the particle positions, using Equation (10). Then, taking into account that occupied position can't be occupied by the other particle, one should use the uniform distribution [14,19]. Because the meso-particle array can be considered as quasi-uniform spatial system in the plane of the substrate (XOY plane), one can transmit to so-called *k-z* representation [4],

Copyright © 2012 SciRes.

$$\left\langle \sum_{q=1}^{N_\alpha} G_{ij}\left(\mathbf{r}-\mathbf{r}_q,z,z_q,\omega\right)\tilde{\chi}_{jl}^{\alpha}(\omega)E_l\left(\mathbf{r}_q,z,z_q,\omega\right)\right\rangle$$
$$=\frac{1}{S^{N_\alpha-1}}\int d\mathbf{r}_1 d\mathbf{r}_2\cdots d\mathbf{r}_{N_\alpha-1}\sum_{q=1}^{N_\alpha-1}\int\frac{d\mathbf{k}e^{-i\mathbf{k}\left(\mathbf{r}-\mathbf{r}_q\right)}}{\left(2\pi\right)^2}G_{ij}\left(\mathbf{k},z,z_q,\omega\right)$$
$$\times\tilde{\chi}_{jl}^{\alpha}(\omega)\int\frac{d\mathbf{k}'e^{-i\mathbf{k}'\mathbf{r}_q}}{\left(2\pi\right)^2}E_l\left(\mathbf{k}',z_q,\omega\right) \tag{11}$$

where **r** and **k** are the coordinate and wave vector in the XOY plane, respectively, S is the area of the substrate. To calculate this expression one should to consider $N_\alpha-1$ summand of the sum in right part of Equation (11), which has a form,

$$\overbrace{\int d\mathbf{r}_1\cdots d\mathbf{r}_{N_\alpha-2}}^{=S^{N_\alpha-2}}\int d\mathbf{k}'\int\frac{d\mathbf{k}e^{-i\mathbf{k}\mathbf{r}}}{\left(2\pi\right)^2}G_{ij}\left(\mathbf{k},z,z_q,\omega\right)\tilde{\chi}_{jl}^{q}(\omega)$$
$$\times E_l\left(\mathbf{k}',z_q,\omega\right)\overbrace{\int\frac{d\mathbf{r}_{N_\alpha-1}}{\left(2\pi\right)^2}e^{-i\mathbf{r}_{N_\alpha-1}(\mathbf{k}-\mathbf{k}')}}^{=\delta(\mathbf{k}-\mathbf{k}')} \tag{12}$$
$$=S^{N_\alpha-2}\int\frac{d\mathbf{k}e^{-i\mathbf{k}\mathbf{r}}}{\left(2\pi\right)^2}G_{ij}\left(\mathbf{k},z,z_q,\omega\right)\tilde{\chi}_{jl}^{\alpha}(\omega)E_l\left(\mathbf{k},z_q,\omega\right).$$

As a result, the right part of Equation (9) is written as

$$\left\langle \sum_{q=1}^{N_\alpha} G_{ij}\left(\mathbf{r}-\mathbf{r}_q,z,z_q,\omega\right)\tilde{\chi}_{jl}^{\alpha}E_l\left(\mathbf{r}_q,z,z_q,\omega\right)\right\rangle$$
$$=\frac{N_\alpha-1}{S}\int\frac{d\mathbf{k}e^{-i\mathbf{k}\mathbf{r}}}{\left(2\pi\right)^2}G_{ij}\left(\mathbf{k},z,z_q,\omega\right)\tilde{\chi}_{jl}^{\alpha}(\omega)E_l\left(\mathbf{k},z_q,\omega\right). \tag{13}$$

Then, the equation of the self-consistent field written for the system under consideration has form

$$E_i\left(\mathbf{k},z_q,\omega\right)$$
$$=E_i^{(0)}\left(\mathbf{k},z_q,\omega\right) \tag{14}$$
$$-\sum_{\alpha}^{s}aG_{ij}\left(\mathbf{k},z,z_q,\omega\right)n_\alpha\tilde{\chi}_{jl}^{\alpha}(\omega)E_l\left(\mathbf{k},z_q,\omega\right)$$

where

$$n_\alpha=\lim_{N_\alpha,S\to\infty}\left(N_\alpha-1\right)\Big/S$$

is concentration of the particles of α-th type. The dependence between the induced subsystem dipole moment and the external field,

$$E_l\left(\mathbf{k},z_q,\omega\right)$$
$$=\frac{1}{\varepsilon_0}\left(\tilde{\chi}_{jl}^{\beta}(\omega)\right)^{-1}P_j^{\beta}\left(\mathbf{k},z_q,\omega\right). \tag{15}$$

Substituting Equation (15) in Equation (14) one can obtain the polarization of the β-th subsystem

$$P_j^{\beta}\left(\mathbf{k},z_q,\omega\right)$$
$$=\varepsilon_0\left[\left(\tilde{\chi}_{jl}^{\beta}(\omega)\right)^{-1}+\sum_{\alpha}^{s}aG_{ij}\left(\mathbf{k},z,z_q,\omega\right)\right.$$
$$\left.\times n_\alpha\tilde{\chi}_{jl}^{\alpha}(\omega)\left(\tilde{\chi}_{jl}^{\beta}(\omega)\right)^{-1}\right]^{-1} \tag{16}$$
$$\times E_i^{(0)}\left(\mathbf{k},z_q,\omega\right)$$

Then, the polarizability (the effective susceptibility) of the total system has a form,

$$\mathrm{X}_{jl}\left(\mathbf{k},z_q,\omega\right)$$
$$=\sum_{\beta}^{s}n_\beta\tilde{\chi}_{ji}^{\beta}(\omega)\left[\delta_{li}+\sum_{\alpha}^{s}aG_{lk}\left(\mathbf{k},z,z_q,\omega\right)n_\alpha\tilde{\chi}_{ki}^{\alpha}(\omega)\right]^{-1}. \tag{17}$$

This equation will be used for further calculations of the absorption and luminescent spectra of the system under consideration. Present paper calculation based on the method developed in [18] with adaptation into present model of the one. According to the definition of the absorption spectra,

$$Q=\frac{1}{4}\left\langle\overline{\left(\vec{J}+\vec{J}^{*}\right)\left(\vec{E}+\vec{E}^{*}\right)}\right\rangle. \tag{18}$$

All characteristics that include Equation (18) are volume averaged already, and due to time averaging,

$$Q=\frac{1}{4}\left(J_i^{*}\left(\mathbf{R},\omega\right)E_i\left(\mathbf{R},\omega\right)+J_i\left(\mathbf{R},\omega\right)E_i^{*}\left(\mathbf{R},\omega\right)\right). \tag{19}$$

Let consider expressions,

$$J_j^{\alpha}\left(\mathbf{k},z_q,\omega\right)=-i\omega\tilde{\chi}_{jl}(\omega)F_{li}^{\alpha}\left(\mathbf{k},z_q,\omega\right)E_i^{(0)}\left(\mathbf{k},z_q,\omega\right) \tag{20}$$

$$E_j^{\alpha}\left(\mathbf{k},z_q,\omega\right)=F_{ji}^{\alpha}\left(\mathbf{k},z_q,\omega\right)E_i^{(0)}\left(\mathbf{k},z_q,\omega\right) \tag{21}$$

where

$$F_{ij}^{\alpha}\left(\mathbf{k},z_q,\omega\right)$$
$$=\left[\delta_{ij}+\sum_{\alpha}^{s}aG_{ij}\left(\mathbf{k},z,z_q,\omega\right)n_\alpha\tilde{\chi}_{jl}^{\alpha}(\omega)\right]^{-1}$$

is local field factor.

Formulas above are written in $\mathbf{k}-z$ representation, they must be convenient to use in Equation (19). Thus it is necessary to perform inverse Fourier transformation. Due to suppositions considered above they has simple view,

$$J_j^{\alpha}\left(\mathbf{k},z_q,\mathbf{r},\omega\right)$$
$$=-i\omega\tilde{\chi}_{jl}(\omega)F_{li}^{\alpha}\left(\mathbf{k},z_q,\omega\right)E_i^{(0)}\left(\mathbf{k},z_q,\omega\right)e^{ik_z z_q}e^{i\mathbf{k}\mathbf{r}} \tag{22}$$

$$E_j^{\alpha}\left(\mathbf{k},z_q,\mathbf{r},\omega\right)=F_{ji}^{q}\left(\mathbf{k},z_q,\omega\right)E_i^{(0)}\left(\mathbf{k},z_q,\omega\right)e^{ik_z z_q}e^{i\mathbf{k}\mathbf{r}}. \tag{23}$$

Substituting Equations (22) and (23) into Equation (19) one obtains the dissipative function of nanoparticle array

Copyright © 2012 SciRes.

in the form,

$$Q = \frac{\omega}{2}\sum_{\alpha=1}^{s} n_\alpha \operatorname{Im}\left\{\tilde{\chi}_{jl}^{\alpha}\right\} F_{li}^{\alpha} F_{ij}^{\alpha *} E_i^{(0)} E_i^{(0)*}. \qquad (24)$$

Include into consideration distribution function

$$\sum_{\alpha=1}^{s} n_\alpha = \sum_{\alpha=1}^{s} f_\alpha(\xi_\alpha)\Delta\xi_\alpha \xrightarrow{\Delta\xi_\alpha \to 0} \int_{\xi_1}^{\xi_2} \mathrm{d}\xi f(\xi),$$

where ξ is some parameter of the particle.

Final view of absorption spectra formula

$$Q = \frac{\omega}{2}\int_{\rho_1}^{\rho_2} \mathrm{d}\xi f(\xi) \operatorname{Im}\left\{\tilde{\chi}_{jl}^{\alpha}(\xi)\right\} F_{li}^{\alpha} F_{ij}^{\alpha *} E_i^{(0)} E_i^{(0)*}, \qquad (25)$$

where $\tilde{\chi}_{jl}^{\alpha}(\xi)$ is effective susceptibility of the single particle with the parameter ξ, which founded in previous section.

4. Numerical Calculations and Discussions

Numerical calculations were performed in the frames of the model of the bulk material susceptibility with corrections discussed above. The susceptibility of the bulk silicon and germanium were taken from [13,16]. As could be seen from the experimental data (green colored lines at **Figures 4** and **5**) the range of luminescence spectrum is about 1 eV near the absorption edge from 1.2 eV to 2.3 eV. That is why in the theoretical calculations only absorption edge were taken into consideration with the frequency shift about 0.2 eV and grows of the intensity about 2 units. In the model we use the different distribution functions which fulfill different models of growing of the structures to find the most suitable. The averaged dimension of the particles were chosen as the next: Radius of the base of the cone was equal to $r = 100$ nm, the averaged height of the cone-like particles was equal to $h_{\mathrm{mid}} = 8$ nm. It was supposed that heights of the cone-like particles are varies from $h_{\min} = 7.5$ nm to $h_{\max} = 9.5$ nm. There different shape distributions of the particles were used in the present work. Gauss distribution function has form

$$f(h) = C_G \exp\left(\frac{(h - h_{\mathrm{mid}})^2}{2\sigma^2}\right) \qquad (26)$$

with the constant C_G being founded from the relation $N = \int_{h_{\min}}^{h_{\max}} f(h)\mathrm{d}h$, where is the total number of the particles in the array. Lifshits-Slezov-Wagner distribution function can be represented in the form [17],

$$f(h) = C_{LS} u^2 (1-u)^{-B} \left(u + x^2 + x\right)^D \exp\left(\frac{C}{1-u}\right) \qquad (27)$$

$$B = \frac{2x^4 + 4x^3 + 12x^2 + 10x + 5}{x^4 + 2x^3 + 3x^2 + 2x + 1} \qquad (28)$$

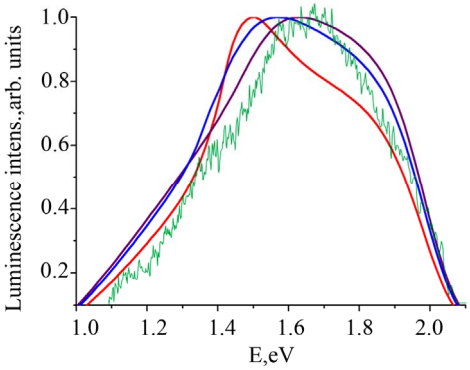

Figure 4. Luminescence spectra of different structures [1-3]: Green colored line is experimental data, red colored Lifshits-Slezov distribution (x = 1), purple is Wagner distribution (x = 0), blue is Gauss distribution, SiO_2/Si structure, T_{ne} = 60.

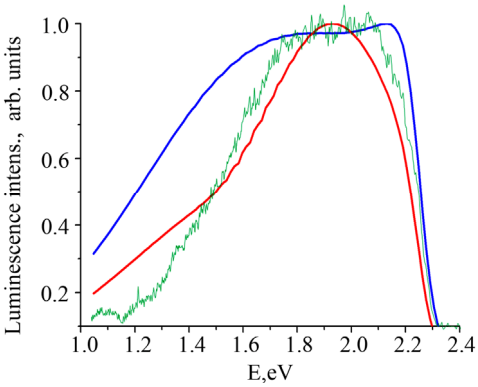

Figure 5. Luminescence spectra of different structures [1-3]: Green colored line is experimental data, red colored Lifshits-Slezov distribution (x = 1), purple is Wagner distribution (x = 0), blue is Gauss distribution, $Si_{0.7}Ge_{0.3}$/Ge, T_{ne} = 55.

$$C = -\frac{3x^2 + 3x + 3}{x^4 + 2x^3 + 3x^2 + 2x + 1} \qquad (29)$$

$$D = -\frac{4x^4 + 8x^3 + 6x^2 + 2x + 1}{x^4 + 2x^3 + 3x^2 + 2x + 1} \qquad (30)$$

where $u = \frac{h}{h_{\max}}$, $h_{\max}$ is the maximal dimension of the particle in the array, x is the parameter of the model depends on the kinetic properties of the different materials ($0 \le x \le 1$) [11]. Constant C_{LS} is founded from the normalisation equation.

The luminescence spectra for structures 1) SiO_2 (substrate)/Si(particle) and 2) $Si_{0.7}Ge_{0.3}$/Ge are depicted in **Figures 4** and **5**, green colored lines are experimental data. For estimation the luminescence spectra via absorption profile we use so-called Levshin rule [6,7,21],

$$L(\omega) = \omega^3 \exp\left(-\frac{\hbar\omega - E_0}{kT_{ne}}\right) Q(\omega) \qquad (31)$$

Copyright © 2012 SciRes.

where T_{ne} is the fenomenological constant. From the form of the structures obtained by the laser beam scanning along the silicon surface [1-3] one can see that interparticle distances are comparable with wave length. As we can see from the experimental spectra wave length at the left side of the spectra two times larger than at the right side. Moreover intensity of the diffuse scattering for the small wave length is larger. That is why the effective intensity of radiation at the detector must be smaller. For the estimation of the theoretical curve one uses the phenomenological function which describes intensity at the detector. The function must satisfy the next conditions: 1) The scattering processes are not appreciable for the long wave length photons. It means the function must be constant in the long wavelength limit; 2) When the wavelength is comparable with inhomogeneties of the structure the function must abate,

$$f\left(E_0,\Delta\right)=\frac{1}{1+\exp\left(\dfrac{E-E_0}{\Delta}\right)} \tag{32}$$

where E_0 is the phenomenological energy which corresponds to the critical wavelength, and which corresponds to range of the frequencies of the effective scattering.

It could be easily seen (**Figure 4**)) that model with Lifshits-Slezov (Lifshits-Slezov-Wagner, x = 1) (red colored line) the distribution function more suitable than symmetric Gauss distribution (blue colored line). And at the **Figure 5** we can see the same situation where Wagner distribution function (Lifshits-Slezov-Wagner, x = 0) more suitable than symmetrical Gausian. It is expected result because of the heat action of the laser beam because Lifshits-Slezov distribution was derived for the annealing process [11]. In contrast the etching process [8] where presented logarithmic normal size distribution with the dominant number of the smaller particles. We can see from **Figure 4** that the local field effects lead to rather strong distortion of the initial curve [13] describing absorption properties of the bulk material from which the nanohills are made. As we can see from **Figures 4** and **5**, the maximum of the calculated luminescence curve has the same position as at the experimental data curve and it has the similar low frequency side. In **Figure 5** for another pair of materials ($Si_{0.7}Ge_{0.3}$/Ge) we can see the same features at the low frequency range and it is comparable with experimental data. It is easy to see that both SiO_2/Si and $Si_{0.7}Ge_{0.3}$/Ge have similar peculiarities in the same region of the photon energies. It allows us to think that the nature of the features observed above are similar.

5. Conclusion

The model of two dimensional array of cone-shaped meso-particles for explanation of the experimental data reported earlier by the authors in [1-3] is proposed. As opposed to [1-3] where obtained the results were explained by the spatial quantization effects here one proposed the additional approach based on taking into account the local-field interactions inside the particles and the interparticle interactions. The local-field interactions inside the particles were considered in the frame of effective susceptibility concept in the near-field approximation. The interparticle electro dynamical interactions were considered rather strongly by solution of Lippmann-Schwinger equation for the system under consideration with what taken into account as near- as middle- and far-field interactions. Different models of the particle distributions—Gaussian-like distribution and Lifshits-Slezov-Wagner distribution were used. The both models of the particle distribution give qualitatively correct results. But the Lifshits-Slezov-Wagner distribution model is the most suitable. This fact allows us to conclude that particle distri- bution obtained by laser heating [1-3] of SiO_2 surface is described by Lifshits-Slezov-Wagner distribution with x = 1. In the case of $Si_{0.7}Ge_{0.3}$ surface the luminescence spectrum is described by Wagner distribution. Comparison of calculated and experimentally obtained luminescence spectra allows us to think that the luminescence of the nanohills can be explained by the local-field effects.

REFERENCES

[1] A. Medvid, A. Mychko, A. Pludons and Yu. Naseka, "Laser Induced Nanostructure Formation on a Surface of CdZnTe Crystal," *Journal of Nano Research*, Vol. 11, 2010, pp. 107-112.

[2] A. Medvid, I. Dmitruk, P. Onufrijevs, D. Grabovskis, A. Mychko and I. Pundyk, "Control of Surface Roughness of Si and Ge Single Crystal by Laser Radiation," *JLMN*, Vol. 1, No. 3, 2006, pp. 172-175. doi:10.2961/jlmn.2006.03.0004

[3] A. Medvid, I. Dmytruk, P. Onufrijevs and I. Pundyk, "Quantum Confinement Effect in Nanohills Formed on a Surface of Ge by Laser Radiation," *Physica Status Solidi* (*C*), Vol. 4, No. 8, 2007, pp. 3066-3069. doi:10.1002/pssc.200675477

[4] V. Lozovski, "The Effective Susceptibility Concept in the Electrodynamics of Nano-Systems," *Journal of Computational and Theoretical Nanoscience*, Vol. 7, No. 10, 2010, pp. 1-17. doi:10.1166/jctn.2010.1588

[5] V. Lozovski, "Susceptibilities of Nano-Particles at the Surface of a Solid," *Physica E*: *Low-Dimensional Systems and Nanostructures*, Vol. 9, No. 4, 2001, pp. 642-651. doi:10.1016/S1386-9477(00)00291-5

[6] W. L. Levshin, "Das Gesetz Der Spiegelkorrespondenz Der Absorption-Und Fluoreszenzspektren," *Zeitschrift Für Physik A Hadrons and Nuclei*, Vol. 72, No. 5-6, 1931, pp. 368-381. doi:10.1007/BF01341957

[7] V. L. Levshin, "Svechenie Aktivirovanukh Kristalov," *UFN*, Vol. 43, No. 3, 1951, pp. 426-484.

Copyright © 2012 SciRes.

[8] L. B. Freund and H. T. Johnson, "Influence of Strain on Functional Characteristics of Nanoelectronic Devices," *Journal of the Mechanics and Physics of Solids*, Vol. 49, No. 9, 2001, pp. 1925-1935. doi:10.1016/S0022-5096(01)00039-4

[9] L. B. Freund and H. T. Johnson, "The Influence of Strain on Confined Electronic States in Semiconductor Quantum Structures," *International Journal of Solids and Structures*, Vol. 38, No. 6-7, 2001, pp. 1045-1062.

[10] E. P. O'Reilly, "Valence Band Engineering in Strained-Layer Structures," *Semiconductor Science and Technology*, Vol. 4, No. 3, 1989, p. 121. doi:10.1088/0268-1242/4/3/001

[11] E. P. O'Reilly and A. R. Adams, "Band-Structure Engineering in Strained Semiconductor Lasers," *IEEE Journal of Quantum Electronics*, Vol. 30, No. 2, 1994, pp. 366-379. doi:10.1109/3.283784

[12] L. T. Canham, "Properties of Porous Silicon," INSPEC, London, 1997.

[13] E. Ghahramani, D. J. Moss and J. E. Sipe, "Linearoptical Properties of Strained (Si)n/(Ge)n Superlattices on (001) Si Substrates," *Physical Review B*, Vol. 41, No. 8, 1990, pp. 5112-5125. doi:10.1103/PhysRevB.41.5112

[14] O. Keller, "Local Fields in the Electrodynamics of Mesoscopic Media," *Physics Reports*, Vol. 268, No. 2-3, 1996, pp. 85-262. doi:10.1016/0370-1573(95)00059-3

[15] O. Keller and T. Garm, "Intraparticle and Interparticle Radiative Coupling in Quantum Dot Arrays: Influence of a Magnetic Field," *Journal of the Optical Society of America B*, Vol. 13, No. 10, 1996, pp. 2121-2128. doi:10.1364/JOSAB.13.002121

[16] R. Poerschke, "Semiconductors Group IV Elements and III-V Compounds," Springer-Verlag, Berlin, 1991.

[17] R. D. Vengrenovich, B. V. Ivanskii and A. V. Moskalyuk, "Generalized Lifshits—Slezov—Wagner Distribution," *Journal of Experimental and Theoretical Physics*, Vol. 104, No. 6, 2007, pp. 906-912. doi:10.1134/S1063776107060088

[18] V. Lozovski and A. Tsykhonya, "Dispersion Properties of Nano-Scale Systems," *International Journal of Theoretical Physics*, Vol. 12, No. 3, 2007, pp. 31-51.

[19] V. Chegel, Yu. Chegel, M. D. Guiver, A. Lopatynskyi, O. Lopatynska and V. Lozovski, "3D-Quantification of Biomolecular Covers Using Surface Plasmon-Polariton Resonance Experiment," *Sensors and Actuators B*, Vol. 134, No. 1, 2008, pp. 66-71. doi:10.1016/j.snb.2008.04.012

[20] I. Iezhokin, O. Keller and V. Lozovski, "Influence of Local Field on Spontaneous Light Emission by Nanoparticles," *Ukrainian Journal of Physics*, Vol. 54, No. 4, 2009, pp. 398-406.

[21] T. G. Meister, "Electronnye Spectry Mnogoatomnykh Molekul," LGU, Leningrad, 1969.

Copyright © 2012 SciRes.

Optics and Photonics Journal, **2012, 2, 152-156**
doi:10.4236/opj.2012.23022 Published Online September 2012 (http://www.SciRP.org/journal/opj)

Study on the Effect of Monochromatic Light on the Growth of the Red Tide Diatom *Skeletonema costatum*

Hongli Miao, Lina Sun, Qingzhen Tian, Shanshan Wang, Jing Wang
College of Information Science and Engineering, Ocean University of China, Qingdao, China
Email: wjing@ouc.edu.cn

Received June 19, 2012; revised July 21, 2012; accepted August 1, 2012

ABSTRACT

Effects of light intensity and quality of three kinds of LED monochromatic lights (blue, green, and red) on the growth of *Skeletonema costatum* are investigated in batch culture conditions. Seven light intensities (20, 30, 40, 45, 50, 60 and 80 $\mu mol \cdot m^{-2} \cdot s^{-1}$) are used to evaluate the specific growth rate, spectrum absorption coefficient and saturated light intensity of LED monochromatic light. Results show that the growth rates of *Skeletonema costatum* increase with the enhanced light intensity; however, the light level beyond the saturation light intensity inhibited the growth of *Skeletonema costatum*. Compared with red and green light, the growth rate of *Skeletonema costatum* under blue light is higher within saturated light intensity, and saturated light intensity of LED monochromatic light is lower under blue light and higher under green light. It is concluded that under different monochromatic light, the saturated light intensity decreases and the growth rate increases with the increasing of spectrum absorption coefficient.

Keywords: Monochromatic Light; Saturated Light Intensity; *Skeletonema costatum*; Growth Rate; Red Tide

1. Introduction

Under certain ecological conditions, some marine microalgae may grow rapidly in a short time and lead to discoloration of waterbody or water blooms, which refer to harmful algal blooms. Such over-proliferated blooms are harmful to other organisms and other organisms can be affected directly or indirectly [1]. The marine diatom *Skeletonema costatum* has been considered as one of the dominant red tide species in the coastal areas, and it distributes widely in the waters around the world. In China, it is one of typical seriously harmful red tide species [2]. Many physical factors play important roles in the growth of this harmful alga. Among these factors, light is an important environmental factor which can affect microalgae growth, and it is one of the key environmental factors of the red tides happened [3-6]. For a certain pH value, temperature, and nutrition conditions, the light intensity and the duration of illumination which decides the algae photosynthesis efficiency also play crucial roles on the growth rate of algae [7-9].

Many studies on the effects of light intensity, temperature and salinity have been reported [10-14]. However, in terms of light intensity, most studies focused on the effects of fluorescent or the sun-light on the growth of red tide species [10,11]. Studies of the influence of light on the *Skeletonema costatum* have been reported by Baiye Sun with filed culture experiments and model calculations [12], and the optimal light intensity for growth of *Skeletonema costatum* increases gradually to a maximum of 121.6 $W \cdot m^{-2}$ with temperature up to 25˚C. Under this temperature, the optimal irradiance was 7000 lx for *Skeletonema costatum* reported by Yu Ping [13]. Also, it was described that under the high temperature, *Skeletonema costatum* adapted to higher light intensity, and under the low temperature conditions it adapted to the low light intensity. The optimal light intensity for growth of *Skeletonema costatum* was 3000 - 6000 lx reported by Chou Jianbiao [14]. The light source in their studies was white light of fluorescent. However, white light is composed of seven monochromatic lights, in order to determine the role of light wavelength on the growth of *Skeletonema costatum* and explain the effects of light on the red tides from photosynthesis mechanism, it is necessary to research the effect of the monochromatic light on the growth conditions of *Skeletonema costatum*. Besides, in the experiment by using the filter to get the beam width of light for monochromatic research, light energy loss is serious, and the beam width of light is relatively large [15-17].

In this work, we use the monochromatic light-emitting diode (LED) as the light source and study the effects of three monochromatic lights on the growth of *Skeletonema costatum* with the same photosynthetic available quantum flux density. Based on the study on the effects of different wavelength of monochromatic light and different light intensities on the growth of *Skeletonema costatum*,

Copyright © 2012 SciRes.

we obtain the saturated light intensities of different monochromatic lights, and further provide the basis of analysis of the mechanism of the red tides occurrence.

2. Materials and Methods

2.1. Algal Species and Culture Conditions

The strain of *Skeletonema costatum* is obtained from the Institute of Fisheries College, Ocean University of China. Seawater used in this work is sterilized artificial seawater that is filtered through a 0.45 μm filter before used for culture medium preparation. Algal cells in the exponenttial growth phase are used, which are inoculated into 300 mL Erlenmeyer flasks containing 100 mL fresh f/2 enriched seawater. Stock cultures are maintained in sterilized Erlenmeyer flasks and cultivated in a plant growth chamber under the common background conditions of 21˚C with a 12:12 light:dark photoperiod. The lights used for the culture are provided by monochromatic LED with the center wavelength of 456 nm, 512 nm and 656 nm, respectively. The light intensity can be adjusted from 20 $\mu mol \cdot m^{-2} \cdot s^{-1}$ to 80 $\mu mol \cdot m^{-2} \cdot s^{-1}$ by changing the distance between the light source and vessel. The spectra of light sources are measured by PR-650 spectrophotometer/spectrocolorimeter, as shown in **Figure 1**.

2.2. Method of Measurement

For researching the growth condition of Skeletonema costatum, a 50 μL algal sample is fetched from each flask everyday, and then supported by a glass slide. The numbers of algal cell are counted under optical microscope, and cell number countings are repeated for at least three times. The specific growth rate μ was calculated during the exponential growth period by [18,19]

$$\mu = \frac{\ln N_2 - \ln N_1}{t_2 - t_1} \quad (1)$$

where N_1 and N_2 are cell numbers on days t_1 and t_2, respectively.

3. Results and Discussion

3.1. Effects of Light Intensity and Light Quality on the Growth of *Skeletonema costatum*

Firstly, we study the effect of blue light on the growth rate of *Skeletonema costatum*. *Skeletonema costatum* strain culture is maintained in conditions as mentioned above until the end of the exponential phase. The typical light intensity used are 20, 30, 40, 45, 50, 60 and 80 $\mu mol \cdot m^{-2} \cdot s^{-1}$. For all light intensities, the *Skeletonema costatum* has an exponential growth phase in seven days, as is shown in **Figure 2(a)**. (Considering that the cell cycle of *Skeletonema costatum* is about five days [12], we pay our attentions to the data in the first seven days). For different light intensities, the

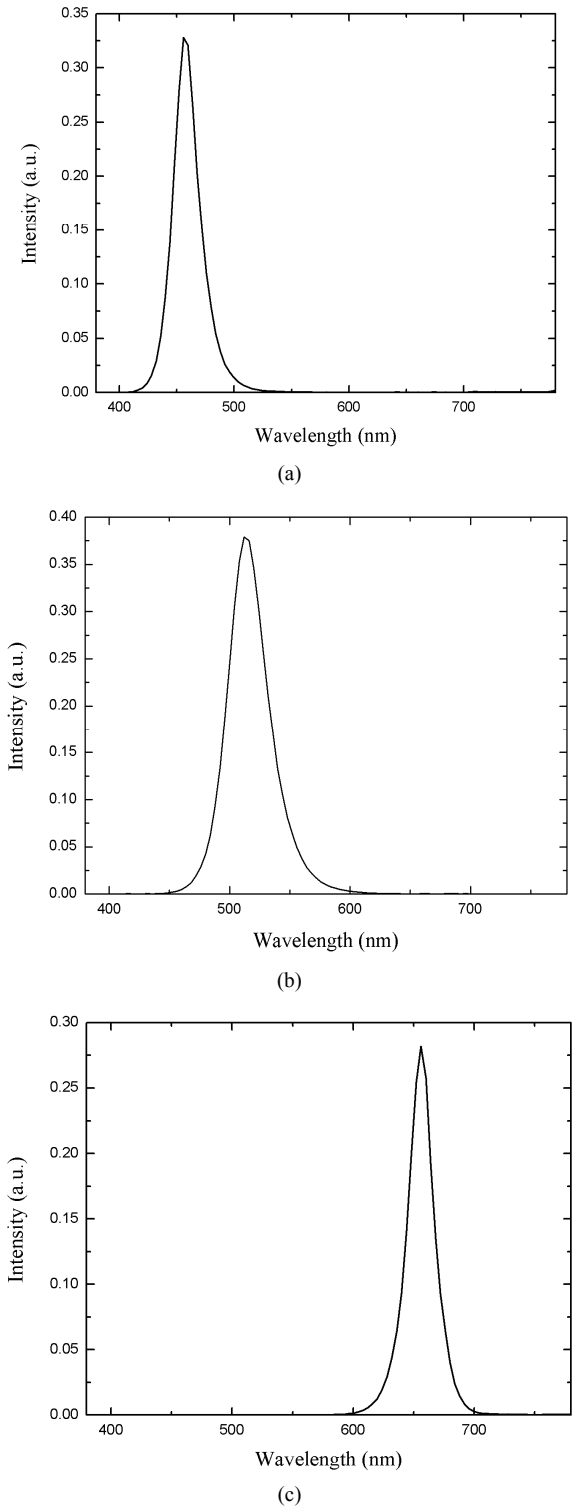

Figure 1. Spectra of three kinds of LED illuminants. (a) Blue; (b) Green; (c) Red.

growth of *Skeletonema costatum* is significantly different, especially after two days. Based on the cell number, we can calculate the growth rates under different light intensities using Equation (1). As is shown in **Figure 2(b)**, the

Copyright © 2012 SciRes.

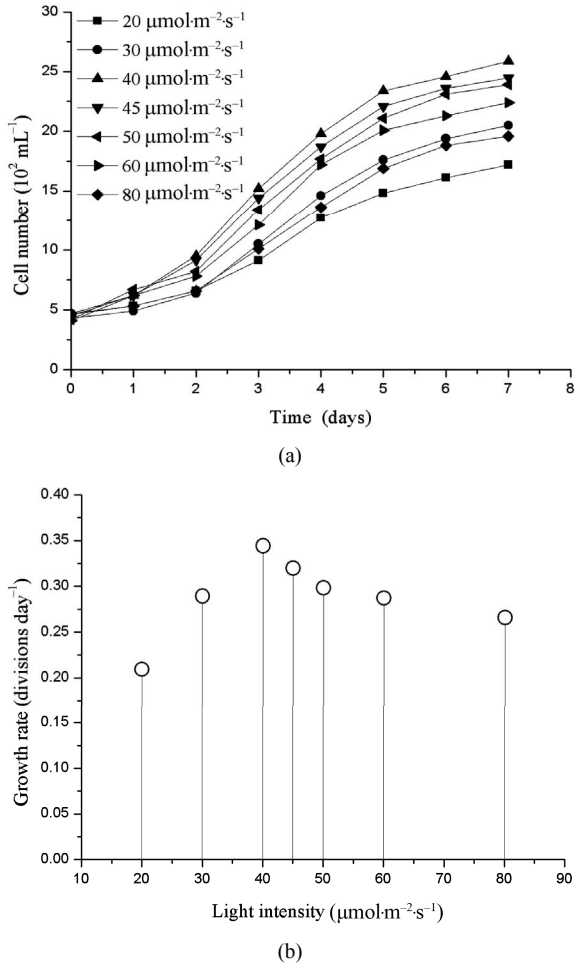

Figure 2. (a) The growth curve of *Skeletonema costatum* under blue light; (b) Growth rate of *Skeletonema costatum* under blue light.

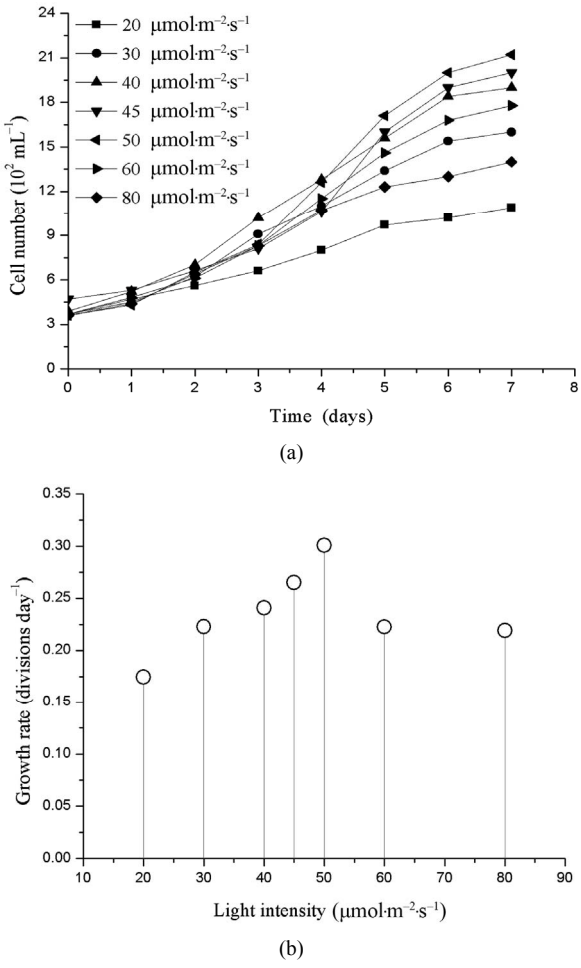

Figure 3. (a) The growth curve of *Skeletonema costatum* under green light; (b) Growth rate of *Skeletonema costatum* under green light.

growth rates increase with the increasing light intensity from 20 to 40 μmol·m^{-2}·s^{-1}, the maximum growth rate is observed at 40 μmol·m^{-2}·s^{-1} (**Figure 2(b)**). When the light level exceeds 40 μmol·m^{-2}·s^{-1}, the growth rates of *Skeletonema costatum* gradually decrease, which means the saturated light intensity of *Skeletonema costatum* under blue light is about 40 μmol·m^{-2}·s^{-1}.

When the *Skeletonema costatum* are cultured under green light, the effect of the wavelength on the growth of the microalgae is not significant in the first two days (**Figure 3(a)**), and then it goes significantly different after two days. Growth response curves as a function of intensity for *Skeletonema costatum* are shown in **Figure 3(b)**. The growth rates of *Skeletonema costatum* increase when light intensity increases from 20 to 50 μmol·m^{-2}·s^{-1}, and then decreases beyond 50 μmol·m^{-2}·s^{-1}. The highest growth rate of *Skeletonema costatum* is 0.3006 at 50 μmol·m^{-2}·s^{-1}.

By the same method, we study the cell numbers and growth rates of *Skeletonema costatum* under red light, as is shown in **Figures 4(a)** and **(b)**. The growth rates of *Skeletonema costatum* increase with the increasing light intensity from 20 to 45 μmol·m^{-2}·s^{-1}. When exceeds this light intensity range, the growth rates gradually decrease. The maximum and minimum growth rates of Skeletonema costatum are 0.1953 at 20 μmol·m^{-2}·s^{-1} and 0.3212 at 45 μmol·m^{-2}·s^{-1}, respectively. The saturated light intensity of *Skeletonema costatum* under red light is about 45 μmol·m^{-2}·s^{-1}.

Results above show that when cells are exposed to blue, green or red light, the growth conditions of *Skeletonema costatum* are greatly influence by different light wavelength. For three kinds of monochromatic light, the growth rates of *Skeletonema costatum* are significantly different. The growth rate under blue light is larger than under green and red light until it reaches saturation light intensity. In blue light condition, the saturation light intensity is about 40 μmol·m^{-2}·s^{-1}, which below the value of saturation light intensity of the green (50 μmol·m^{-2}·s^{-1}) and red light (45 μmol·m^{-2}·s^{-1}).

Copyright © 2012 SciRes.

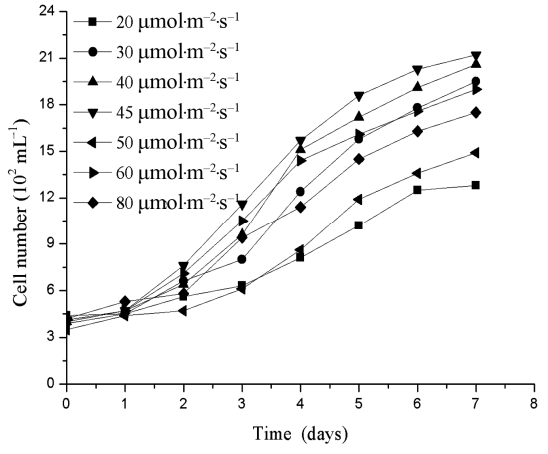

(a)

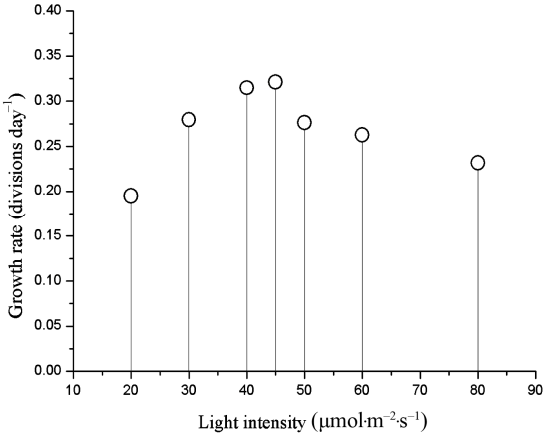

(b)

Figure 4. (a) The growth curve of *Skeletonema costatum* under red light; (b) Growth rate of *Skeletonema costatum* under red light.

3.2. The Relationship of Spectrum Absorption Coefficient and Growth Rate, Saturated Light Intensity

Spectrum absorption coefficient represents the quantum efficiency of the light photosynthetic effective quantum flux absorbed by microalgae, and it further reflects the efficiency of the light to promote the growth of microalgae. In this work, we estimated the relationship between the growth rates and spectrum absorption coefficient using the equation by [20]:

$$A_\eta = \frac{\sum_{400}^{700} \lambda\phi(\lambda)\left[1-10^{-OD(\lambda)}\right]\Delta\lambda}{\sum_{380}^{780} \lambda\phi(\lambda)\Delta\lambda} \quad (2)$$

where λ is wavelength, $\Delta\lambda$ is wavelength interval, $\phi(\lambda)$ is relative spectrum power density, and it is provided by the spectra of light sources. OD (λ) is absorbance, and it can be obtained from the absorption spectrum of microalgae, as is presented in **Figure 5**.

Based on Equation (2), it is now possible to estimate the spectrum absorption coefficient of *Skeletonema costatum* in different lights. Spectrum absorption coefficient of blue light is 0.0913 (**Figure 6**), it is larger than that of red light and green light (0.0871 and 0.0868, respectively). With the certain photosynthetic available quantum flux density, the growth rates of *Skeletonema costatum* is the highest under blue light and the lowest under green light within saturated light intensity. As a result, we can conclude that the saturated light intensity decreases and the rowth rate increases with the increasing of spectrum absorption coefficient.

4. Conclusion

In conclusion, effects of light intensity and quality of three kinds of LED monochromatic light (blue, green, and red) on the growth of *Skeletonema costatum* are investigated. Results indicate that *Skeletonema costatum* prefer blue and red light to green light and the saturated light intensity is significantly different under three monochromatic

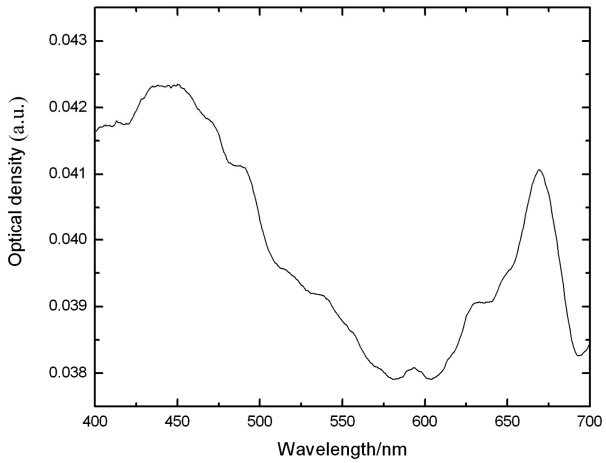

Figure 5. Absorption spectrum of *Skeletonema costatum*.

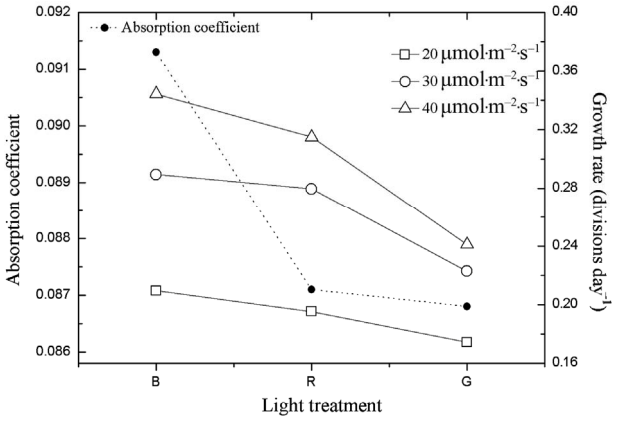

Figure 6. The relationship of Spectrum absorption coefficient and growth rates under blue, green and red light.

Copyright © 2012 SciRes.

lights. Based on the theory of quantum energy level transition, we analysis the results of the experiment and conclude that the wavelength of the light and the corresponding spectrum absorption coefficient play important roles in the energy level transition of molecular photosynthesis. For further illustrating the role of light in the growth condition of *Skeletonema costatum*, we obtain the relationship between spectrum absorption coefficient and growth rate or saturated light intensity. In blue light condition, the value of saturated light intensity is the least (40 $\mu mol \cdot m^{-2} \cdot s^{-1}$), but the spectrum absorption coefficient is the largest ($A_\eta = 0.0913$). In green light condition, the value of saturated light intensity is the largest (50 $\mu mol \cdot m^{-2} \cdot s^{-1}$), but the spectrum absorption coefficient is the least ($A_\eta = 0.0868$). Hence, saturated light intensities are negative correlation with the spectrum absorption coefficient. It also shows that within the saturated light intensity and the same photosynthetic available quantum flux density, the growth rates is the largest under blue light and the least under green light, therefore, the growth rates of *Skeletonema costatum* are positive correlation with the spectrum absorption coefficient. Results presented in this work may offer valuable references for estimating the effect of light wavelength on the growth condition of *Skeletonema costatum* and understanding the mechanism of the red tides occurrence.

5. Acknowledgements

This research is funded by Natural Science Foundation of Shandong Province (No. ZR2010DM009) and the Fundamental Research Funds for the Central Universities (No. 201113011).

REFERENCES

[1] T. J. Smayda, "Harmful Algal Blooms: Their Ecophysiology and General Relevance to Phytoplankton Blooms in the Sea," *Limnology and Oceanography*, Vol. 42, 1999, pp. 1137-1153. doi:10.4319/lo.1997.42.5_part_2.1137

[2] J. S. Xu, "Offshore Shrimp Pond and Red Tide," Marine Press, Beijing, 2003.

[3] M. J. Zhou and M. Y. Zhu, "Progress of the Project Ecology and Oceanography of Harmful Algal Blooms in China," *Advances Earth Science*, Vol. 21, No. 7, 2006, pp. 673-679.

[4] H. L. Cheng, S. H. Lv, C. S. Zhang, *et al.*, "A Survey on the Red Tide of *Prorocentrum donghaiense* in East China Sea," *Ecologic Science*, Vol. 25, No. 3, 2006, pp. 226-230.

[5] Y. S. Lee, "Factors Affecting Outbreaks of High Density *Cochlodinium polykrikoides* Red Tides in the Coastal Seawaters around Yeosu and Tongyeong, Korea," *Marine Pollution Bulletin*, Vol. 52, No. 10, 2006, pp. 1249-1259. doi:10.1016/j.marpolbul.2006.02.024

[6] Y. Li, D. J. Li, J. L. Tang, *et al.*, "Phytoplankton Distribution and Variation in the Yangtze River Estuary and Its Adjacent Sea," *Environmental Science*, Vol. 28, No. 4, 2007, pp. 719-729.

[7] Y. J. Sheng and D. H. Chen, "Effect of Different Light Cycle on the Growth of P. Millirod Algae and Green Millirod Algae," *Journal of Lake Science*, Vol 16, No. 3, 2004, pp. 21-25.

[8] R. Y. Sun, B. Li, G. Y. Zhu, *et al.*, "Ordinary Ecology," Higher Education Press, Beijing, 1993.

[9] W. Wang and J. M. Lin, "Light-Dependent Control and Development of Algae," *Chinese Bulletin of Botany*, Vol. 17, No. 5, 1998, pp. 31-39.

[10] H. B. Seung, S. J. Shimode, Tomohiko, *et al.*, "Growth of Dinoflagellates, *Ceratium furca* and *Ceratium fusus* in Sagami Bay, Japan: The Role of Temperature, Light Intensity and Photoperiod," *Harmful Algae*, Vol. 7, No. 2, 2008, pp. 163-173. doi:10.1016/j.hal.2007.06.006

[11] H. Mao, H. Xu and Z. P. Liu, "Effects of Water Temperature, Illumination, and pH on the Growth of *Chaetoceros curvisetus*," *Ecological Science*, Vol. 26, No. 5, 2007, pp. 432-436.

[12] B. Y. Sun, S. K. Liang, C. Y. Wang, *et al.*, "Role of Irradiance on the Seasonality of *Skeletonema costatum* Cleve Blooms in the Coastal Area in East China Sea," *Environmental Science*, Vol. 29, No. 7, 2008, pp. 1849-1854.

[13] P. Yu, Q. Q. Zhang and X. L. Wang, "Effects of Temperature and Irradiance on Growth of Two Strains of Marine Diatoms," *Marine Environmental Science*, Vol. 25, No. 1, 2006, pp. 38-40.

[14] J. B. Chou, L. H. Hu, S. Z. Lin, *et al.*, "Study on the Productive Culture of *Skeletonema costatum* Goreville," *Shandong Fisheries*, Vol. 23, No. 6, 2006, pp. 27-29.

[15] W. Wang, "Effect of Light Quality on Growth and Biochemical Compositions of a Diatom *Biddulphia sinensis*," *Journal of Wuhan Botanical Research*, Vol. 17, No. 3, 1999, pp. 197-200.

[16] Y. W. Shen, Z. Y. Zhu and Y. D. Liu, "Effects of Different Light Quality on *Richelia sinica*," *Acta Hydrobiologica Sinica*, Vol. 23, No. 3, 1999, pp. 285-287.

[17] Y. Wu and L. Gu, "Study on the Growth and the Light Bioreactor Intracellular Polysaccharide of Two Kinds of Microalgae," *Biotechnology*, Vol. 14, No. 3, 2004, pp. 59-60.

[18] S. Nagasoe, D.-I. Kim, Y. Shimasaki, *et al*., "Effects of Temperature, Salinity and Irradiance on the Growth of the Red Tide Dinoflagellate *Gyrodinium instriatum* Freudemthalet Lee," *Harmful Algae*, Vol. 5, No. 1, 2006, pp. 20-25. doi:10.1016/j.hal.2005.06.001

[19] J. L. Mouget, P. Rosa and G. Tremblin, "Acclimation of *Haslea ostrearia* to Light of Different Spectral Qualities Confirmation of 'Chromatic Adaptation' in Diatoms," *Journal of Photochemistry and Photobiology B*: *Biology*, Vol. 75, No. 1-2, 2004, pp. 1-11. doi:10.1016/j.jphotobiol.2004.04.002

[20] A. J. Mao and J. Wang, "Calculation and Application of Photosynthetic Photon Flux Density," *Periodical of Ocean University of China*, Vol. 36, 2006, pp. 151-155.

Copyright © 2012 SciRes.

Optics and Photonics Journal, **2012, 2, 157-162**
doi:10.4236/opj.2012.23023 Published Online September 2012 (http://www.SciRP.org/journal/opj)

Preparation and Microstructural, Structural, Optical and Electro-Optical Properties of La Doped PMN-PT Transparent Ceramics

Fernando Andrés Londono Badillo, Jose Antonio Eiras, Flavio Paulo Milton, Ducinei Garcia
Ferroelectric Ceramics Group, Physics Department, Federal University of São Carlos, São Carlos, Brazil
Email: flondono@df.ufscar.br

Received June 30, 2012; revised July 27, 2012; accepted August 10, 2012

ABSTRACT

Transparent relaxor ferroelectric ceramics of the system lanthanum modified lead magnesium niobate have been investigated for a variety of electro-optic properties that could make these materials alternatives to $(Pb,La)(Zr,Ti)O_3$. However, a study that relates the to properties in function stoichiometric formula, has not been analyzed heretofore. Therefore, in this work the effect of A-site substitution of La^{3+} in the characterization microstructural, structural, optical and electro-optical on $(1-x)\left[Pb_{(1-3/2y)}La_y\left(Mg_{1/3}Nb_{2/3}\right)O_3\right]-xPbTiO_3$ and $(1-z)\left[(1-x)Pb\left(Mg_{1/3}Nb_{2/3}\right)O_3+xPbTiO_3\right]+zLa_2O_3$ has been performed. It was observed that the properties according to the stoichiometric formula and the PT had a maximum whose behavior was related to the addition of lanthanum in each stoichiometries.

Keywords: Ferroelectric; Optics; Transmittance; Electro-Optical

1. Introduction

Lead magnesium niobato $Pb\left(Mg_{1/3}Nb_{2/3}\right)O_3$ (PMN), as one of the most widely investigated relaxor ferroelectric with a perovskites structure, was first synthesized in the late 1950s [1]. Initially, PMN was prepared by the conventional mixed oxide method, where pyrochlore phase was inevitably produced. In order to synthesize stoichiometric perovskite PMN ceramics, Swartz and Shrout [2] proposed a columbite precursor method, where the intermediate reaction of the formation of pyrochlore phase was bypassed, which results in the stabilization of perovskites structure as compared to the mixed oxide method. Recently, a novel methodology was devised to stabilize perovskites structure by adding stable normal $PbTiO_3$ (PT). The formation of the solid solution increases the tolerance factor and electronegativity difference, leading to the stabilization of the perovskites structure and the enhancement of dielectric property of the relaxor ferroelectric [3].

A study of the optical, electrical and electro-optical properties of PMN-PT ceramics in function of the stoichiometrie is of interest both for possible insight into the physical nature of relaxor ferroelectrics as well as for making practical extension of its several present applications to include usage in electro-optical devices. Present applications take advantages of PMN-PT singularly excellent dielectric, low thermal expansion, and high electrostrictive properties [4]. From the viewpoint of crystal chemistry, the substitution of Ti^{4+} ions for the complex $\left(Mg_{1/3}Nb_{2/3}\right)^{4+}$ ions on the B-site of the perovskite structure in the $(1-x)Pb\left(Mg_{1/3}Nb_{2/3}\right)O_3-xPbTiO_3$ (PMN-PT) system leads to the outstanding properties of the PMN-PT ceramics that exhibit excellent electrical and electro-optical performance, which make them promising applications in multilayer capacitors, piezoelectric transducers and actuators and optical devices [5,6]. However, perovskite structure are extremely difficult to fabricate reproducibly without the appearance of stable pyrochlore phase, which always exist in the PMN-PT ceramics and significantly deteriorates such properties as the dielectric property [7].

The optical transmittance as function of wavelength was studied in $Pb\left(Mg_{1/3}Nb_{2/3}\right)_{0.62}Ti_{0.38}O_3$ single crystal by Wan *et al.* It was found that the crystal is transparent in the visible region and rolls off in near 450 nm. Using the Senarmont compensador method, the effective electro-optic coefficient r_c = 42.8 pm/V was also obtained [8]. Some effect and applications, such as photorefractive, Second-Harmonic Generation (SHG), electro-optic and elasto-optical devices, are based on the large optical property coefficient of the materials [9,10]. The knowledge of factors that can modify these properties is desirable to find new application of the relaxor and elec-

Copyright © 2012 SciRes.

tro-optical materials. In this work, ceramics in the PMN-PT system were prepared by doping with lanthanum. La addition to PMN-PT has been shown to promote densification and through hot uniaxial pressing, optically transparent materials have been achieved, allowing the determination of various optic and electro optic properties [11,12].

It is the purpose of this article, to report the microstructural, structural, electrical, optical and electro-optical properties according to the stoichiometric formula of lanthanum doped PLMN-XPT and PMN-XPT:La with $0.11 \leq x \leq 0.15$.

2. Experimental Procedure

The powder was synthesized by the columbite or two-stage calcining method [2]. The batch formulae were $(1-x)\left[\mathrm{Pb}_{(1-y)}\mathrm{La}_{y}\left(\mathrm{Mg}_{1/3}\mathrm{Nb}_{2/3}\right)\mathrm{O}_{3}\right]-x\mathrm{PbTiO}_{3}$ PLMN-XPT, and $(1-z)\left[(1-x)\mathrm{PbLa}\left(\mathrm{Mg}_{1/3}\mathrm{Nb}_{2/3}\right)\mathrm{O}_{3}-x\mathrm{PbTiO}_{3}\right]+z\mathrm{LaO}_{3/2}$ PMN-XPT:La, with $y = 0.01$. $z = 0.01$, X = 100 x and $0.11 \leq x \leq 0.15$. The starting materials were lanthanum oxide, La_2O_3 (Aldrich, >99% purity), niobium oxide, Nb_2O_5 (Alfa Aesar 99.9% purity), magnesium carbonate hydroxide pentahydrate, $(MgCO_3)4{\cdot}Mg(OH)_2{\cdot}5H_2O$ (Aldrich 99% purity), lead oxide, PbO (MGK 99%) and titanium oxide, TiO_2 (Alfa Aesar, 99.8% purity) powders. The $(MgCO_3)4{\cdot}Mg(OH)_2{\cdot}5H_2O$ was carried up to 1100˚C, for 4 h, to drive off CO_2 and H_2O and obtain the correct amount of MgO for a stoichiometric reaction with Nb_2O_5. In the first stage, MgO and Nb_2O_5 powders were ball-milled and prereacted at 1100˚C for 4 h, in air, to form the columbite phase ($MgNb_2O_6$). In the second stage, the synthesized $MgNb_2O_6$ (MN) was ball-milled in isopropanol, for 24 h, with appropriate amounts of PbO, TiO_2 and La_2O_3 and heated at 900˚C, for 4 h, in oxygen atmosphere, at a controlled pressure of 200 kPa. The calcined powders were pressed into pellets 10 mm in diameter and 10 mm in thickness with the addition of an appropriate amount of polyvinyl alcohol (PVA) binder. The pellets were sintered in hot uniaxial pressing in O_2 atmosphere followed for 4 h at 1220˚C, and 6 MPa.

The phases and the structural parameters were determined by X-ray diffraction (XRD) using a Rigaku diffractometer, with CuKα radiation. The lattice parameters were calculated by least squares from the positions of the diffraction peaks. Apparent densities were determined by the Archimedes method. The microstructural features of the samples were investigated by scanning electron microscopy (SEM), using a Jeol JSM 5800 LV. The grain sizes were calculated from the SEM images of the polished thermally etched surfaces by the linear-intercept method. For dielectric measurement, gold electrodes were deposited on both faces of the disk samples (5 mm diameter and ~1.0 mm thick). The relative permittivity, ε was measured by impedance analysis (HP4194A). The transmittance was measured in a spectrophotometer (Micronal-B582), at wavelengths ranging from 200 to 1000 nm for optically polished samples, 600 μm thick. The method used in the electro-optical characterization, determination of the Pockels and Kerr coefficients, is based in the Senarmont configuration illustrated in the **Figure 1** [13]. The birefringence medium (sample) is located between two linear polarizer's, P_1 and P_2, where the P_2 polarizer is known as analyzer, whit polarizer axis forming angles of ±45˚ in relation to principal axis of the sample, this definite by the electric-field direction applied. Between the sample and the analyzer is located a $\lambda/4$ plate used to compensation the effects caused by the natural birefringence of the medium. Then the analyzer is positioned in the angle β that optimizes the relation between the birefringence and the applied electric-field. In the Equation (1) is presented the relation between birefringence and electric-field for medium with linear and quadratic electro-optic response.

$$\Delta n\left(E\right) = -1/2n^3\left(rE + RE\right) \tag{1}$$

where Δn is the birefringence induced for the electric-field E, n is the natural birefringence of the medium, r and R are the Pockels and Kerr electro-optic coefficients, respectively.

3. Results and Discussion

The relative density of PLMN-XPT and PMN-XPT:La at different PT concentration are greater than 96% of the theoretical density as can be seen in **Figure 2**, which is especially suitable for electronic industry application [14]. The relative density of the two system exhibits the tendency to decrease when PT concentration is increased. This can be attributed the loss of PbO (control atmosphere of PbO was not used in this work) [15]. As well can be seen the relative densities of PLMN-XPT ceramics is greater for all PT concentrations when compared with PMN-XPT:La. This possibly associated with the less occupation of La^{3+} in Pb^{2+} sites, implying in the appearance of vacancies in the A and B sites in different quantities [16] (La^{3+} atoms are lighter than Pb^{2+} atoms, and PMN-XPT:La have major number of La atoms).

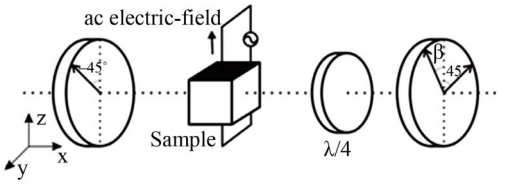

Figure 1. Illustration of the experimental Senarmont method for characterization of the transversal electro-optical effect.

Copyright © 2012 SciRes.

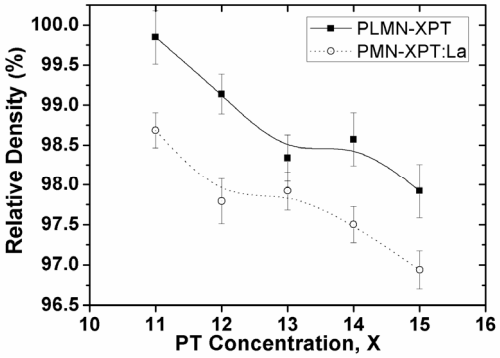

Figure 2. Variation of relative density as a function of PT concentration of the PLMN-XPT and PMN-XPT:La ceramics with $0.11 \leq x \leq 0.15$.

The variation of density is considered as relating to mass loss induced by evaporation of PbO or to variation of temperature of densification relating to the increase of PT, this changes the grain size, porosity could appear which decreases the relative density of ceramics. However the slight decrease of relative density of PLMN-XPT and PMN-XPT:La ceramics can be attributed to the variation of microstructure and to evaporation of lead at elevated sintering temperatures.

The high densification of PLMN-XPT and PMN-XPT:La ceramics is further confirmed by SEM observation, which is shown in **Figure 3**. All ceramics exhibited similar microstructure as can be seen in the micrograph of polished and thermally attacked surface of PLMN-13PT (shown here).

The variation of grain size with the increase of PT concentration is shown in **Figure 4**. An increase in PT concentration resulted in a decrease in grain size and a corresponding slight decrease in density [17]. The grain size in PMN-XPT:La is lesser for all concentration when compared to PLMN-XPT because the major quantities of La^{3+} resulted in reduction of grain size as observed by Kim *et al.* in La^{3+} doped PMN-PT ceramics [18].

The XRD patterns of sintered ceramics with different compositions are presented in **Figure 5**, where a complete perovskite structure (JCPDS 391488) is formed and the pyrochlore or other second phases were not detected.

The permittivity (real, ε' and imaginary, ε'') was measured at various temperatures in the frequency range 1 kHz - 1MHz. In the **Figure 6** can be seen a typical examples of measurements realized in this work. All the samples exhibit typical relaxor behavior [19,20], with the magnitude of ε' decreasing with increasing frequency, and the maximum permittivity real, ε'_{max} shifting to higher temperatures, as shown in the PLMN-12PT ceramics (**Figure 6**). The data of all ceramic analyzed in this work can be seen in the **Table 1**.

Variations in the shape of ε' in function of T curves can be also directly related to the diffuseness coefficient,

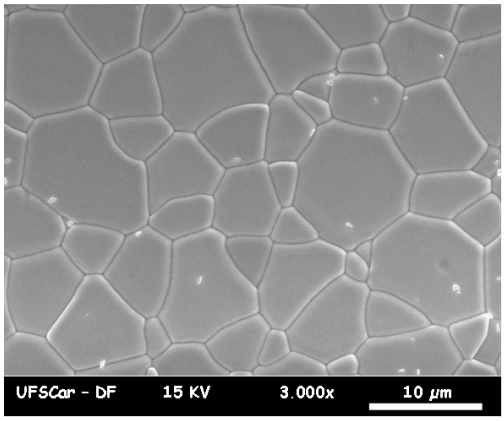

Figure 3. SEM image of surfaces polished and thermally attacked of PLMN-13PT ceramic.

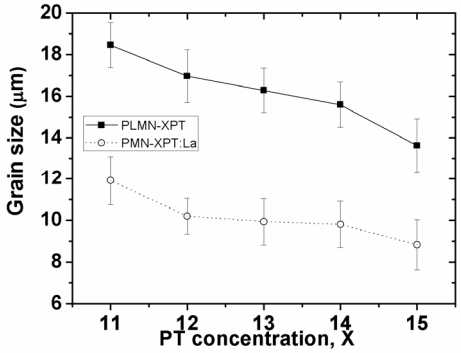

Figure 4. Grain size in function of PT concentration of the PLMN-XPT and PMN-XPT:La ceramics with $0.11 \leq x \leq 0.15$.

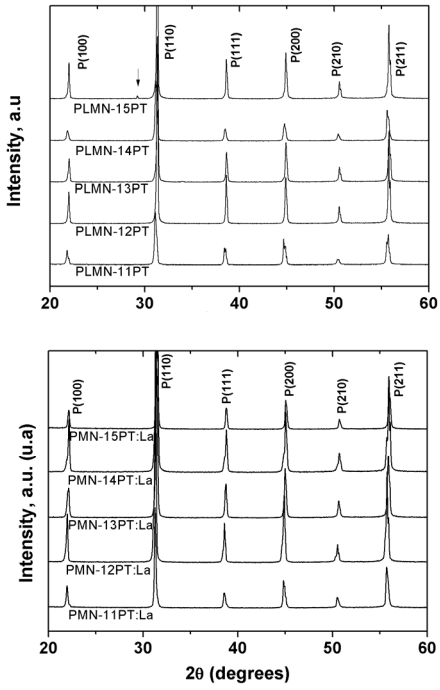

Figure 5. XRD patterns of PLMN-XPT and PMN-XPT:La ceramics with $0.11 \leq x \leq 0.15$.

Copyright © 2012 SciRes.

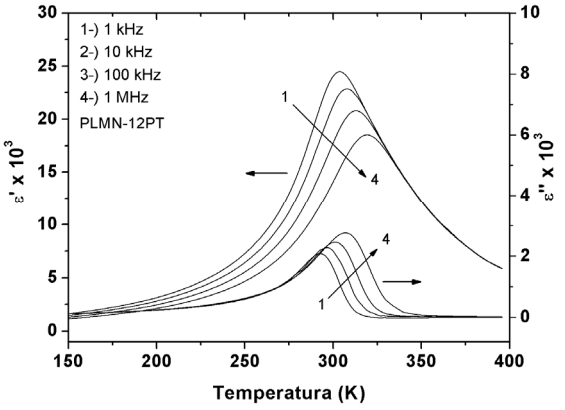

Figure 6. Permittivity real, ε' and permittivity imaginary, ε'' at various frequencies in function of temperature for PLMN-XPT and PMN-XPT:La ceramics with $0.11 \leq x \leq 0.15$.

Table 1. Dielectric properties of PLMN-XPT and PMN-XPT: La with $0.11 \leq x \leq 0.15$ at 1 kHz.

Ceramic	ε'_{max}	T_{max} (K)	Δ
PLMN-11PT	27,000	293	1.66
PLMN-12PT	26,800	300	1.65
PLMN-13PT	25,200	305	1.63
PLMN-14PT	29,000	308	1.53
PLMN-15PT	28,000	317	1.55
PMN-11PT:La	25,000	297	1.62
PMN-12PT:La	24,700	299	1.62
PMN-13PT:La	25,100	308	1.62
PMN-14PT:La	23,000	318	1.60
PMN-15PT:La	30,000	319	1.52

δ in **Table 1**, calculated from the Santos Eiras equation [21], which for relaxors reflect the level of disorder in term of the diffusivity of the ε'_{max}. As can be deduced from **Table 1**, the value of ε'_{max} for PMN-XPT:La^{3+} are smaller that PLMN-XPT, inferring that lanthanum additions result in the reduction in ε'_{max}, while increasing the degree of ordering, as observed for Kim *et al.* [18].

The transmission spectrum as a function of wavelength (200 nm - 1100 nm) of PLMN-XPT and PMN-XPT:La ceramics with $0.11 \leq x \leq 0.15$ and 630 μm thickness is presented in **Figure 7**. For both of these stoichiometries formula the percentage of transmitted light begins to rise abruptly at just below 380 nm and then increases only gradually with wavelength about 500 nm. This gradual increase in transmittance continues into the near IR at least through 1100 nm without any noticeable absorption band being observed. This is similar to what was observed for most crystals with oxygen-octahedral perovskites structure [22-24]. From the transmission characterization, we can see that the optical absorption is very small at higher wavelength range. In general, optical transmission relates to reflection loss and scattering loss. Using the refractive indices measured by Mchenry *et al.* [12], e by the Fresnel expression, the reflection loss of the light at two surfaces was calculated about 20%. Beyond of reflection loss is observed loss by scattering which can be attributed the dispersion by ferroelectrics domain (spontaneous birefringence), increases in the porosity (by loss of PbO) and precipitation of spurious phases. In general the addition of PT increase the transmittance both the PLMN-XPT and PMN-XPT:La, nevertheless exist a concentration optimal of PT in 14%. As previously mentioned the increase of content of PT promotes the densification of the samples, favoring the transmittance, though the sample with PMN-XPT:La present less transmission in comparison with the PLMN-XPT in function of wavelength. This effect is attributed the replacement of lanthanum ions in the sites of the lead, that increased the number of vacancies reducing the density and consequently affecting the transmittance.

In the **Table 2** can be seen the values for the electro-optic Kerr coefficients as a function of PT concentration and stoichiometric formula, which were determined under frequency of 200 Hz, at room temperature. The values of electro-optical coefficients here obtained are similar the reported in literature for La doped PMN-PT ce-

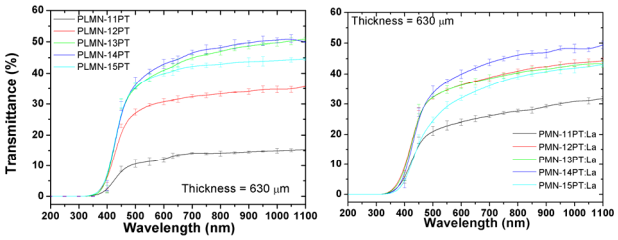

Figure 7. Percent transmission as a function of wavelength for optically polished PLMN-XPT and PMN-XPT:La with $0.11 \leq x \leq 0.15$ and 630 μm thickness.

Table 2. Electro-optical coefficient, *R* of PLMN-XPT and PMN-XPT:La with $0.11 \leq x \leq 0.15$ calculated under frequency of 200 Hz.

Ceramic	R ($\times 10^{-16}$ m^2/V^2)
PLMN-11PT	8.0
PLMN-12PT	14.1
PLMN-13PT	23.7
PLMN-14PT	10.1
PLMN-15PT	10.3
PMN-11PT:La	7.1
PMN-12PT:La	10.3
PMN-13PT:La	13.0
PMN-14PT:La	9.2
PMN-15PT:La	6.1

Copyright © 2012 SciRes.

ramics [12,25] and greater to commercial PLZT ceramics [26]. The Kerr coefficients of the PLMN-XPT ceramics are higher when compared with PMN-XPT:La ceramics because of their major transmittance, since that the phase induced by electro-optical effect is directly proportional intensity of light transmission [27].

4. Conclusion

The ceramics obtained in this study showed high dense and homogeneous microstructure, independent of the stoichiometric which were obtained. The La addition to the PLMN-XPT and PMN-XPT:La relaxor ferroelectric system was found to promote densification and inhibit grain growth, however the PMN-XPT:La ceramic to present smaller density in relation to other composition. The transmittance characterization revealed a transmission of about 50% from 0.45 μm to 1.1 μm, presenting a lower transmission in the samples of PMN-XPT:La. The quadratic electro-optic coefficients, calculated from measurements of birefringence in this work to PMN-XPT and PLMN-XPT ceramics are up to two times higher than the maximum reported for PLZT. Thus confirming the potential use of these system as substitutes for PLZT in electro-optical applications.

5. Acknowledgements

To CAPES, FAPESP and CNPq for the financial support. To Dr. Y. P. Mascarenhas (São Carlos Physics Institute at the University São Paulo), for the use of the XRD laboratory facilities. And to Mr. Francisco José Picon for the technical support.

REFERENCES

[1] G. A. Smolenskii and A. I. Agranovskaya, "Dielectric Polarization and Losses of Some Complex Compounds," *Soviet Physics—Technical Physics*, Vol. 3, No. 7, 1958, pp. 1380-1382.

[2] S. L. Swartz and T. R. Shrout, "Fabrication of Perovskite Lead Magnesium Niobate," *Materials Research Bulletin*, Vol. 17, No. 10, 1982, pp. 1245-1250. doi:10.1016/0025-5408(82)90159-3

[3] T. R. Shrout and A. Halliyal, "Preparation of Lead-Based Ferroelectric Relaxors for Capacitors," *The Bulletin of the American Ceramic Society*, Vol. 66, No. 4, 1987, pp. 704-711.

[4] S. J. Jang, K. Uchino, S. Nomura and L. E. Cross, "Electrostrictive Behavior of Lead Magnesium Niobate Based Ceramic Dielectrics," *Ferroelectrics*, Vol. 27, No. 1, 1980, pp. 31-34. doi:10.1080/00150198008226059

[5] Y. H. Chen, K. Uchino, M. Shen and D. Viehland, "Substituent Effects on the Mechanical Quality Factor of $Pb(Mg_{1/3}Nb_{2/3})O_3$-$PbTiO_3$ and $Pb(Sc_{1/2}Nb_{1/2})O_3$-$PbTiO_3$ Ceramics," *Journal of Applied Physics*, Vol. 90, No. 3, 2001, pp. 1455-1458. doi:10.1063/1.1379248

[6] L. B. Kong, J. Ma, W. Zhu and O. K. Tan, "Rapid Formation of Lead Magnesium Niobate-Based Ferroelectric Ceramics via a High-Energy Ball Milling Process," *Materials Research Bulletin*, Vol. 37, No. 3, 2002, pp. 459-465. doi:10.1016/S0025-5408(01)00823-6

[7] E. M. Jayasingh, K. Prabhakaran, R. Sooraj, C. Durgaprasad and S. C. Sharma, "Synthesis of Pyrochlore Free PMN-PT Powder by Partial Oxalate Process Route," *Ceramics International*, Vol. 35, No. 2, 2009, pp. 591-596. doi:10.1016/j.ceramint.2008.01.022

[8] X. M. Wan, H. Q. Xu, T. H. He, D. Lin and H. S. Luo, "Optical Properties of Tetragonal $Pb(Mg_{1/3}Nb_{2/3})_{0.62}$-$TiO_{0.38}$ Single Crystal," *Journal of Applied Physics*, Vol. 93, No. 8, 2003, pp. 4766-4768. doi:10.1063/1.1561991

[9] A. S. Bhalla, R. Guo, A. S. Cross, G. Burns, F. H. Dacol and R. R. Neurgaonkar, "Glassy Polarization in the Ferroelectric Tungsten Bronze $(Ba,Sr)Nb_2O_6$," *Journal of Applied Physics*, Vol. 71, No. 11, 1992, pp. 5591-5595. doi:10.1063/1.350537

[10] A. S. Bhalla, R. Guo, A. S. Cross, G. Burns, F. H. Dacol and R. R. Neurgaonkar, "Measurements of Strain and the Optical Indices in the Ferroelectric $Ba_{0.4}Sr_{0.6}Nbz$: Polarization Effects," *Physical Review B*, Vol. 36, No. 4, 1987, pp. 2030-2035. doi:10.1103/PhysRevB.36.2030

[11] F. A. Londono, J. A. Eiras and D. Garcia, "New Transparent Ferroelectric Ceramics with High Electro-Optical Coefficients: PLMN-PT," *Cerâmica*, Vol. 57, No. 344, 2011, pp. 404-408.

[12] D. A. Mchenry, J. Giniewicz, S. J. Jang, A. Bhalla and T. R. Shrout, "Optical Properties of Hot Pressed Relaxor Ferroelectrics," *Ferroelectrics*, Vol. 93, No. 1, 1989, pp. 351-359. doi:10.1080/00150198908017367

[13] R. Go, "Ferroelectric Properties of Lead Barium Niobate Compositions near the Mosphotropic Phase Boundary," Ph.D. Theses, Pennsylvania State University, Pennsylvania, 1990.

[14] C. Ding, *et al*., "Phase Structure and Electrical Properties of $0.8Pb(Mg_{1/3}Nb_{2/3})O_3$ Relaxor Ferroelectric Ceramics Prepared by the Reaction-Sintering Method," *Physica Status Solidi* (*A*), Vol. 207, No. 4, 2010, pp. 979-985. doi:10.1002/pssa.200925377

[15] G. S. Snow, "Fabrication of Transparent Electrooptic PLZT Ceramics by Atmosphere Sintering," *Journal of the American Ceramic Society*, Vol. 56, No. 2, 1973, pp. 91-96. doi:10.1111/j.1151-2916.1973.tb12365.x

[16] S. M. Gupta and D. Viehland, "Role of Charge Compensation Mechanism in La-Modified $Pb(Mg_{1/3}Nb_{2/3})O_3$-$PbTiO_3$ Ceramics: Enhanced Ordering and Pyrochlore Formation," *Journal of Applied Physics*, Vol. 80, No. 10, 1996, pp. 5875-5883. doi:10.1063/1.363581

[17] N. Kim, D. A. McHenry, S. J. Jang and T. R. Shrout, "Fabrication of Optically Transparent Lanthanum Modified $Pb(Mg_{1/3}Nb_{2/3})O_3$ Using Hot Isostatic Pressing," *Journal of the American Ceramic Society*, Vol. 73, No. 4, 1990, pp. 923-928. doi:10.1111/j.1151-2916.1990.tb05137.x

[18] N. Kim, W. Huebner, S. J. Jang and T. R. Shrout, "Dielectric and Piezoelectric Properties of Lanthanum-Modified Lead Magnesium Niobium-Lead Titanate Ceram-

Copyright © 2012 SciRes.

ics," *Ferroelectrics*, Vol. 93, No. 1, 1989, pp. 341-349. doi:10.1080/00150198908017366

[19] L. E. Cross, S. J. Jang, R. E. Newnham, S. Nomura and K. Uchino, "Large Electrostrictive Effects in Relaxor Ferroelectrics," *Ferroelectrics*, Vol. 23, No. 1, 1980, pp. 187-191. doi:10.1080/00150198008018801

[20] K. Uchino, S. Nomura, L. E. Cross, S. J. Jang and R. E. Newnham, "Electrostrictive Effect in Lead Magnesium Niobate Single Crystals," *Journal of Applied Physics*, Vol. 51, No. 2, 1979, pp. 1142-1145. doi:10.1063/1.327724

[21] I. A. Santos and J. A. Eiras, "Phenomenological Description of the Diffuse Phase Transitiion Inferroelectrics," *Journal of Physics*: *Condensed Matter*, Vol. 13, No. 50, 2001, pp. 11733-11740. doi:10.1088/0953-8984/13/50/333

[22] X. M. Wan, H. S. Luo and X. Y. Zhao, "Refractive Indices and Linear Electro-Optic Properties of $(1-x)Pb(Mg_{1/3}Nb_{2/3})O_3-xPbTiO_3$ Single Crystals," *Applied Physics Letters*, Vol. 85, No. 22, 2004, pp. 5233-5235. doi:10.1063/1.1829393

[23] C. J. He, L. H. Luo and X. Y. Zhao, "Optical Properties of Tetragonal Ferroelectric Single Crystal Lead Magnesium Niobate Lead Titanate," *Journal of Applied Physics*, Vol. 100, No. 1, 2006, Article ID: 013112. doi:10.1063/1.2217487

[24] F. A. Londono, J. Eiras and D. Garcia, "Optical and Electro-Optical Properties of $(Pb,La)TiO_3$ Transparent Ceramics," *Optical Materials*, Vol. 34, No. 8, 2012, pp. 1310-1313. doi:10.1016/j.optmat.2012.02.020

[25] K. Uchino, "Ferroelectric Devices," Marcel Dekker, New York, 2000.

[26] K. Uchino, "Electro-Optic Ceramics and Their Display Applications," *Ceramics International*, Vol. 21, No. 5, 1995, pp. 309-315. doi:10.1016/0272-8842(95)96202-Z

[27] A. Yariv and P. Yeh, "Optical Waves in Crystals: Propagation and Control of Laser Radiation," John Wiley & Sons, New York, 1984.

Copyright © 2012 SciRes.

Optics and Photonics Journal, **2012, 2, 163-166**
doi:10.4236/opj.2012.23024 Published Online September 2012 (http://www.SciRP.org/journal/opj)

New Technology for Grids and Scales Manufacturing in Optical Devices

Vladimir Stepanovich Kondratenko, Vladimir Yeugenyevich Borisovskiy, Alexander Sergeevich Naumov, Nikolay Eduardovich Petruljanis
Moscow State University of Instrument Engineering and Computer Science (MGUPI), Moscow, Russia
Email: Kondratenko_vs@mgupi.ru

Received June 2, 2012; revised July 1, 2012; accepted July 11, 2012

ABSTRACT

Using the laser controlled thermocracking method, research results for the new technology of optical grids and scales manufacturing are given in this paper. The opportunity of grids and scales manufacturing is shown for a wide range of the sizes, scale's pitches and its width: From 10 nanometers up to 10 microns with a backlight in various optical ranges.

Keywords: Laser Controlled Thermocracking; Microcrack; Grids and Scales; Disperse System; Luminescent Compounds

1. Introduction

In the manufacture of many optical devices, one of the most important process steps is grids and scales making on this devices. Grid and scale are used to make the sampling, measurement and also for pointing the device at the subject.

Most of the grids and scales are applied for the parallel sided plate's surface, which are predominantly placed in the focal plane of the oculars of the optical system [1].

Depending on the tolerances for linear and angular dimensions, grids are subdivided into three categories:

- Rough grids: Where the tolerance of the linear sizes is more than 100 microns and angular one are more than 5 minutes;
- Normal grids: Where the tolerance of the linear sizes is in the range from 10 to 100 um and angular one are in the 1 - 5 minutes range;
- Precise grids: Where the tolerance of the linear sizes is in the range from 1 to 10 um and angular one are in the 1 - 60 seconds range.

Conventionally, there are two fundamentally different application methods of grids making, which are chosen depending on the configuration of the line and the required class of accuracy. One of that is the method of division, and other photolithography method.

The method of division includes two types:

1) Line making by a diamond cutter directly on the glass surface (mechanical method). It is used in the manufacture of grids with width from 0.5 up to 10 um.

2) Grid making is by scribing of protective layer that cover the glass surface with its following etching (glazing of the protective layer). This method allows obtaining of lines with a 10 - 20 um.

Photolithography allows get a complex drawings with high accuracy of size, but that is technologically complicated. The minimum width of the lines, which can be obtained by this way, is 3 um [1].

Recently laser controlled thermocracking (LCT) method has got a wide application for the precise cutting of brittle non-metallic materials [2,3].

2. The Use of the LCT

The formation of separating cracks occurs due to the tension stress arising as a result of a material surface heating by a laser radiation with following cooling of the heating zone by a coolant. The crack is formed in the material because of the impact of tension stresses where the cutting depth can be tuned from several microns up to through cut. Using air-water aerosol as a coolant during a cutting process, this crack can be visually observed in about the 3 - 10 mm distance after the water jet stream (**Figure 1**), from the place of that forming. Then the microcrack is closed because of stresses arising in the volume of material in the moment of microcrack formation. The microcrack is fully interlocked because of the edge of one does not have any defects and that becomes visually invisible. Therefore, the use of such microcracks as optical lines and grids is not possible. In addition, when cutting of materials by microcrack (pre-cut) it creates difficulties in following braking of the workpiece into the separate parts which often leads to the yield decreasing.

The task of lines and grids making for optical instruments has been successfully solved using LCT method

Copyright © 2012 SciRes.

for the quartz glass [4]. In this case, due to the presence of residual thermostress along the cutting line, the microcrack closing is not happened. Varying the relative parameters of the LCT process, namely the feed rate of relative movement and the density of the laser radiation power, it is possible to control the microcrack with strictly defined geometrical parameters as width and depth. The tunable range of these parameters is very wide. For instance, when reducing the feed rate of relative movement during LCT process from 50 mm/sec down to 10 mm/sec, the width of microcracks is practically linearly increases from 0.5 to 8 um (**Figure 2**).

During R & D of the LCT method with using of different mixed compounds for the coolant the fundamentally new application method has been developed for grids and scales making for surfaces of optical parts [5]. This method carries the formation of microcrack in the glass surface with the width and depth, and it also carries filling the microcrack by various compounds for its visualization, and it also carries the control of optical and geometric parameters of this microcrack.

To obtain a visible cutting line (microcrack) with the specified width and depth it is necessary to use a coolant with the two-level dispersion consisting from a dispersion air environment and the two-phase compound of disperse phase. Thereby the first dispersed phase includes water drops and the second disperse phase includes the colloid compound or solid microparticles.

In addition, for microcracks visualization, cooling of the cutting line can be realized with the coolant in the form of a disperse system containing particles of different colors in the dispersed phase or with the injection in the composition of the disperse phase using disperse coloring agents with different colors or colored solutions.

The line making process by LCT method is as follows (**Figure 1**). When local heating of glass workpiece 1 by laser elliptical beam 2 is focused through spherical and cylindrical lenses 3 compression stresses is created in the material surface layer, which do not exceed the strength of the material and does not lead to its damage. Following sharp cooling of the heating zone by the coolant 5 sprayed into a heating zone by nozzle 4 leads to transforming of compression stresses to tensile stresses, which exceed the strength of the glass and lead microcrack creating in the glass surface 6. Solid particles of the dispersed phase that are in the composition of the coolant put in the microcrack when nozzle spraying and that particles are fixed inside microcrack then preventing its collapse (closing or growing together).

For instance, the special dispersed suspension was used as a coolant, where the dispersive environment was the air-water mixture and the disperse phase was a water dispersion of silica where the average SiO_2 particle size was about 10 nm. When you move the sample glass with a 250 mm/s feed rate, the laser beam is pre-cut with 120 microns microcrack depth, thus the width of one was 2 microns.

Using phosphor solutions in the disperse phase, the microcrack will be illuminated as a glowing line (**Figure 3(a)**) if to backlight transversely and it will be dark black line (**Figure 3(b)**) if to backlight in longitudinal manner. Crack depths were gotten by LCT method with a range from tens to several hundreds of micrometers. The width of that may be varied from tens of nanometers (when using concentrated colloidal solutions) and to tens of micrometers (when using solid fine-dispersed powders).

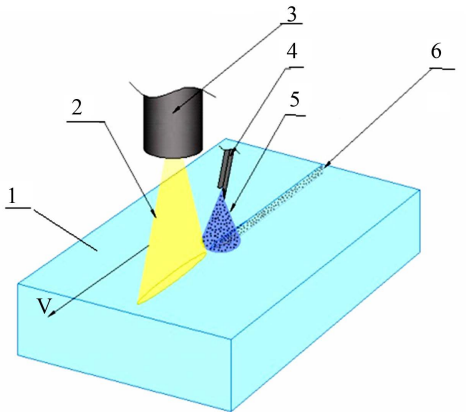

Figure 1. Scheme is the microcrack formation in the glass: 1—A glass workpiece; 2—The laser beam; 3—Focusing lens; 4—Water jet; 5—Coolant; 6—Microcrack.

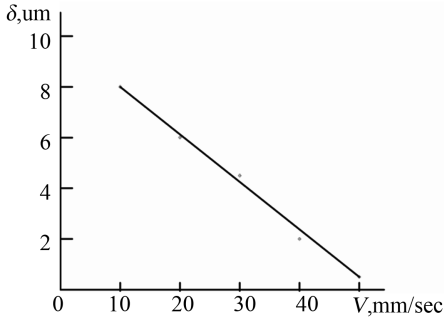

Figure 2. The dependence of the line's (microcrack) width δ from the feed rate V when LCT method.

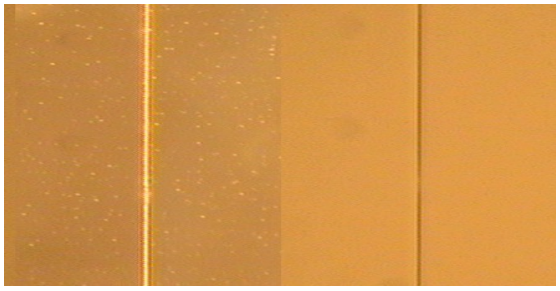

Figure 3. Microcrack view is with backlight (a) and without backlight (b).

Copyright © 2012 SciRes.

Figure 4 shows results of microcrack geometrical parameters measurements filled by a phosphor that was measured on the tunnel microscope Supra 50 VP LEO.

The main advantage of developed technology in that the production of grid lines is the single technological cycle, *i.e.* following etching and line painting is not required (as for the mechanical method) and there are no complex technological processes (as for the photolithography). The speed of the line making is a few hundred millimeters per second.

An important advantage of this method is that practically any material can be put into the microcrack (in the form of fine particles) with required optical properties, without worrying about the presence or absence of adhesion to a glass.

For some of optical devices, in particular, night vision devices, one of the main requirements is to ensure the visibility of the grid lines on a dark background. The part of light is scattered on the glass surface and smallest defects (if it there are) at the common backlight. It gives a common light background that confuses the outlook. In these cases an effective solution is luminescent lines making, which lets be highlighted by ultraviolet light that is invisible for the human eye (**Figure 5(a)**). Manufacturing of such lines by traditional methods is difficult because not all of phosphors have a good adhesion to a glass. Using the LCT method, this kind of the problem doesn't arise. Various phosphors (including organic) can be successfully used with the possibility of obtaining different lines colors and backlight in the different spectral range (**Figure 5(b)**). Varying by phosphor concentration in the coolant, it gives lines with a different intensity of the glow. The width of the grid lines is only a few hundredths of a micron but they are clearly visible as clear luminous lines, both as in case of magnification and with the naked eye.

It should be noted that the described method for optical line application is not limited for continuous lines. **Figure 6** shows photos of the dash line (a) and dash quintuple-dot line (b) that was obtained by the LCT method. It is available to make many kinds of linetypes depending on the request.

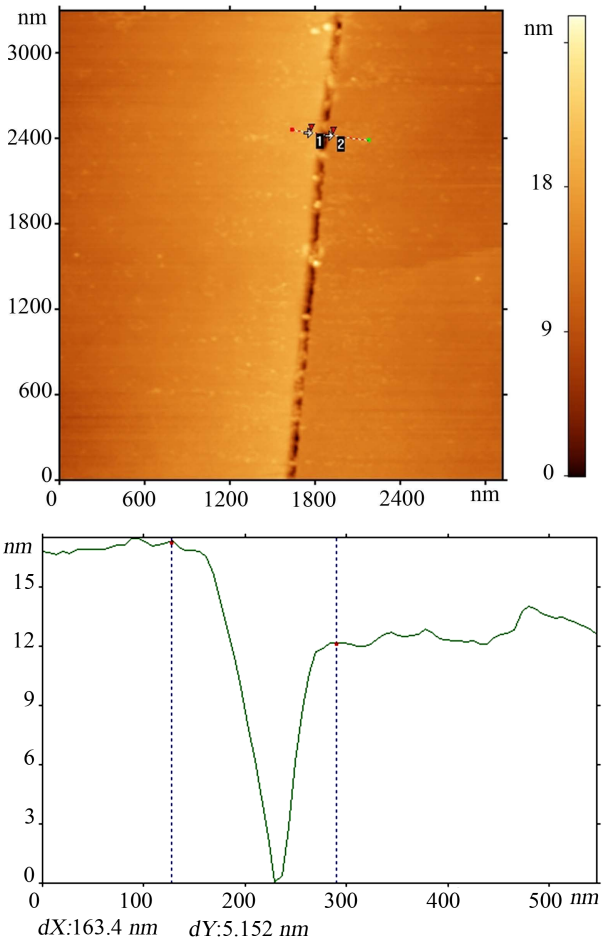

Figure 4. Results are measurements of geometrical parameters of microcrack filled by a phosphor. Measuring equipment is the tunnel microscope Supra 50 VP LEO.

3. Conclusions

The new high-effective method allows to obtain optical tags: Line, mark, risk, grid, etc. with the set of geometrical parameters that impossible to get using conventional technologies.

In addition, the described method [5] provides the possibility to make wiring in the glass (for instance) filling

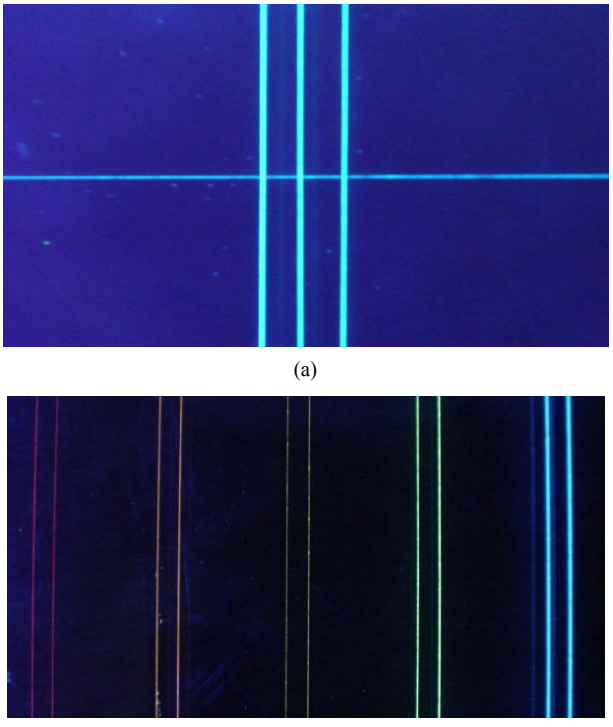

(a)

(b)

Figure 5. Luminous lines of blue (a) and different colors (b).

Copyright © 2012 SciRes.

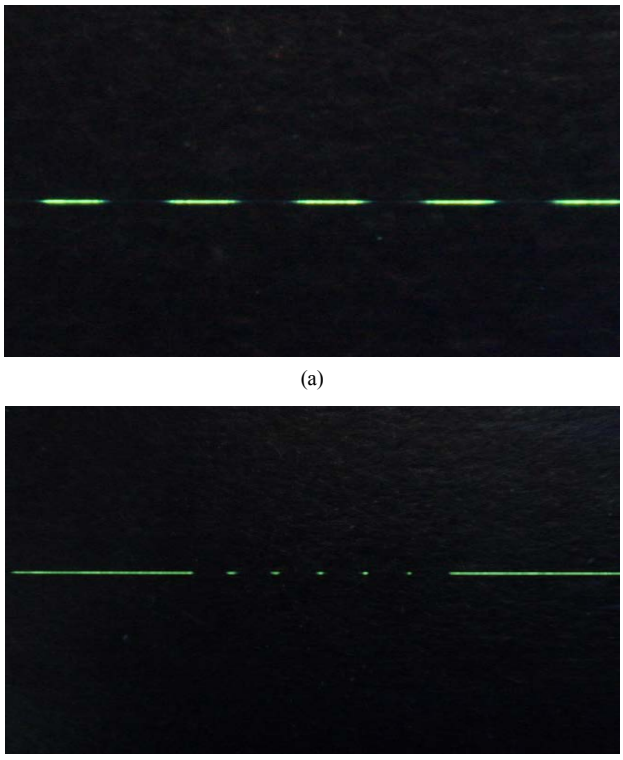

(a)

(b)

Figure 6. The dash line (a) and dash quintuple-dot line (b) photos obtained by the LCT method.

the microcrack by metal current-conducting nanopowders and it provides to get glowing grooves using luminescent compounds. It can be widely used in the building market, for some new generation devices and products.

The fulfilled complex of works in fundamental and applied research of the LCT method shows the competitiveness of the Russian scientific school in the field of high technologies.

Many researches in this paper were done in accordance with the Government Decree of the Russian Federation No. 218, dated 9 April, 2010, on the basis of a Contract 13. G25. 31.0020 between the Ministry of Education and Science of the Russian Federation and JSC "MZ 'Sapphire'" in creation of hi-tech production manufacturing.

REFERENCES

[1] L. M. Krivoviaz, D. T. Puriaev and M. A. Znamenskaya, "The Practice of Optical Measuring Laboratory," Machinery, Moscow, 2004, 333 p.

[2] V. S. Kondratenko, "Method of Cutting of Brittle Material," the Patent of Russian Federation, No. 2024441, 1991.

[3] I. V. Golubjatnikov, V. S. Kondratenko and A. B. Zhymalov, "Development of the Theory and Practice of a Method Laser Controlled Thermocracking," *Instruments*, Vol. 12, No. 114, 2012, pp. 1-6.

[4] V. S. Kondratenko, V. I. Gundiak and V. Y. Bersenyev, "Application of the Method of Laser Controlled Thermocracking of a Glass in the Production of Optical Parts—Electronic Engineering, Ser," *Laser Technology and Optoelectronics*, *Ser. Electronic Engineering*, Vol. 4, No. 56, 1990, pp. 70-71.

[5] V. S. Kondratenko, "Method of Cutting of Brittle Non-Metallic Materials (Two Variants)," The Patent of Russian Federation, No. 2333163, 2007.

Copyright © 2012 SciRes.

Optics and Photonics Journal, 2012, 2, 167-172
doi:10.4236/opj.2012.23025 Published Online September 2012 (http://www.SciRP.org/journal/opj)

Simulation of Diode-Pumped Q-Switched Nd:YAG Laser Generating Eye-Safe Signal in IOPO Environment

Mian M. Ashraf*, Muhammad Siddique
Institute of Industrial Control System, Rawalpindi, Pakistan
Email: *ashrafmian@hotmail.com, mrsiddik@yahoo.com

Received June 18, 2012; revised July 20, 2012; accepted July 30, 2012

ABSTRACT

Numerical simulation of diode-pumped Q-switched Nd:YAG laser leading to the generation of eye-safe signal in singly resonant Intra-cavity Optical Parametric Oscillator (IOPO) is presented. Starting from rate equations, the time dependent laser equations have been solved numerically, whereas the space-dependent OPO equations analytically. Our results show that 1.4 J diode laser (810 nm) pulse with 200 μsec width, delivers 30 mJ Nd:YAG laser (1064 nm) pulse with 5 n-second width. This Nd:YAG laser further generates 9 mJ eye safe signal (1570 nm) pulse with 2.5 n-second width.

Keywords: Simulation; Diode Laser; Q-Switched Nd:YAG Laser; Eye-Safe Laser; Signal; Idler; IOPO; Rate Equations; Out-Put Power; KTP Non-Linear Crystal; Pump Beam Waist

1. Introduction

Compact nanosecond pulsed lasers operating in eye-safe wavelength region (1500 - 1600 nm) are of great interest in many applications such as laser radar, active imaging and remote sensing [1,2]. The conventional methods for the generation of eye-safe lasers are based upon solid-state lasers with Er^{3+} or Cr^{4+} doped media [3-6] and the Raman lasers pumped by Nd doped lasers [7-10]. Another promising approach for high-peak power eye-safe source is based upon optical parametric oscillator (OPO). The OPO has been extensively studied and developed ever since its demonstration in 1965. The main difference between Extra-cavity OPO (EOPO) and Intra-cavity OPO (IOPO) is that in IOPO, the OPO cavity is designed to be inside the cavity of the pump laser. The IOPO serves as a nonlinear cavity dumper to extract the energy stored in the intra-cavity optical field [11,12]. In recent years, KTP-IOPO pumped by passively Q-switched diode-pumped Nd-doped lasers has been investigated experimentally and high-energy pulses with mJ range energy have been obtained. The conversion efficiency of the optimized Q-switched pulse energy at 1047 nm (Nd:YLF) to 1547 nm signal approached by about 47% [13]. However, the signal pulse energy is restricted mainly due to initial transmission of saturable absorber. The first KTP-based IOPO driven by a diode-pumped electro-optical Q-switched Nd:YAG laser was realized by Jin Feng *et al.* 15 mJ energy output at 1.57 μm wavelength with 7 ns duration at 20 Hz was demonstrated [14]. The schematic is shown in **Figure 1** [15].

In this paper we simulate the diode-pumped Q-switched Nd:YAG laser generating eye-safe laser signal in IOPO environment. In the next section Diode-pumped Q-switched Nd:YAG laser is simulated.

2. Simulation of Diode-Pumped Q-Switched Pulsed Nd:YAG Laser

Taking into account the losses of pump into signal and idler radiation in the nonlinear crystal (KTP), the rate equations for the Q-switched Nd:YAG laser in IOPO [16] have been modified for diode-pumped regime and described as:

$$\frac{\mathrm{d}\phi_p}{\mathrm{d}t} = \phi_p \left[c\sigma N \frac{l_r}{L'} - \kappa_{\text{loss}} \right] \tag{1}$$

$$\frac{\mathrm{d}N}{\mathrm{d}t} = -\phi_p c\sigma N. \tag{2}$$

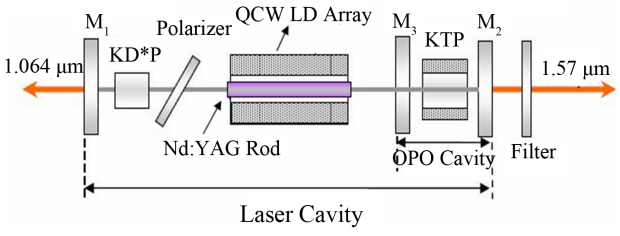

Figure 1. Schematic diagram of Intra-cavity optical parametric oscillator.

*Corresponding author.

Copyright © 2012 SciRes.

With

$$\kappa_{\text{loss}} = \left(\frac{\kappa_{\text{opo}}}{t_{\text{RL}}} + \frac{\kappa_{\text{cav}}}{t_{\text{RP}}} \right)$$

are the total losses inside the laser cavity and OPO cavity with

$$\kappa_{\text{cav}} = \ln\left(R_1 R_2 \left(1 - \frac{T_{\text{tot}}}{T_{\text{KTP}}} \right) \right) \text{ and } \kappa_{\text{opo}} = \left(1 - \eta_{\text{con}} \right).$$

Here, ϕ_p is the pump photon density, N is the population inversion, c is the speed of light, σ is the stimulated emission cross section of the laser medium. R_1 and R_2 represent the reflectivities of Nd:YAG cavity mirror.

Also, $T_{\text{tot}} = T_{\text{Nd:YAG}} + T_{\text{EOM}} + T_{\text{GP}} + T_{\text{KTP}}$, is the total transmission in the laser cavity. The Nd:YAG power/energy is converted into signal and idler power/energy through nonlinear interaction in KTP and represents the conversion efficiency of the Nd:YAG pump density into signal and idler. The scheme is such that idler signal is dumped inside the IOPO. Also, l_r is the length of the Nd:YAG rod and L' is the optical length of the laser cavity. The relation between the photon flux intensity I_m, the photon density ϕ_m, and the complex electric field $\tilde{E}$ (in the nonlinear crystal) is expressed as:

$$I_m = \frac{\phi_m h c \nu_m}{n_m} \tag{3}$$

$$I_m = \frac{1}{2} n_m c \varepsilon_0 \left| \tilde{E}_m \right|^2 \tag{4}$$

The reduction of above equations to photon density equation as:

$$\phi_m = \frac{1}{2} \frac{\varepsilon_0 n_m^2}{h \nu_m} \left| \tilde{E}_m \right|^2, \tag{5}$$

where h is the Plank's constant, ε_0 is the permittivity of free space, n_m is the refractive index at wavelength λ_m (m = p, s, i, corresponding to the secondary pump, signal and idler wavelengths), and $\omega_m = 2\pi\nu_m$ is the radiation frequency.

Equations (1) and (2) are temporal equations and have been numerically simulated. The results are given in **Figure 1**. The photon density forms a pulse with width of the order of few nanoseconds. The threshold population and energy are given as:

$$N_{th} = \frac{L'}{c \sigma l_r} \kappa_{\text{loss}} \tag{6}$$

$$E_{th} = \frac{N_{th} h c \pi L'}{\lambda_p} a^2. \tag{7}$$

The estimated values for N_{th} and E_{th} are 1.06×10^{17} cm^{-3} and 1.5 mJ respectively and more than [16] for lamp pumping. The main reason is that the Nd:YAG rod is transversally pumped by diode laser, which is more efficient than lamp pumping. The primary pumping pulse width is of the order of upper level's life time of Nd:YAG laser. It has been fixed at 200 μsec in the simulation. The dynamics of sudden decrease in population from its maximum initial value, N_i (2.06×10^{18} cm^{-3}), to the minimal value and emergence of Nd:YAG laser pulse simultaneously is represented in **Figure 2**.

In the next section, the simulated photon density of Nd:YAG laser will be transformed into secondary pump energy for eye-safe signal generation.

3. Eye-Safe Laser Pulse Generation in IOPO

It is convenient to define secondary pump photon energy (Nd:YAG) as

$$E_{np} = \frac{1}{2} \varepsilon_0 \left| E_p(t) \right|^2, \tag{8}$$

where $E_p(t)$ is the pump electric field as is described in Equation (5) and is related to photon density. The evolution of the pump, signal and idler fields during multiple round trips in the IOPO resonator has also been simulated. Nonlinear interaction in the KTP crystal, mirror losses including absorption losses in the crystal have been incorporated in the simulation. Assuming uniform plane waves interaction and perfect phase matching, we neglect the diffraction effects. The coupled equations for the parametric interaction along the x-crystallographic axis are:

$$\frac{\mathrm{d}E_p}{\mathrm{d}x} = -\alpha_p E_p - \frac{\omega_p \mathrm{d}_{\text{eff}}}{n_p c} E_s E_i \sin\theta \tag{9}$$

$$\frac{\mathrm{d}E_s}{\mathrm{d}x} = -\alpha_s E_s - \frac{\omega_s \mathrm{d}_{\text{eff}}}{n_s c} E_p E_i \sin\theta \tag{10}$$

$$\frac{\mathrm{d}E_i}{\mathrm{d}x} = -\alpha_i E_i - \frac{\omega_i \mathrm{d}_{\text{eff}}}{n_i c} E_s E_p \sin\theta \tag{11}$$

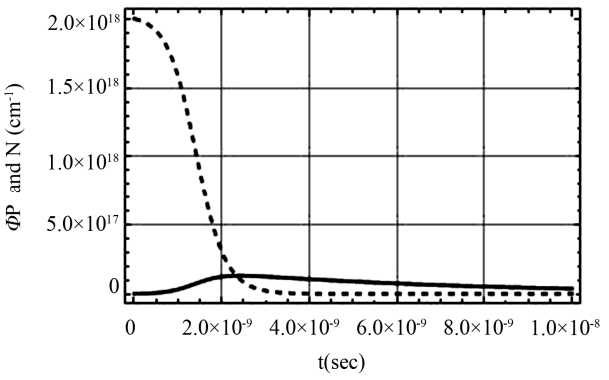

Figure 2. Nd:YAG laser photon density (in solid line) and population inversion (in dashed line) vs. time.

Copyright © 2012 SciRes.

$$\frac{\mathrm{d}\theta}{\mathrm{dx}} = \left(\frac{\omega_p E_s E_i}{E_p n_p} - \frac{\omega_s E_p E_i}{E_s n_s} - \frac{\omega_i E_s E_p}{E_i n_i} \right) \frac{\mathrm{d}_{eff}}{c} \cos\theta \quad (12)$$

It should be noted that all the fields in the Equations (9)-(12) are real. The initial phases of the signal and idler fields are not imposed by the interaction, so we suppose that they adjust themselves to maximize the energy transfer from the pump to signal and idler fields. For non-critical phase matching, $\theta = 90^{\circ}$, it means there is no angle tuning. In order to solve above coupled wave equations, we assume that pump field E_p remains constant in entire cavity length. Consequently, analytical solution of the above coupled wave equations for signal is given as:

$$E_s(x,t) = E_s(0,t) e^{-\alpha_s x} \cosh \Gamma(t) x. \quad (13)$$

where

$$\Gamma(t) = N_{\text{round}} \pi a_{\text{KTP}}^2 \sqrt{k_s k_i g_s} E_p(t) \quad (14)$$

is the parametric gain co-efficient in cm^{-1} is the parametric gain co-efficient in cm^{-1}. Here,

$$k_{i(s)} = \frac{2\pi \mathrm{d}_{\text{eff}}}{\lambda_{i(s)} n_{i(s)}},$$

is the response of the idler (signal) to the nonlinear crystal KTP and g_s is the signal spatial mode coupling co-efficient and is defined as:

$$g_s = \frac{w_p^2}{w_p^2 + w_s^2} \quad (15)$$

Here w_s and w_p are signal and pump beam waist, respectively. N_{round} is the number of round-trips for the gain, $N_{\text{round}} = \frac{1}{2} \frac{(1-R_2)}{(1+R_2)} \frac{A_c}{\pi w_s^2}$. It contains threshold gain similar to Equation (6) of [17]. It is worthwhile to mention here that w_p impacts the overlap between the pump and signal and determines the intra-cavity pump intensity. Furthermore, the steady state signal spot size w_s is also associated with w_p as follows [17]:

$$\left(\frac{\pi}{L' \lambda_s} \right)^2 w_s^6 + w_s^2 - \frac{w_p^2}{2} = 0 \quad (16)$$

with L' is the optical length of the IOPO cavity and given as $L' = \left(L + \left(n_p - 1 \right) l_{\text{KTP}} \right)$. We numerically solve Equation (16) for a fix pump beam waist value and find out that root of polynomial equation in w_s around that fix value of w_p. The signal develops after some round trips in IOPO cavity and a time-delay

$$t_d = \left(l_{\text{Nd:YAG}} + \left(n_p - 1 \right) T_{\text{Nd:YAG}} \right) / c,$$

and we assume that the signal electric field at the IOPO boundary is

$$E_s(0,t_d) = \pi a_{\text{KDP}}^2 l_{\text{KDP}} E_p(0,t_d). \quad (17)$$

Thus the expression for the signal energy is written as,

$$E_{ns}(L_{\text{iopo}},t) = \frac{1}{2} \varepsilon_0 \left| E_s(L_{\text{iopo}},t) \right|^2. \quad (18)$$

The constants/symbols along with values used in the simulation are provided in appendix. The parameters are either fixed or simulated. First, we simulate the primary pump source of the Nd:YAG laser and estimate the pumping rate. This pumping rate estimates initial population, N_i, used in initial conditions for the solution of the differential Equations (1) and (2). Numerical simulation is performed to investigate the population as well as the photon density of Nd:YAG pulsed laser. Another important simulated parameter is secondary pump beam quality as it determines the signal's beam quality. We fix the secondary pump beam waist and simulate the signal beam spot size and then follow the algorithm.

In the next section, the simulation results will be discussed briefly.

4. Results and Discussions

The results of Equations (8) and (18) are shown in **Figure 3**. It is quite evident that a 30 mJ Nd:YAG laser pulse with 5 n-second width generates a 9 mJ eye-safe signal pulse with 2.5 n-second width. The signal pulse emerges after a time delay commensurate with distance between mirrors M_1 and M_3.

The secondary pump beam waist is a vital design parameter. The slight change in its value will drastically affect its signal's counterpart as is evident in **Figure 4**. To prove this point, we increase its value from 500 μm to

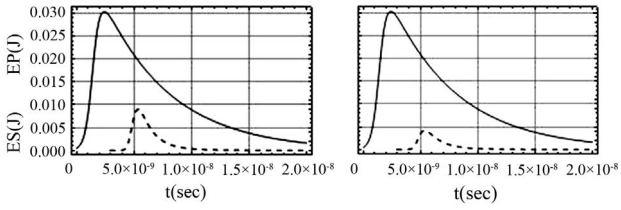

Figure 3. Secondary pump (solid) and signal energy (dashed) vs time for a) 0.05 cm (left) and b) 0.052 cm (right) pump beam waist.

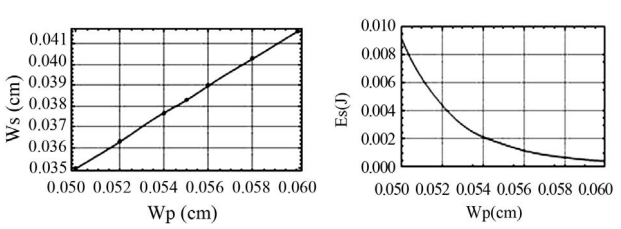

Figure 4. Variation of the signal spot size (left) and corresponding energy (right) with secondary pump beam waist.

Copyright © 2012 SciRes.

520 μm, the peak energy of the signal decreases from 9 to 4 mJ. This sensitivity of the signal spot size and corresponding peak energy with the secondary pump beam waist is highlighted and shown in **Figure 4**.

It is quite obvious from the above figure that the signal spot size has a linear relationship with pump beam waist and $\frac{w_s}{w_p} < 1$. It has been observed that the signal spatial mode coupling coefficient slightly increases with the pump beam waist but remains less than 0.68. However, the increase in secondary pump beam waist decreases the number of round trip for the gain. Consequently, the signal energy drops sharply and this trend goes on. Hence, there should be no compromise on pump beam quality. Finally, a comparison among the reference and simulated results are provided in **Table 1**.

5. Conclusion

Eye-safe laser has been simulated in IOPO environment in two steps. In first step, diode laser has been used as a primary pump source for the generation of 1064 nm Nd:YAG laser and in second step, Nd:YAG laser has been used as a secondary pump source for the generation of 1573 nm eye-safe laser signal. It has been shown that the eye-safe laser signal emerges after a time delay of the order of few n-seconds. The simulation results are in fairly good agreement with the referred work [15,16]. The pump beam waist is a vital design parameter. It describes the pump beam intensity. Here, it also dictates eye-safe signal pulse energy. The simulation gives reasonable results for diode laser energy less than 2 J as a primary pump source. For larger values, the secondary pump-to-signal energy ratio increases and one has to refix the parameters.

Table 1. A comparison of the simulated and referred results.

S. No.	Referred Results	Simulated Results
1	Diode pump λ = 808 nm [15-17]	Diode pump λ = 810 nm
2	Diode Peak Power: 15 KW [15]	Diode Peak Power: 14 KW
3	Nd:YAG λ = 1064 nm [15-17]	Nd:YAG λ = 1064 nm
4	Nd:YAG energy/pulse: 33 mJ (**Figure 2** of [16])	Nd:YAG energy/pulse: 30 mJ
5	Signal λ = 1570 nm [15,16]	Signal λ = 1573 nm
6	Signal Peak Power: 9.1 MW [15]	Signal Peak Power: 9.0 MW
7	Signal Pulse width: 3.48 n-sec [15]	Signal Pulse width 2.5 n-sec

6. Acknowledgements

The authors would like to thank Dr. Rehan Akhter and Dr. A. H. Hamadani for useful discussions.

REFERENCES

[1] E. Gregor, D. E. Niieuwsma and R. D. Stultz, "20 Hz Eyesafe Laser Rangefinder for Air Defense," *SPIE Proceedings*, Vol. 1207, 1990, pp. 124-134. doi:10.1117/12.17855

[2] E. Nettleton, B. W. Schilling, D. N. Barr and J. S. Lei, "Monoblock Laser for a Low-Cost, Eyesafe, Microlaser Range Finder," *Applied Optics*, Vol. 39, No. 15, 2000, pp. 2428-2432. doi:10.1364/AO.39.002428.

[3] S. Kuck, K. Petermann, U. Pohlmann, U. Schonhoff and G. Huber, "Tunable Room Temperature Laser Action of Cr^{4+}-doped $Y_3Sc_xAl_{5-x}O_{12}$," Vol. 58, No. 2, 1994, pp 153-156.

[4] N. V. Kuleshov, *et al.*, "Fluorescence Dynamics, Excited-State Absorption and Stimulated Emission of Er^{3+} in $KY(WO_4)_2$," *Optics InfoBase*: *Journal of the Optical Society of America B*, Vol. 15, No. 3, 1998, pp. 1205-1212. doi:10.1364/JOSAB.15.001205

[5] I. Sokolska, E. Heumann, S. Kuck and T. Lukasiewicz, "Laser Oscillation of Er^{3+}:YVO_4 and Er^{3+}, Yb^{3+}:YVO_4 Crystals in the Spectral Range around 1.6 μm," *Applied Physics B*, Vol. 71, No. 6, 2000, pp. 893-896.

[6] A. Sennaroglu, "Broadly Tunable Cr-Doped Solid-State Lasers in the near Infrared and Visible," *Progress in Quantum Electronics*, Vol. 26, No. 6, 2002, pp. 287-352. doi:10.1016/S0079-6727(02)00016-2

[7] P. Cerny, H. Jelinkova, P. G. Zverev and T. T. Basiev, "Solid State Lasers with Raman Frequency Conversion," *Progress in Quantum Electronics*, Vol. 28, No. 2, 2004, pp. 113-143. doi:10.1016/j.pquantelec.2003.09.003

[8] Y. F. Chen, "Compact Efficient All-Solid-State Eye-Safe Laser with Self-Frequency Raman Conversion in a Nd:YVO_4 Crystal," *Optics Letters*, Vol. 29, No. 18, 2004, pp. 2172-2174. doi:10.1364/OL.29.002172

[9] Y. F. Chen, "Efficient 1521-11 m Nd:$GdVO_4$ Raman Laser," *Optics Letters*, Vol. 29, No. 22, 2004, pp. 2632-2634. doi:10.1364/OL.29.002632

[10] J. T. Murray, R. C. Powell, N. Peyghambarian, D. Smith, W. Austin and R. A. Stolzenberger, "Generation of 1.5 μm Radiation through Intracavity Solid State Raman Shifting in $Ba(NO_3)_2$ Nonlinear Crystals," *Optics Letters*, Vol. 20, No. 9, 1995, pp. 1017-1023. doi:10.1364/OL.20.001017

[11] Y. Yashkir and H. M. Van Driel, "Passively Q-Switched 1.57-μm Intracavity Optical Parametric Oscillator," *Applied Optics*, Vol. 38, No. 12, 1999, pp. 2554-2559. doi:10.1364/AO.38.002554

[12] A. Agnesi, S. Dell'aequa and G. Reali, "Diode-Pumped Quasi-Cw Intracavity Optical Parametric Oscillator at 1.57 μm with Efficient Pulse Shortening," *Applied Physics B*: *Lasers and Optics*, Vol. 70, No. 6, 2000, pp. 751-753. doi:10.1007/PL00021130

Copyright © 2012 SciRes.

[13] W. Zendzian, J. K. Jabczynski, J. Kwiatkowski and K. Kopczynski, "300-kW, Eye-Safe Intracavity OPO Transmitter," *Proceedings of the SPIE*, Vol. 6952, 2008, Article ID: 69520U.

[14] F. Jin, G. Zhai, J. Li, N. Ma and S. S. Shi, "All Solid State Eye-Safe Optical Parametric Oscillators," *Laser Technology*, Vol. 26, No. 3, 2002, pp. 201-203.

[15] Y.-Y. Wang, K. Zhong and D.-G. Xu, "High-Energy Pulsed Eye-Safe Intracavity Optical Parametric Oscillator at 1.57 μm," *Proceedings of the SPIE*, Vol. 7276, 2008, Article ID: 727603.

[16] R. Dabu, A. Stratan and C. Fenic, "Intracavity Pumped Nanosecond Optical Parametric Oscillator Emitting in the Eye-Safe Range," *Applied Optics*, Vol. 40, No. 24, 2001, pp. 4334-4340.

[17] J. G. Miao, H. K. Bian and B. S. Wang, "Low Threshold Narrow Pulse Width Intra-Cavity Optical Parametric Oscillator at 1573 nm," *Optics Communications*, Vol. 265, No. 1, 2006, pp. 349-353. doi:10.1016/j.optcom.2006.03.040

Copyright © 2012 SciRes.

Appendix

Constants and Symbols

Diode pumping inputs.

η_r	Laser diode irradiative efficiency	50	[%]
η_t	Pump transfer efficiency	80	[%]
η_a	Absorption efficiency of the diode laser	90	[%]
η_{p1}	Primary pumping efficiency $\eta_{p1} = \eta_r \times \eta_t \times \eta_a$	36	[%]
P_p	Pumping peak power of diode laser	14	KW

Nd:YAG inputs.

R_1	Reflectivity of M_1 (Nd:YAG transmission)	99.7	[%]
R_2	Reflectivity of M_2 (Eye-safe transmission)	99.3	[%]
l	Nd:YAG Laser rod length	7.5	[cm]
$l_{\text{Nd:YAG}}$	Nd:YAG (only) laser cavity length	87.5	[cm]
$a_{\text{KD*P}}$	Diameter of electro-optical Q-switch (Pockels cell)	0.055	[cm]
$l_{\text{KD*P}}$	Length of electro-optical Q-switch (Pockels cell)	1.2	[cm]
a	Diameter of Nd:YAG rod in cm	0.05	[cm]
L	Optical length of the Nd:YAG cavity	91.122	[cm]
η_{lsr}	Laser efficiency	2.5	[%]
L	Laser cavity Length	90	[cm]
τ_1	Lower laser level life time	120×10^{-9}	[sec]
τ_2	Upper laser level life time	230×10^{-6}	[sec]

IOPO inputs

d_{eff}	Effective nonlinear coefficient	7×10^{-10}	[cm/V]
a_{ktp}	Diameter of KTP crystal	0.04	[cm]
l_{ktp}	KTP crystal length	1.5	[cm]
l_{iopo}	Length of IOPO (only)	2.5	[cm]
η_{con}	Conversion efficiency of secondary pump into signal	0.90	[%]
τ_{RL}	Round trip time in IOPO resonator	6.05×10^{-9}	[sec]
τ_{RP}	Round trip time in IOPO cavity, $\tau_{\text{RP}} = (2\,(l_{\text{iopo}} + (\text{ns} - 1)\,l_{\text{ktp}}))/\text{c}$	0.21×10^{-9}	[sec]
Ac	Area of the out-put coupler M_1 & M_2	0.5	[cm^2]
n_p	Refractive index at secondary pump wavelength	1.748	-
n_s	Refractive index at signal wavelength	1.5	-
n_i	Refractive index at idler wavelength	1.5	-
T_{EOM}	Transmission of electro-optical modulator	96	[%]
$T_{\text{Nd:YAG}}$	Transmission of Nd:YAG	96	[%]
T_{GP}	Transmission of polarizer	86	[%]
T_{KTP}	Transmission of KTP crystal	98	[%]
R_3	Reflectivity of M_3 for eye-safe signal	100	[%]
λ_i	Idler wavelength	3.3×10^{-4}	[cm]
α_i	Attenuation coefficient of idler in KTP	0.4	[cm^{-1}]
α_s	Attenuation coefficient of signal in KTP	0.007	[cm^{-1}]

Copyright © 2012 SciRes.

Optics and Photonics Journal, **2012, 2, 173-177**
doi:10.4236/opj.2012.23026 Published Online September 2012 (http://www.SciRP.org/journal/opj)

Schrödinger Equation with a Cubic Nonlinearity Sech-Shaped Soliton Solutions

Pierre Hillion
Institut Henri Poincaré, Le Vésinet, France
Email: pierre.hillion@wanadoo.fr

Received June 3, 2012; revised July 1, 2012; accepted July 12, 2012

ABSTRACT

We first analyze the sech-shaped soliton solutions, either spatial or temporal of the 1D-Schrödinger equation with a cubic nonlinearity. Afterwards, these solutions are generalized to the 2D-Schrödinger equation in the same configuration and new soliton solutions are obtained. It is shown that working with dimensionless equations makes easy this generalization. The impact of solitons on modern technology is then stressed.

Keywords: Soliton; Schrödinger Equation; Cubic Nonlinearity

1. Introduction

The one dimensional Schrödinger equation with a cubic nonlinearity has been known for a long time as well as its analytical solutions in terms of sech-shaped functions.Till recently, the situation was different for the two dimensional Schrödinger equation that we shall discuss here.

Using general equations, we start with the spatial and temporal sech-shaped soliton solutions of the 1D-Schrödinger equation with a cubic nonlinearity and it is shown that working with dimensionless equations leads to further types of solitons. Then, the same process with gene-ral and dimensionless equations is applied to the 2D-nonlinear Schrödinger equation which has sech-shaped soliton solutions generalizing 1D-solitons. Finally, because the nonlinear Schrödinger equation is a universal model that describes many physical non linear systems, the importance of solitons in modern technology is stressed. Nonlinear Schrödinger equations in (3D) and in cylindrical coordinates are succinctly discussed in Section 4.

2. One Dimensional Sech-Shaped Solitons

2.1. General Equations

The one-dimensional, cubic, nonlinear Schrödinger Equation [1] intervenes in different physical settings to describe wave propagation in fluids, plasmas… nonlinear optics [2-6] in one of the three forms (c is the light velocity, k the wave number of propagating waves, χ is a positive dimensionless parameter characterizing the medium in which this propagation takes place).

$$i\partial_z\psi(x,z)-1/2k\,\partial_x{}^2\psi(x,z)-k\chi|\psi|^2\psi(x,z)=0 \quad (1a)$$

$$i\partial_z\psi(t,z)+\beta\partial_t^2\psi(t,z)+k\chi|\psi|^2\psi(t,z)=0 \quad \beta>0 \quad (1b)$$

$$i/c\,\partial_t\psi(x,t)+1/2k\,\partial_x^2\psi(x,t)+k\chi|\psi|^2\psi(x,t)=0 \quad (1c)$$

It is known to be one of the simplest partial differential equations with complete integrability, admetting in particular Nth order solitons as solutions and called spatial and temporal when they are solutions of (1a) or (1b). Changing the sign of the last term on the left hand side of Equations (1a)-(1c) gives a second set of cubic nonlinear Schrödinger equations with quasi periodic but no soliton sech-shaped solutions.

It is easy to prove that the first order soliton solution of Equation (1a) with amplitude A is [6]

$$\psi(x,z)-A\exp(-i\lambda z)\operatorname{sech}(x/x_0) \quad (2)$$

with

$$\lambda=k\chi A^2/2,\ 1/x_0=kA\sqrt{\chi} \quad (2a)$$

Indeed:

$$\begin{aligned} &i\partial_z\psi(x,z)-k\chi|\psi|^2\psi(x,z)\\ &=k\chi A^2/2\left[1-2\operatorname{sech}^2(x/x_0)\right]\psi(x,z)\end{aligned} \quad (3a)$$

while

$$\begin{aligned} &-1/2k\,\partial_x^2\psi(x,z)\\ &=-1/2k\,x_0{}^2\left[1-2\operatorname{sech}^2(x/x_0)\right]\psi(x,z)\end{aligned} \quad (3b)$$

$$=-k\chi A^2/2\left[1-2\operatorname{sech}^2(x/x_0)\right]\psi(x,z) \quad (3c)$$

Substituting (3a) and (3c) into (1a) proves the result and, changing z, k into ct, $-k$ in (2) gives the first order

Copyright © 2012 SciRes.

soliton solution of Equation (1c) while the solution of (1b) is [6] easy to check

$$\psi(t,z) = 1/t_0 \sqrt{\beta/\chi}\exp\left(i\beta z/2t_0^2\right)\operatorname{sech}\left(t/t_0\right) \quad (4)$$

These solutions have the remarkable feature that their profile does not evolve during propagation.

2.2. Dimensionless Equations

Using the dimensionless coordinates $\zeta = kz$, $\xi = \sqrt{2kx}$, $\tau = kct$ the Equations (1a) and (1c) take the simple form (5a) and (5c)

$$i\partial_\zeta\psi - \partial_\xi^2\psi - \chi|\psi|^2\psi = 0 \quad (5a)$$

$$i\partial_z\phi + \partial_t^2\phi + \chi|\phi|^2\phi = 0 \quad (5b)$$

$$i/\partial_\tau\psi + \partial_\xi^2\psi + \chi|\psi|^2\psi = 0 \quad (5c)$$

while the Equation (5b) is obtained with [7] $\zeta = z/z_0$, $\tau = t/t_0$, $t_0^2 = \beta z_0$, $\psi = \phi/\sqrt{z_0}$.

But, there exist more general expressions of the first order solitons for instance, for the Equation (5c) rewritten with the coordinates x, z, t, we have

$$\psi(x,t) = \pm A/2\chi\exp\left[iBx + i\left(A^2 - B^2\right)t + C_1\right] \times\operatorname{sech}\left[Ax - 2Abt + C_2\right] \quad (6)$$

in which A, B, C_1, C_2 are arbitrary real constant with in particular [7]

$$\psi(x,t) = \left(2\alpha/\chi\right)^{1/2}\exp\left[ivx/2 - i\left(v^2/4 - \alpha\right)t\right] \times\operatorname{sech}\left[\alpha^{1/2}\left(x - vt\right)\right] \quad (6a)$$

Similarly, with Equation (5a) also rewritten with x, z, we get as solution in which β is a dimension-less parameter

$$\psi(x,z) = \left(2\alpha/\chi\right)^{1/2}\exp\left[i\beta x/2 + i\left(\beta^2/4 - \alpha\right)z\right] \times\operatorname{sech}\left[\alpha^{1/2}\left(x + \beta z\right)\right] \quad (7)$$

The higher order soliton solutions have more intricate expressions [8] and their profile is no more constant, the solutions being rather periodic than stationary. The profile of a $N = 2$ soliton is pictured in [3].

The Equation (5b) has the simple solution [6]

$$\phi(\zeta,\tau) = \sqrt{(2q)}\exp(iq\zeta)\operatorname{sech}\left[\sqrt{(2q)}\tau\right]\ q > 0,$$

but, the comparison of (5b) and (5c) shows that changing x, t, ψ into τ, ζ, ϕ in (6a) gives another solution of (5b)

$$\phi(\tau,\zeta) = \left(2\alpha/\chi\right)^{1/2}\exp\left[i\eta\tau/2 - i\left(\eta^2/4 - \alpha\right)\zeta\right] \times\operatorname{sech}\left[\alpha^{1/2}\left(t - \eta\zeta\right)\right] \quad (8)$$

where to avoid confusion η has ben used instead of v.

3. Two Dimensional Sech-Shaped Solitons

3.1. General Equations

The situation is somewhat different for the two dimensional cubic nonlinear Schrödinger equations (cylindrical coordinates are used in (9b))

$$\begin{aligned} &i\partial_z\psi(x,y;z) \\ &-1/2k\left[\partial_x^2\psi(x,y;z) + \partial_y^2\psi(x,y;z)\right] \\ &-k\chi|\psi|^2\psi(x,y;z) = 0 \end{aligned} \quad (9a)$$

$$\begin{aligned} &i\left[\partial_r + 1/r\partial_\theta\right]\psi(r,\theta;t) \\ &+\beta\partial_t^2\psi(r,\theta;t) + \chi|\psi|^2\psi(r,\theta;t) = 0 \end{aligned} \quad (9b)$$

$$\begin{aligned} &i/c\,\partial_t\psi(x,y;t) \\ &+1/2k\left[\partial_x^2\psi(x,y;t) + \partial_y^2\psi(x,y;t)\right] \\ &+k\chi|\psi|^2\psi(x,y;t) = 0 \end{aligned} \quad (9c)$$

They where devoted to some domains, mainly hydrodynamics and mechanics [9-11] till that recently nonlinearities became an important topic, specially in optics and photonics, with as consequence to boost works on the analysis of Equations (9).

We prove here that Equation (9a) have soliton-shaped solutions generalizing (2)

$$\psi(x,y;z) = A\exp(i\lambda z)\operatorname{sech}\left(x/x_0 + y/y_0\right) \quad (10)$$

with

$$\lambda = k\chi A^2/2,\quad 1/x_0^2 + i/y_0^2 = k^2A^2\chi \quad (10a)$$

We first have

$$\begin{aligned} &i\partial_z\psi(x,y;z) - k\chi|\psi|^2\psi(x,y;z) \\ &= k\chi A^2/2\left[1 - 2\operatorname{sech}^2\left(x/x_0 + y/y_0\right)\right]\psi(x,y;z) \end{aligned} \quad (11a)$$

and according to (3b) together with the second relation (10a)

$$\begin{aligned} &1/2k\left[\partial_x^2\psi(x,y;z) + \partial_y^2\psi(x,y;z)\right] \\ &= -1/2k\left(1/x_0^2 + 1/y_0^2\right)\left[1 - 2\operatorname{sech}^2\left(x/x_0 + y/y_0\right)\right] \\ &\times\psi(x,y;z) \end{aligned} \quad (11b)$$

$$= -k\chi A^2/2\left[1 - 2\operatorname{sech}^2\left(x/x_0 + y/y_0\right)\right]\psi(x,y;z) \quad (11c)$$

Substituting (11a) and (11c) into (9a) achieves the proof. Changing z, k into ct, $-k$ in (10) gives the soliton-shaped solution $\psi(x,y;t)$ of Equation (9c).

3.2. Dimensionless Equations

The two dimensional generalization of Equation (5c), that is (9c) with dimensionless coordinates, is

Copyright © 2012 SciRes.

$$i\partial_t\psi(x,y;t) + \left(\partial_x^2+\partial_y^2\right)\psi(x,y;t)+\chi|\psi|^2\psi(x,y;t)=0 \quad (12)$$

We look for the solutions of this equation in the form

$$\psi(x,y;t)=\exp\left[iv_x x/2+iv_y y/2-i\left(v^2/4-\alpha\right)t\right] \times\phi\left[r\left(x-v_x t\right)+s\left(y-v_y t\right)\right] \quad (13)$$

in which $v^2=v_x^2+v_y^2$ while α, r, s are real parameters and, to symplify we write exp(.) the exponential factor. Then, a simple calculation gives

$$\begin{aligned} i\partial_t\psi &= \left(v^2/4-\alpha\right)\psi+\exp(.)i\partial_t\phi \\ \partial_x^2\psi &= -v_x^2/4\psi+\exp(.)\left[iv_x\partial_x\phi+\partial_x^2\phi\right] \\ \partial_y^2\psi &= -v_y^2/4\psi+\exp(.)\left[iv_y\partial_y\phi+\partial_y^2\phi\right] \end{aligned} \quad (14)$$

Substituting (13) into (12) gives the equation satisfied by ϕ with $\left(i\partial_t+iv_x\partial_x+iv_y\partial_y\right)\phi=0$

$$\left(\partial_x^2+\partial_y^2\right)\phi-\alpha\phi+\chi\phi^3=0 \quad (15)$$

and we look for the solutions of (15) in the form

$$\phi(x,y;t)=\lambda\,\mathrm{sech}\left[r\left(x-v_x t\right)+s\left(y-v_y t\right)\right] \quad (16)$$

in which λ, r, s are real parameters to be determined. Writing to simplify $\phi=\lambda/\cosh(.)$, we get

$$-\alpha\phi+\chi\phi^3=-\alpha\lambda/\cosh(.)\left[1-\chi\lambda^2/\alpha\cosh^2(.)\right] \quad (17)$$

and

$$\begin{aligned} \partial_x\phi &= -\lambda r\,\sinh(.)/\cosh^2(.) \\ \partial_x^2\phi &= \lambda r^2/\cosh(.)\left[1-2/\cosh^2(.)\right] \end{aligned} \quad (18a)$$

$$\partial_y^2\phi=\lambda s^2/\cosh(.)\left[1-2/\cosh^2(.)\right] \quad (18b)$$

substituting (17) and (18a,b) into (15) gives

$$-\alpha\lambda/\cosh(.)\left[1-\chi\lambda^2/\alpha\cosh^2(.)\right] +\lambda\left(r^2+s^2\right)/\cosh(.)\left[1-2/\cosh^2(.)\right]=0 \quad (19)$$

implying

$$\alpha=r^2+s^2,\quad \lambda^2=2\alpha/\chi \quad (19a)$$

so that the solution (16) becomes with $\alpha_r+\alpha_s=\alpha$

$$\phi(x,y;t)=\left(2\alpha/\chi\right)^{1/2}\mathrm{sech}\left[\sqrt{a_r\left(x-v_x t\right)}+\sqrt{a_s\left(y-v_y t\right)}\right] \quad (20)$$

to be compared with (6a).

Similarly the two dimensional generalization of (5a), that is (9a) with dimensionless coordinates, is

$$i\partial_z\psi(x,y;z)-\left[\partial_x^2\psi(x,y;z)+\partial_y^2\psi(x,y;z)\right] -\chi|\psi|^2\psi(x,y;z)=0 \quad (21)$$

with the solutions in which $\beta^2=\beta_1^2+\beta_2^2$ and $\beta_1+\beta_2=\alpha$

$$\psi(x,y;z) =\left(2\alpha/\chi\right)^{1/2}\exp\left[i\beta_1 x/2+i\beta_2 y/2+i\left(\beta^2/4-\alpha\right)z\right] \times\mathrm{sech}\left[\sqrt{\beta_1\left(x+\beta_1 z\right)}+\sqrt{\beta_2\left(y+\beta_2 z\right)}\right] \quad (22)$$

We are left with Equation (9b). Then, using the dimensionless coordinates $r=r_0\rho$, $t=t_0\tau$, $t_0^2=\beta r_0$, $\psi=\phi/\sqrt{r_0}$ in which ρ and r_0 positive. we get

$$i\left[\partial_\rho+1/\rho\partial_\theta\right]\phi(\rho,\theta;\tau) +\partial_\tau^2\phi(\rho,\theta;\tau)+\chi|\phi|^2\phi(\rho,\theta,\tau)=0 \quad (23)$$

We look for the solution of this equation in the form

$$\phi(\rho,\theta;\tau)=\exp\left[-i\theta-if(\rho)\right]\varpi(\tau) \quad (24)$$

with $f(\rho)$ satisfying the equation

$$\left[\left(\partial_\rho+1/\rho\right)f\right]=-k\quad k>0 \quad (24a)$$

Substituting (24) into (23) and taking into account (24a) give

$$\partial_\tau^2\varpi(\tau)-k\varpi(\tau)+\chi\varpi^3(\tau)=0 \quad (25)$$

with the solution [7]

$$\varpi(\tau)=\left(2k/\chi\right)^{1/2}\mathrm{sech}\left[\sqrt{k}\left(\rho-v\tau\right)\right] \quad (25a)$$

while the solution of (24a) is

$$f(\rho)=-k(\rho)/2 \quad (26)$$

substituting (25a) and (26) into (24) we get finally

$$\phi(\rho,\theta;\tau)=\left(2k/\chi\right)^{1/2}\exp\left[-i\theta+(i\,k\rho)/2\right] \times\mathrm{sech}\left[\sqrt{k}\left(\rho-v\tau\right)\right] \quad (27)$$

in which v is an arbitrary real parameter. It does not seem that the sech-shaped soliton (27) is known. But, substituting the dimensionless coordinate $\zeta=z/z_0$ to τ into (27) gives the sech-shaped pulse

$$\phi(\rho,\theta;\zeta)=\left(2k/\chi\right)^{1/2}\exp\left[-i\theta-i\exp(-k\rho)/\rho\right] \times\mathrm{sech}\left[\sqrt{k}\left(\rho-v\zeta\right)\right] \quad (28)$$

4. Two Generalizations

4.1. 3D-Schrödinger Equation

Using the index $j=1,2,3$ for the dimensionless coordinates x,y,z together with the sum-mation convention on the repeated indices and $\mathbf{x}=(x,y,z)$, the tridimensional cubic nonlinear Schrödinger equation is

$$i\partial_t\psi(\mathbf{x},t)+\partial^j\partial_j\psi(\mathbf{x},t)+\chi|\psi|^2\psi(\mathbf{x},t)=0 \quad (29)$$

Copyright © 2012 SciRes.

We look for the solution of this equation in the form $v^j v_j = v^2$

$$\left(\psi(\mathbf{x},t) = \exp\left[iv^j x_j/2 - i\left(v^2-\alpha\right)t\right]\phi\left(\beta^j x_j - v_j t\right)\right) \quad (30)$$

the exponential term is written exp(.) to simplify and a simple calculation gives

$$\begin{aligned} i\partial_t\psi &= \left(v^2/4-\alpha\right)\psi + \exp(.)i\partial_t\phi \\ \partial^j\partial_j\psi &= -v^2/4\psi + \exp(.)\left[iv^j\partial_j\phi + \partial^j\partial_j\phi\right] \end{aligned} \quad (31)$$

Since $\left(\partial_t + v^j\partial_j\right)\phi = 0$, substituting (31) into (30) gives the equation satisfied by ϕ

$$\partial^j\partial_j\phi - \alpha\phi + \chi\phi^3 = 0 \quad (32)$$

We look for its solutions in the form with the real parameters λ, β^j to be determined

$$\phi = \lambda\,\mathrm{sech}\left[\beta^j\left(x_j - v_j t\right)\right] \quad (33)$$

and writing 1/cosh(.) for $\mathrm{sech}\left[\beta^j\left(x_j - v_j t\right)\right]$, we get

$$-\alpha\phi + \chi\phi^3 = -\alpha\lambda/\cosh(.)\left[1 - \chi\lambda^2/\alpha\cosh^2(.)\right] \quad (34a)$$

and $\partial_j\phi = -\lambda\beta^j\sinh(.)/\cosh^2(.)$ implying

$$\partial^j\partial_j\phi = \lambda\beta^2/\cosh(.)\left[1 - 2/\cosh^2(.)\right] \quad (34b)$$

Substituting (34) into (32) gives

$$\begin{aligned} &-\alpha\lambda/\cosh(.)\left[1-\chi\lambda^2/\alpha\cosh^2(.)\right] \\ &+\lambda\beta^2/\cosh(.)\left[1-2/\cosh^2(.)\right] = 0 \end{aligned} \quad (35)$$

implying

$$\alpha = \beta^2, \quad \lambda^2 = 2\alpha/\chi \quad (36)$$

which achieves to determine (33) and consequently the solution (30) of the three dimensional cubic nonlinear Schrödinger equation

4.2. Schrödinger Equation in Cylindrical Coordinates

Using the dimensionless coordinates r, θ, ϕ, the Schrödinger equation with a cubic non linelarity is

$$\left\{\psi \equiv \psi(r,\theta,\phi;t)\right\}$$

$$i\partial_t\psi + \Delta\psi + \chi|\psi|^2\psi = 0 \quad (37)$$

$$\Delta = \partial_r^2 + 2/r\partial_r + 1/r\sin\theta\partial_\theta\left(\sin\theta\partial_\theta\right) + 1/r^2\sin^2\theta\partial_\phi^2 \quad (37a)$$

For fields that do not depend on θ, ϕ, this equation reduces to

$$i\partial_t\psi(r,t) + \left(\partial_r^2 + 2/r\partial_r\right)\psi(r,t) + \chi|\psi|^2\psi(r,t) = 0 \quad (38)$$

and assuming $\psi(r,t) = 1/r\phi(r,t)$, we get

$$\partial_r\psi = 1/r\partial_r\phi - 1/r^2\phi, \partial_r^2\psi = 1/r\partial_r^2\phi - 2/r\partial_r^2\phi + 2/r^3\phi \quad (39)$$

so that

$$\left(\partial_r^2 + 2/r\partial_r\right)\psi = 1/r\partial_r^2\phi \quad (40)$$

and Equation (38) becomes

$$i\partial_t\phi + \partial_r^2\phi + \chi/r^2|\phi|^2\phi = 0 \quad (41)$$

We look for the solutions of this equation in the form

$$\phi(r,t) = \exp\left[ivr/2 - i\left(v^2/4-\alpha\right)t\right]\varpi(r-vt) \quad (42)$$

and a simple calculation gives, exp(.) representing the exponential term.

$$\begin{aligned} i\partial_t\phi &= \left(v^2/4-\alpha\right)\phi + \exp(.)i\partial_t\varpi \\ \partial_r\phi &= iv/2\phi + \exp(.)\partial_r\phi \\ \partial_r^2\phi &= -v^2/4\phi + \exp(.)\left(iv\partial_r\varpi + \partial_r^2\varpi\right) \end{aligned} \quad (43)$$

Substituting (42) into (41) and taking into account (43), we get since $\left(\partial_t + v\partial_r\right)\varpi = 0$

$$\partial_r^2\varpi - \alpha\varpi + \chi/r^2\varpi^3 = 0 \quad (44)$$

We look for the solutions of this equation in the form with the real parameters β, λ to be de-termined

$$\varpi = \lambda/\cosh\left[\beta(r-vt)\right] \quad (45)$$

Writing $\cosh(.)$, $\sinh(.)$ for hyperbolic functions, a simple calculation gives

$$\begin{aligned} \partial_r\varpi &= -\lambda\beta\sinh(.)/\cosh^2(.), \\ \partial_r^2\varpi &= -\lambda\beta^2\left[1/\cosh(.) - 2\sinh^2(.)/\cosh^3(.)\right] \end{aligned} \quad (46)$$

Substituting (45) and (46) into (44) gives

$$\begin{aligned} &\lambda\beta^2\left[1/\cosh(.) - 2/\cosh^3(.)\right] \\ &-\lambda\alpha/\cosh(.) + \chi\lambda^3/r^2\cosh^2(.) = 0 \end{aligned} \quad (47)$$

that is

$$\beta^2/\alpha\left[1-2/\cosh^3(.)\right] - 1 + \chi\lambda^2/\alpha r^2\cosh^2(.) = 0 \quad (48)$$

We consider an asymptotic approximation of this equation for $r \gg r_0$ with $r = r_0 + \rho$ so that to the order $0(2\rho/r_0)$ Equation (48) becomes

$$\beta^2/\alpha\left[1-2/\cosh^3(.)\right] - 1 + \chi\lambda^2/\alpha r_0^2\cosh^2(.) = 0 \quad (48a)$$

with the solution $\beta^2 = \alpha$, $\lambda = r_0\sqrt{2\alpha}/\chi + 0(2\rho/r_0)$ which achieves to determine the spherical solution of the cubic nonlinear Schrödinger equation.

5. Conclusions

The nonlinear Schrödinger equation describes physical processes in which nonlinearity and dispersion cancel giving birth to solitons. This equation [9-11] can be applied to hydrodynamics (rogue waves), nonlinear optics (optical solitons in Kerr media), nonlinear aoustics (blood circu-

Copyright © 2012 SciRes.

lation), quantum condensates (Bose-Einstein), heath waves… All these processes lead to the generation of solitons along pulse propagation: An example is supplied by the optical solitons that travel without distortion justifying their importance [12-15] for laser pulse propagation in optical fibers.

Two dimensional solitons present a great interest since they propagate in lattices [16,17] as well as surface waves [18-21]. Some works were recently devoted to the 2D-optical solitons [22,23] and the sech-shaped solutions (20), (21) of Equations (9a) and (9c) are a particular case of the spatial temporal solutions discussed in [23].

No doubt that some of the 2D sech-shaped solitons discussed here will find practical applications in a near future.

REFERENCES

[1] T. Oh and C. Sulem, "On One Dimensional Cubic Nonlinear Schrödinger Equation," arXiv: 10072018, 2010.

[2] N. N. Akhmediev, "Spatial Solitons in Kerr and Kerr-Like Media," *Optical and Quantum Electronics*, Vol. 30, No. 7-10, 1998, pp. 535-569. doi:10.1023/A:1006902715737

[3] J. G. New, "Introduction to Nonlinear Optics," Cambridge University Press, Cambridge, 2011. doi:10.1017/CBO9780511975851

[4] G. Gryndberg, A. Aspect and Cl. Fabre, "Introduction to Quantum Optics," Cambridge University Press, Cambridge, 2010.

[5] C. Q. Dai, Z. Q. Qin and C. L. Zheng, "Multisoliton Solutions of the Modified Nonlinear Schrö-Dinger Equation," *Physica Scripta*, Vol. 85, No. 4, 2012, Article ID: 045007. doi:10.1088/0031-8949/85/04/045007

[6] C. J. Brenton, "Solitons and Nonlinear Optics in Silicon-On Insulator Photonics Wires," Thesis, 2009.

[7] G. B. Whitham, "Linear and Nonlinear Wave Equations," Wiley, New York, 1974.

[8] Eq. World (Google), "Shrödinger Equation with a Cubic Nonlinearity,"

[9] J. Bourgain, "Nonlinear Schrödinger Equation," Parc City Lectures, 1995.

[10] R. Killip, T. Tao and M. Visam, "The Cubic Nonlinear Schrödinger Equation in Two Dimen-Sions with Radial Data," *Journal of the European Mathematical Society*, Vol. 11, No. 6, 2009, pp. 1203-1258. doi:10.4171/JEMS/180

[11] A. R. Seadway, "Exact Solutions of a Two Dimensional Nonlinear Schrödinger Equation," *Applied Mathematics Letters*, Vol. 25, 2012, pp. 687-691.

[12] J. C. Bronski, M. Segev and M. Weinstein, "Mathematical Frontiers in Optical Solitons," *Proceedings of the National Academy of Sciences*, Vol. 98, No. 23, 2001, pp. 12872-12873.

[13] Z. H. Muslinami, K. G. Makris, R. EL-Ganaini and D. N. Christodoulides, "Optical Solitons in PT Periodic Potentials," *Physical Review Letters*, Vol. 100, 2006, Article ID: 030402.

[14] Y. V. Kartshov, "Optical Lattice Solitons: Guiding and Routing Light at Will," *OSA Optics and Photonics Focus*, 2009.

[15] F. I. Khatri, "Optical Soliton Propagation and Control," MIT Thesis, Massachusetts Institute of Technology, Cambridge, 1996.

[16] Y. V. Kartshov, J. A. Malomed, V. A. Vysloukh and L. Torner, "Two Dimensional Solitons in Nonlinear Lattices," *Optics Letters*, Vol. 34, No. 6, 2009, pp. 770-777. doi:10.1364/OL.34.000770

[17] M. J. Ablowitz, B. Ilan, E. Schonbrun and R. Piestun, "Two Dimensional Solitons in Irregular Lattices," *Theoretical and Mathematical Physics*, Vol. 151, No. 3, 2007, pp. 723-734. doi:10.1007/s11232-007-0058-4

[18] G. Maugin, "Nonlinear Surface Wave and Solitons," *The European Physical Journal*, Vol. 147, No. 1, 2007, pp. 209-230.

[19] X. Wang, A. Bezryadina, Z. ChenK, G. Magris, D. N. Christodoulides and G. I. Stegman, "Observation of a Two Dimensional Surface Soliton," *Physical Review*, Vol. 98, 2007, Article ID: 123903.

[20] Y. Kominis, A. Papadopoulos and K. Hizanidis, "Surface Solitons in Wave Guide Arrays; Analytical Solutions," *Optics Express*, Vol. 15, No. 16, 2007, pp. 10041-10051. doi:10.1364/OE.15.010041

[21] Y. V. Kartshov, V. A. Vysloukh and L. Torner, "Generation of Surface Soliton Arrays," *Optics Letters*, Vol. 31, No. 15, 2006, pp. 2329-2331. doi:10.1364/OL.31.002329

[22] N. K. Efremides, J. Hudlock, D. N. Christodoulides, J. W. Fleischer, D. Cohen and M. Segev, "Two Dimensional Optical Lattice Solitons," *Physical Review Letters*, Vol. 91, No. 21, 2003, pp. 1-4.

[23] B. A. Malomed, D. Mialache, F. Wise and L. Torner, "Spatial Temporel Solitons," *Journal of Optics B*: *Quantum and Semiclassical Optics*, Vol. 7, No. 5, 2005, pp. R53-R72. doi:10.1088/1464-4266/7/5/R02

Copyright © 2012 SciRes.

Optics and Photonics Journal, **2012, 2, 178-184**
doi:10.4236/opj.2012.23027 Published Online September 2012 (http://www.SciRP.org/journal/opj)

Break up of *N*-Soliton Bound State in a Gradient Refractive Index Waveguide with Nonlocal Nonlinearity

Isnani Darti[1,2], Suhariningsih[3], Marjono[1], Agus Suryanto[1]
[1]Department of Mathematics, Faculty of Sciences, Brawijaya University, Malang, Indonesia
[2]Mathematics and Natural Sciences PhD Program, Airlangga University, Surabaya, Indonesia
[3]Department of Physics, Faculty of Sciences and Technology, Airlangga University, Surabaya, Indonesia
Email: isnanidarti@ub.ac.id

Received June 28, 2012; revised July 31, 2012; accepted August 10, 2012

ABSTRACT

We study the propagation of *N*-soliton bound state in a triangular gradient refractive index waveguide with nonlocal nonlinearity. The study is based on the direct numerical solutions of the model and subsequent eigenvalues evolution of the corresponding Zakharov-Shabat spectral problem. In the waveguide with local nonlinearity, the velocity of a single soliton is found to be symmetric around zero and therefore the soliton oscillates periodically inside the waveguide. If the nonlocality is presence in the medium, the periodic motion of soliton is destroyed due to the soliton experiences additional positive acceleration induced by the nonlocality. In the waveguide with the same strength of nonlocality, a higher amplitude soliton experiences higher nonlocality effects, *i.e.* larger acceleration. Based on this soliton behavior we predict the break up of *N*-soliton bound state into their single-soliton constituents. We notice that the splitting process does not affect the amplitude of each soliton component.

Keywords: *N*-Soliton Bound State; GRIN Waveguide; Nonlocal Nonlinearity; Conserved Implicit Crank-Nicolson Method; Inverse Scattering Technique

1. Introduction

The propagation of optical beam in a homogenous Kerr medium is described by the nonlinear Schrodinger (NLS) equation which has a soliton solution. Spatial solitons are self-trapped light beams in which the diffraction is balanced by the self-focusing induced by nonlinearity. In a homogeneous Kerr medium with local nonlinearity, a single soliton propagates with a constant velocity. The velocity of soliton is disturbed as it propagates in an inhomogeneous refractive index medium, *i.e.*, a medium with a transverse gradient refractive index (GRIN) distribution, see e.g. [1,2]. If the nonlinear response of medium is nonlocal then it may significantly affect the properties of soliton [3]. For example, a uniform medium with positive nonlocal nonlinearity may induce a self-bending soliton [4-6]. It has been shown that a nonlocality increases the soliton acceleration. In a medium with the same strength of nonlocality, a higher amplitude soliton experiences much larger nonlocality effects than the lower one and therefore a soliton with higher amplitude will propagate with larger acceleration than that with lower amplitude, see e.g. [7,8].

It is known that the NLS equation has *N*-soliton bound state solution. Such a bound state contains *N* single solitons which have different amplitudes but they travel together with the same speed. During the propagation *N*-soliton bound state undergoes periodic oscillations in shape with individual solitons remaining localized. It is noticed that *N*-soliton bound state has no binding energy and therefore under suitable perturbations the *N*-soliton bound state can break up into their soliton constituents [9]. The break up of spatial *N*-soliton bound state can be induced e.g. by reflection at material interface [10], refractive index variation [11,12], interaction with periodic lattice [13,14], combination of two- and three-photon absorption [15], linear loss [16], and defect layer [17]. In this paper we study the break up of *N*-soliton bound state in a triangular GRIN waveguide with nonlocal nonlinearity. The study is based on the direct numerical solutions of the modified nonlinear Schrödinger (m-NLS) equation as well as the evolution of discrete eigenvalues of the corresponding Zakharov-Shabat spectral problem. For that purposes in Section 2 we review the beam propagation equation in non-homogeneous medium with nonlocal nonlinearity as well as the inverse scattering theory. Then we study in Section 3 the propagation of a single soliton in a triangular waveguide. It is shown that when a single soliton is launched in a triangular waveguide then it experiences transverse acceleration which depends on the

Copyright © 2012 SciRes.

strength of nonlocality as well as on its amplitude. Using these propagation properties in Section 4 we study the break up of *N*-soliton bound state into multiple single soliton. Finally conclusion will be given in the last section.

2. Basic Equation and Inverse Scattering Technique

We consider the evolution of beam propagating along the *z* axis in a slab waveguide with inhomogeneous linear refractive index in a transverse direction and first-order nonlocal contribution to nonlinear respond. Such beam propagation is described by the normalized modified nonlinear Schrödinger (m-NLS) equation, see [18]:

$$i\frac{\partial u}{\partial z}+\frac{1}{2}\frac{\partial^2 u}{\partial x^2}+|u|^2 u=(V_1+V_2)u\,, \tag{1}$$

where $V_1=-\Delta n(x)$ and $V_2=\mu\dfrac{\partial|u|^2}{\partial x}$ are respectively the contributions of linear refractive index inhomogeneity and nonlocality. Function $\Delta n(x)$ and parameter μ denote the profile of GRIN distribution and the strength of the nonlocal component of nonlinear response, respectively. The GRIN distribution in this paper is considered to have a triangular profile,

$$\Delta n(x)=\begin{cases}0, & x<-b\\ \Delta n_0\left(1+\dfrac{x}{b}\right), & -b\le x<0\\ \Delta n_0\left(1-\dfrac{x}{b}\right), & 0\le x<b\\ 0, & x\ge b\end{cases}, \tag{2}$$

where $2b$ is the total width of the waveguide and Δn_0 is the maximum index variation. Notice that the waveguide is symmetric where its center is located at $x=0$. In the absence of inhomogeneity and nonlocality, *i.e.* $\Delta n_0=\mu=0$, Equation (1) is known as the NLS equation. The NLS equation is integrable by the inverse scattering technique (IST) [19]. In this approach, the NLSE is associated with the Zakharov-Shabat eigenvalue problem (ZSEP),

$$\begin{aligned} i\frac{\mathrm{d}\psi_1}{\mathrm{d}x}+u(x)\psi_2&=\lambda\psi_1\\ -i\frac{\mathrm{d}\psi_2}{\mathrm{d}x}-u(x)^*\psi_1&=\lambda\psi_2, \end{aligned}\,, \tag{3}$$

where u is the beam envelope which acts as potential function and superscript * denotes the complex conjugate. If the linear *z*-evolution of the auxiliary spectral function $\Psi=(\psi_1,\psi_2)$ is given then the NLS equation can be resolved from the compatibility condition $\Psi_{zx}=\Psi_{xz}$. The continuous spectrum of ZSEP corresponds to waves that are radiated away; whereas a number of discrete eigenvalues $\lambda_j=(\kappa_j+i\eta_j)/2$, $j=1,2,\cdots,N$ corresponds to N soliton. Here $-\kappa_j$ and η_j define the velocity and the amplitude of the *j*-th soliton, respectively [20]. One of particular *N*-soliton is obtained if we consider an initial scattering potential

$$u(x,0)=Nq_0\,\mathrm{sech}\left(q_0(x-x_0)\right). \tag{4}$$

Satsuma and Yajima [21] showed that ZSEP (3) with initial potential (4) has eigenvalues which are purely imaginary

$$\lambda_j=iq_j/2=iq_0\left(N-j+\frac{1}{2}\right),\ j=1,2,\cdots,N\,. \tag{5}$$

This solution is called an *N*-soliton bound state or higher-order soliton because it contains *N* single soliton components which propagate together and always remain localized in *x* (the transversal velocity of each single soliton is zero, *i.e.* $\kappa_j=0,\forall j$).

In the absence of perturbations (e.g. linear refractive index variation and nonlocality) to the NLS equation, the ZSEP is iso-spectral (all eigenvalues are constant). In other words, the soliton content of a given input remains constant. In the presence of perturbations, the soliton eigenvalues are no longer *z*-invariant and the m-NLSE is not integrable and therefore the IST cannot be applied. However the ZSEP provide a powerful tool which enables us to monitor the dynamics of the discrete eigenvalues, *i.e.* the parameters of each individual soliton. In this case, when analyzing a certain potential (beam shape) at a distance *z*, the obtained discrete eigenvalues gives information about the soliton as if it would further propagate in an unperturbed medium. As long as the perturbations are small, the ZSEP holds likewise in the perturbed medium. In this paper, the soliton eigenvalues of the ZSEP will be determined numerically using procedure given in [22]. For this purpose, the potential $u(x,z)$ at distance *z* is obtained by solving the m-NLS equation using the conserved implicit Crank-Nicolson scheme [23].

3. Propagation of a Single Soliton

We begin with the propagation of a single soliton in a triangular GRIN waveguide by considering an input beam as in Equation (4) with $N=1$, $q_0=1$ and initial position at $x=x_0$. First we use waveguide parameters to be $\Delta n_0=0.1$, $b=5$, $x_0=-2.5$ and some values of μ. **Figures 1(a)-(c)** show the evolution of beam envelope for μ = 0, 0.01, 0.02 respectively. The corresponding eigenvalue evolutions are depicted in **Figures 1(d)-(f)** (imaginary parts/η) and **Figures 1(g)-(i)** (real parts/κ). It is shown that during the evolution, the imaginary part of eigenvalue (η) in all three cases is almost constant; indicating that the change of soliton amplitude during its

Copyright © 2012 SciRes.

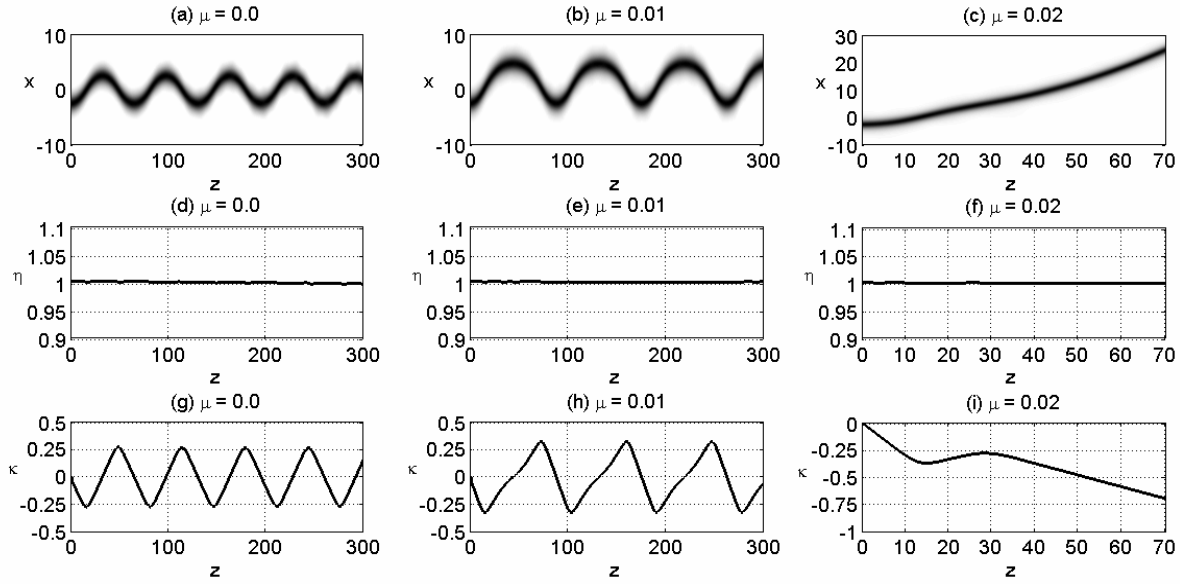

Figure 1. Propagation of a soliton with amplitude $q_0 = 1$ and initial position $x_0 = -2.5$ in a triangular GRIN waveguide with $\Delta n_0 = 0.1$, $b = 5$. The first row shows the evolution of beam envelope for (a) $\mu = 0.0$, (b) $\mu = 0.01$, and (c) $\mu = 0.02$. Dynamics evolution of the corresponding eigenvalue is shown in the second and third rows for the imaginary part and the real part of eigenvalue, respectively.

propagation is small. However, the real part of the eigenvalue (κ) is certainly not invariant. If the nonlinearity of medium is local ($\mu = 0.0$) then the real part of eigenvalue (κ) is a symmetric function around zero. This behavior shows that during the propagation the soliton oscillates symmetrically around the center of waveguide. In the medium with $\mu = 0.01$, the changing of κ is faster and bigger; meaning that the soliton experiences a larger acceleration. Nevertheless the soliton still oscillates but asymmetrically about the waveguide center. The effect of nonlocality is more pronounced if we further increase the nonlocality. Indeed, by taking $\mu = 0.02$, we see that the soliton propagates with much larger acceleration such that κ does not oscillate anymore. Here κ is always negative which means that the soliton always experiences positive velocity. It can be said that the waveguide does not support the oscillating soliton. Instead, the soliton is forced to exit the waveguide. Outside the waveguide, *i.e.* when $\Delta n(x) = 0$ the soliton propagates with a constant acceleration (or linear velocity). We remark that the eigenvalues evolution perfectly matched with the equivalent particle approach in [8].

Next we study the effect of soliton amplitude on its propagation in nonlocal triangular GRIN waveguide with $\Delta n_0 = 0.1$, $b = 5$, $\mu = 0.01$ and $x_0 = -2.5$ by varying q_0, see **Figure 2**. In **Figure 2(a)** we show the propagation of soliton with $q_0 = 0.5$. It is noticed that in this case the waveguide width is narrower than the soliton width and the index variation is sufficiently large. Consequently, part of soliton which is inside the waveguide will move faster to the wave center while another part remains outside the waveguide. Therefore the soliton is distorted and emits some radiation during its propagation. However it is clearly seen that the main part still oscillates in the waveguide. Such radiation is also described by the evolution of imaginary part of its eigenvalue (η); see **Figure 2(d)**. Here the value of η decreases which means that the soliton amplitude is getting smaller due to emitting radiation. The oscillation of the main part of beam is clearly seen from the real part of its eigenvalue (κ); see **Figure 2(g)**. We notice that the soliton in this case is not a single entity and therefore the equivalent particle approach presented in [8] cannot be applied. **Figures 2(b)-(c)** show that if we increase the soliton amplitude and therefore the soliton width is comparable to the width of waveguide then we hardly observe radiation during its propagation. This fact can also be seen from **Figures 2(e)-(f)** which show that each real part of its eigenvalue is practically speaking constant. However, we observed from **Figures 2(h)-(i)** that different amplitude soliton experiences different velocity. As mentioned in previous paragraph, the transversal velocity (κ) of soliton with amplitude $q_0 = 1$ oscillates around zero and therefore the soliton also oscillates around the waveguide center. In the case of larger amplitude ($q_0 = 1.5$), the soliton experiences much larger acceleration such that the transversal velocity is always positive (or κ is always negative). Therefore the soliton always moves to the right and exit from the waveguide. This behavior is in accordance with the prediction of equivalent particle theory given in [8].

Copyright © 2012 SciRes.

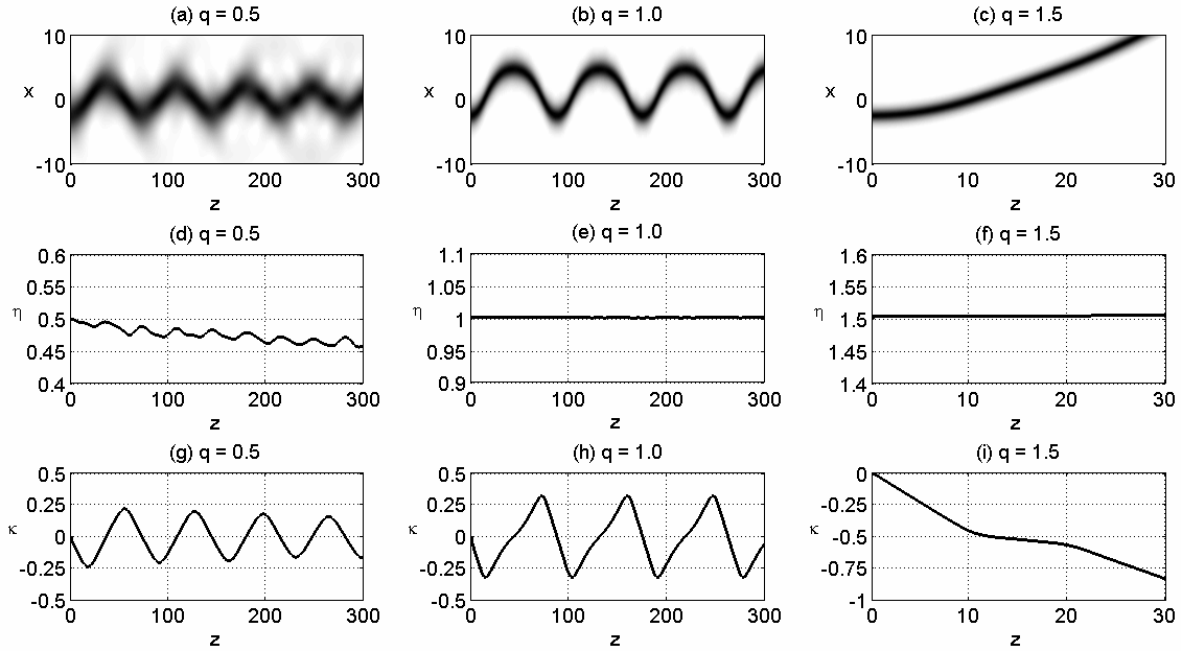

Figure 2. Propagation of a soliton with initial position $x_0 = -2.5$ in a nonlocal triangular GRIN waveguide with $\Delta n_0 = 0.1$, $b = 5$ and $\mu = 0.1$. The first row shows the evolution of beam envelope for (a) $q_0 = 0.5$ (b) $q_0 = 1$ and (c) $q_0 = 1.5$. Dynamics evolution of the corresponding eigenvalue is shown in the second and third rows for the imaginary part and the real part of eigenvalue, respectively.

4. Break up of *N*-Soliton Bound State

We continue with the dynamics of the beam evolution when the input contains several single solitons. As discussed in previous section, different strength of nonlocality causes different transversal velocity of soliton. Moreover, in the waveguide with the same strength of nonlocality, a single soliton with different amplitude also experiences different velocity ($-\kappa$). Hence, if the input beam is *N*-soliton bound state which consists of several single soliton with different amplitude then the bound state will certainly be destroyed because each soliton component experience different velocity. In other words the bound *N*-soliton bound state will break up when it propagates in a triangular GRIN waveguide with nonlocal nonlinearity. To illustrate the break up we perform several numerical experiments using initial condition given by Equation (4) with $N = 2$. The waveguide parameters are $\Delta n_0 = 0.1$ and $b = 5$. In **Figure 3** we show some numerical results using $q_0 = 0.75$ and $x_0 = -2.5$ for three different values of μ. Notice that the input beam initially consists of two single solitons of amplitude $\eta_1 = 0.75$ and $\eta_2 = 2.25$ with zero velocity. It is seen from **Figure 3** that during the evolution in the waveguide with $\mu = 0$, $\mu = 0.001$ and $\mu = 0.005$, each imaginary part of eigenvalues (η) which corresponds to the amplitude of single solitons is relatively constant. This fact shows that the break up process almost does not affect the soliton amplitude. But each real part of eigenvalues changes immediately after the bound state enters the waveguide. The break up process can be considered as an interaction of two single solitons moving with different velocity. Due to this interaction, the velocity of each soliton certainly differs from that of a single soliton propagating alone. In the waveguide with local nonlinearity ($\mu = 0$), after bound state breaks up into two solitons, each soliton constituent oscillates in the waveguide with different period. Since they have different oscillation period, a collision of the two solitons will certainly be predicted. The collision forces the smaller soliton ($\eta_1 = 0.75$) to exit the waveguide and then continue to propagate in the left side of waveguide with constant velocity. The higher soliton ($\eta_2 = 2.25$) in this case remains oscillating inside the waveguide. We further observe in **Figure 3** that the increasing strength of nonlocality (μ) leads to much larger velocity of soliton with higher amplitude ($\eta_2 = 2.25$) and therefore speeds up the splitting process of bound soliton. As a result, the higher amplitude soliton ($\eta_2 = 2.25$) exits and propagates to the right part of the waveguide while the lower amplitude soliton ($\eta_1 = 0.75$) oscillates inside the waveguide.

To see the effects of amplitude and initial position of soliton, we plot some results of numerical simulations using the same parameters as in **Figure 3** except $q_0 = 0.8$ and three different initial positions; see **Figure 4**. Since $N = 2$ and $q_0 = 0.8$, our initial beam consists of two single solitons with amplitude $\eta_1 = 0.8$ and $\eta_2 = 2.4$

Copyright © 2012 SciRes.

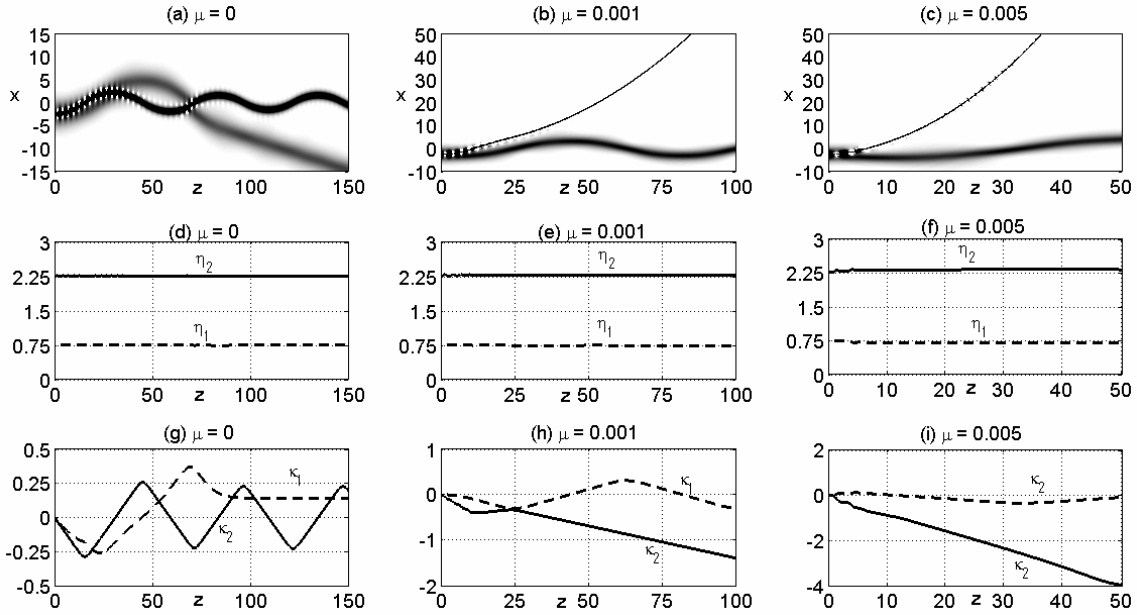

Figure 3. Break up of 2-soliton bound state in a triangular GRIN waveguide with $\Delta n_0 = 0.1$, $b = 5$, where the initial position of bound state is $x_0 = -2.5$ and $q_0 = 0.75$. The first row shows the evolution of beam envelope for (a) $\mu = 0$, (b) $\mu = 0.001$ and (c) $\mu = 0.005$. Dynamics evolution of the corresponding eigenvalue is shown in the second and third rows for the imaginary part and the real part of eigenvalue, respectively.

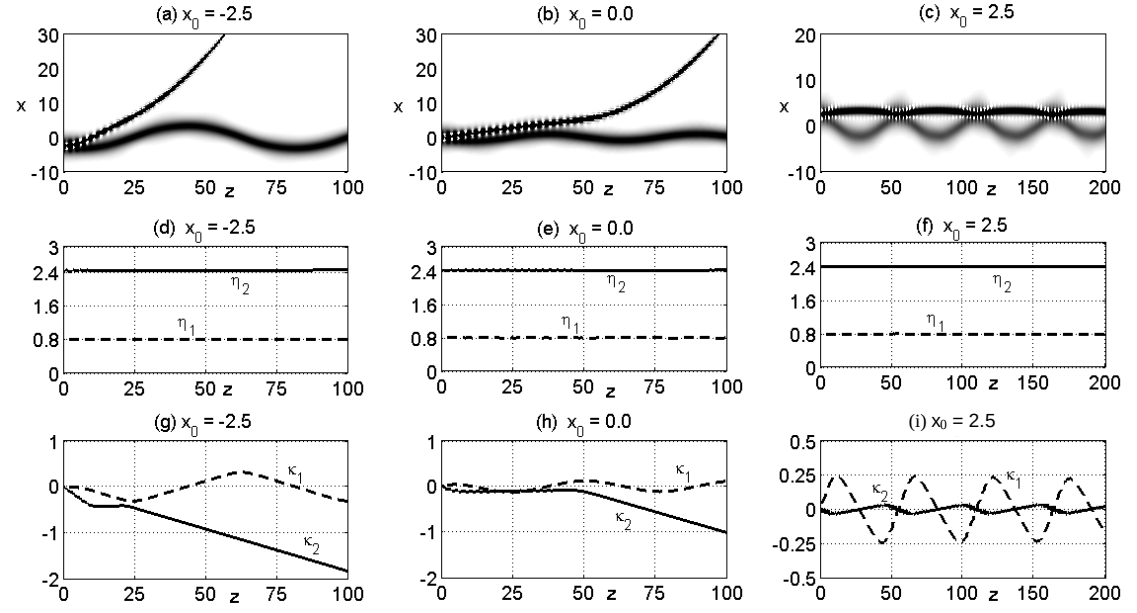

Figure 4. Break up of 2-soliton bound state with $q_0 = 0.8$ in a triangular GRIN waveguide with $\Delta n_0 = 0.1$, $b = 5$ and $\mu = 0.001$. The first row shows the evolution of beam envelope for three different initial positions, *i.e.* (a) $x_0 = -2.5$, (b) $x_0 = 0$ and (c) $x_0 = 2.5$. Dynamics evolution of the corresponding eigenvalue is shown in the second and third rows for the imaginary part and the real part of eigenvalue, respectively.

respectively, see Equations (3) and (4). Using $q_0 = 0.75$ and $q_0 = 0.8$ with the same initial position, we observe that these two cases give the same qualitative break up process of *N*-soliton bound state; see **Figures 3(b)**, **(e)** and **(h)** and **Figures 4(a)**, **(d)** and **(g)**. Here the lower soliton oscillates inside the waveguide while the higher soliton exits from the waveguide. However, detail observation shows that soliton with amplitude $\eta_2 = 2.4$ has

Copyright © 2012 SciRes.

larger velocity or acceleration (see **Figures 4(a)-(g)**) than that with amplitude $\eta_2 = 2.25$ (see **Figures 3(b)-(h)**). This is caused by the fact that the higher amplitude soliton experiences larger nonlocality effect. If the initial position of bound state is shifted to the waveguide center, *i.e.* at $x_0 = 0$ we see that the break up process is also qualitatively the same as if the bound state is initially placed at $x_0 = -2.5$. But the break up process of bound state with initial position $x_0 = 0$ is slower than that with $x_0 = -2.5$. Different splitting process is obtained if the initially position of bound state is at $x_0 = 2.5$, see **Figure 4(c)**. Although the higher soliton ($\eta_2 = 2.4$) experiences larger velocity but it does not exit the triangular GRIN waveguide. In this case both solitons oscillate inside the waveguide with different period and therefore they experience consecutive collisions. We see that the consecutive collisions of two solitons is almost periodically and there is no soliton moving out from the waveguide until the propagation distance z = 200. This behavior can be seen clearly from the evolution of beam envelope in **Figure 4(c)** as well as from the velocity ($-\kappa$) in **Figure 4(i)**.

5. Conclusion

We have investigated numerically the splitting of *N*-soliton bound state in a waveguide with nonlocal nonlinearity where the linear refractive index has a triangular profile. The splitting of *N*-soliton bound state is caused by the fact that each soliton components of the bound state experiences different acceleration induced by both refractive index variation and nonlocal nonlinearity. It is also found that the splitting process of the *N*-soliton bound state does not affect the amplitude of all single soliton components.

6. Acknowledgements

This research is supported by Direktorat Penelitian dan Pengabdian kepada Masyarakat, Direktorat Jenderal Pendidikan Tinggi Indonesia (Penelitian Unggulan Perguruan Tinggi—Hibah Doktor via DIPA (RM) Universitas Airlangga SK No. 2613/H3/KR/2012, No. Kontrak 4074/H3.6/PPd/2012).

REFERENCES

[1] S. H. Crutcher, A. J. Osei and M. E. Edwards, "Optical Spatial Solitons, the Power Law, and the Swing Effect," *Proceedings of SPIE*, Vol. 7056, 2008, Article ID: 70560Q. doi:10.1117/12.792007

[2] M. Ebnali-Heidari, M. K. Moravvej-Farshi and A. Zarifkar, "Swing Effect of Spatial Solitons Propagating through Gaussian and Triangular Waveguides," *Applied Optics*, Vol. 48, No. 26, 2009, pp. 5005-5014. doi:10.1364/AO.48.005005

[3] W. Krolikowski and O. Bang, "Solitons in Nonlocal Nonlinear Media: Exact Solutions," *Physical Review E*, Vol. 63, No. 1, 2000, Article ID: 016610. doi:10.1103/PhysRevE.63.016610

[4] V. Aleshkevich, Y. Kartashov and V. Vysloukh, "Self-Bending of the Coupled Spatial Soliton Pairs in a Photorefractive Medium with Drift and Diffusion Nonlinearity," *Physical Review E*, Vol. 63, No. 1, 2000, Article ID: 016603. doi:10.1103/PhysRevE.63.016603

[5] J. Petter, C. Weilnau, C. Denz, A. Stepken and F. Kaiser, "Self-Bending of Photorefractive Solitons," *Optics Communications*, Vol. 170, No. 4, 1999, pp. 291-297. doi:10.1016/S0030-4018(99)00485-X

[6] Y. V. Izdebskaya, V. G. Shvedov, A. S. Desyatnikov, W. Krolikowski and Y. S. Kivshar, "Soliton Bending and Routing Induced by Interaction with Curved Surfaces in Nematic Liquid Crystals," *Optics Letters*, Vol. 35, No. 10, 2010, pp. 1692-1694. doi:10.1364/OL.35.001692

[7] A. Suryanto and I. Darti, "Soliton Steering in a Ramp Waveguide with Nonlocal Nonlinearity," *Journal Nonlinear Optical Physics and Materials*, Vol. 20, No. 1, 2011, pp. 33-41. doi:10.1142/S0218863511005826

[8] A. Suryanto and I. Darti, "Dynamics of Spatial Soliton in a Gradient Refractive Index Waveguide with Nonlocal Nonlinearity," *International Journal of Applied Mathematics and Statistics*, Vol. 28, No. 4, 2012, pp. 23-30. http://www.ceser.in/ceserp/index.php/ijamas/article/view/1337

[9] S. V. Manakov, S. P. Novikov, L. P. Pitaevskii and V. E. Zakharov, "Theory of Solitons," Consultants Bureu, New York, 1984.

[10] V. A. Aleshkevich, Y. V. Kartashov, A. S. Zelenina, V. A. Vysloukh, J. P. Torres and L. Torner, "Eigenvalue Control and Switching by Fission of Multisoliton Bound States in Planar Waveguides," *Optics Letters*, Vol. 29, No. 5, 2004, pp. 483-485. doi:10.1364/OL.29.000483

[11] A. Suryanto and E. van Groesen, "Break up of Bound-N-Spatial-Soliton in a Ramp Waveguide," *Optical Quantum Electronics*, Vol. 34, No. 5, 2002, pp. 597-606. doi:10.1023/A:1015685122513

[12] A. Suryanto and E. van Groesen, "Self-Splitting of Multisoliton Bound States in Planar Waveguides," *Optics Communications*, Vol. 258, No. 2, 2006, pp. 264-274. doi:10.1016/j.optcom.2005.07.063

[13] K. Zhou, Z. Guo and S. Liu, "Position Dependent Splitting of Bound States in Periodic Photonic Lattices," *Journal of the Optical Society of America B*, Vol. 27, No. 5, 2010, pp. 1099-1103. doi:10.1364/JOSAB.27.001099

[14] Y. V. Kartashov, L. C. Crasovan, A. S. Zelenina, V. A. Vysloukh, A. Sanpera, M. Lewenstein and L. Torner, "Soliton Eigenvalue Control in Optical Lattices," *Physical Review Letters*, Vol. 93, No. 14, 2004, Article ID: 143902. doi:10.1103/PhysRevLett.93.143902

[15] O. Katz, Y. Lahini and Y. Silberberg, "Multiple Break up of High-Order Spatial Soliton," *Optics Letters*, Vol. 33, No. 23, 2008, pp. 2830-2832. doi:10.1364/OL.33.002830

[16] J. E. Prilepsky and S. A. Derevyanko, "Breakup of a

Copyright © 2012 SciRes.

Multisoliton State of the Linearly Damped Nonlinear Schrodinger Equation," *Physical Review E*, Vol. 75, No. 3, 2007, Article ID: 036616. doi:10.1103/PhysRevE.75.036616

[17] S. Pu, C. Hou, K. Zhan, C. Yuan and Y. Du, "Spatial Solitons in Nonlocal Materials with Defocusing Effects," *Optics Communications*, Vol. 285, No. 6, 2012, pp. 1456-1460. doi:10.1016/j.optcom.2011.11.037

[18] Y. V. Kartashov, V. A. Vysloukh and L. Torner, "Tunable Soliton Self-Bending in Optical Lattices with Nonlocal Nonlinearity," *Physical Review Letter*, Vol. 93, No. 15, 2004, Article ID: 153903. doi:10.1103/PhysRevLett.93.153903

[19] V. E. Zakharov and A. B. Shabat, "Exact Theory of Two-Dimensional Self-Focusing and One-Dimensional Self-Modulation of Waves in Nonlinear Media," *Journal of Experimental and Theoretical Physics*, Vol. 34, No. 1, 1972, pp. 62-69. http://www.jetp.ac.ru/cgi-bin/e/index/e/34/1/p62?a=list

[20] A. Hasegawa and Y. Kodama, "Solitons in Optical Communications," Clarendon Press, Oxford, 1995.

[21] J. Satsuma and N. Yajima, "Initial Value Problems of One-Dimensional Self-Modulation of Nonlinear Waves in Dispersive Media," *Progress of Theoretical Physics Supplement*, No. 55, 1974, pp. 284-306.

[22] P. Chamorro-Posada, G. S. McDonald, G. H. C. New and F. J. Fraile-Pelaez, "Fast Algorithm for the Evolution of Optical Solitons under Perturbations," *IEEE Transactions on Magnetics*, Vol. 35, No. 3, 1999, pp. 1558-1561. doi:10.1109/20.767268

[23] I. Darti, Suhariningsih, Marjono and A. Suryanto, "A Conservative Finite Difference Scheme for Simulation of Soliton in Inhomogeneous Medium with Nonlocal Nonlinearity," *International Journal of Mathematics and Computation*, Vol. 13. No. D11, 2011, pp. 69-77. www.ceser.in/ceserp/index.php/ijmc/article/view/1153

Copyright © 2012 SciRes.

Optics and Photonics Journal, 2012, 2, 185-192
doi:10.4236/opj.2012.23028 Published Online September 2012 (http://www.SciRP.org/journal/opj)

Enhancement in Light Extraction Efficiency of GaN-Based Light-Emitting Diodes Using Double Dielectric Surface Passivation

Chung-Mo Yang[1], Dong-Seok Kim[1], Yun Soo Park[1], Jae-Hoon Lee[2], Yong Soo Lee[1], Jung-Hee Lee[1]
[1]School of Electrical Engineering and Computer Science, Kyungpook National University, Daegu, South Korea
[2]GaN Power Research Group, R & D Institute, Samsung LED Co., Ltd., Suwon, South Korea
Email: jlee@ee.knu.ac.kr

Received June 27, 2012; revised July 26, 2012; accepted August 8, 2012

ABSTRACT

SiO_2/Al_2O_3 double dielectric stack layer was deposited on the surface of the GaN-based Light-Emitting Diode (LED). The double dielectric stack layer enhances both the electrical characteristics and the optical output power of the LED because the first Al_2O_3 layer plays a role of effectively passivating the p-GaN surface and the second lower index SiO_2 layer increases the critical angle of the light emitted from the LED surface. In addition, the effect of the Fresnel reflection is also responsible for the enhancement in output power of the double dielectric passivated LED. The leakage current of the LED passivated with Al_2O_3 layer was -3.46×10^{-11} A at –5 V, at least two and three orders lower in magnitude compared to that passivated with SiO_2 layer (-7.14×10^{-9} A) and that of non-passivated LED (-1.9×10^{-8} A), respectively, which indicates that the Al_2O_3 layer is very effective in passivating the exposed GaN surface after dry etch and hence reduces nonradiative recombination as well as reabsorption of the emitted light near the etched surface.

Keywords: GaN; Light-Emitting Diode (LED); Al_2O_3; PEALD; Passivation; Double Dielectric Stack Layer

1. Introduction

The III-nitrides are suitable materials for photoelectronic applications covering most of the electromagnetic spectrum due to their wide range of direct bandgap energy. Light emitting diodes (LEDs) are promising semiconductor devices for solid state lighting. Due to a remarkable development in LED fabrication technologies, the LEDs are now being commercialized in various applications such as traffic signals, full-color displays, back lighting in liquid-crystal displays, and so on [1]. However, further improvement in output power with long life time is still required for the GaN-based LED to be more efficiently used in such a field. The increase of the external quantum efficiency (η_{EQE}), which can be determined from the product of injection efficiency (η_{inj}) × radiative efficiency (η_{rad}) × extraction efficiency (η_{ext}), is the most important factor in achieving a high efficiency LED. η_{inj} and η_{rad} can be increased by improving the crystal quality and optimizing the epitaxial layer structure which maximizes the radiative recombination in active region. Surface passivation with appropriate dielectric layers is also necessary to avoid non-radiative recombination for high η_{rad} [2]. Special techniques such as control of surface roughness [3-5], preparation of patterned sapphire substrate (PSS) [6,7], application of flip-chip bonding [8-10], adaption of laser lift-off process [11], and formation of photonic crystal structure [12] are frequently used to improve η_{ext}, which can be increased by increasing the critical angle for the emitted light through an appropriate modification of the surface of the LED [13,14]. Anti-reflection (AR) coating of dielectric layers is frequently used to reduce the Fresnel reflection at the semicon- ductor-air interface in communication LEDs.

In this work, we report, in more detail, the development of passivation technique for the GaN-based LEDs by using double dielectric stack layer design is not optimized for the maximum anti-reflectivity.

2. Device Fabrication

Figure 1(a) shows the schematic LED configuration investigated in this work. The layer structure was grown on the patterned sapphire substrate (PSS) by metal-organic chemical vapor deposition (MOCVD). The blue LED structure contains low temperature grown GaN buffer layer, un-doped GaN layer, Si doped n-GaN layer, InGaN/GaN multi-quantum well active layer and Mg doped p-GaN cladding layer. The composition and thickness of InGaN/GaN multi-quantum well active layer was opti-

Copyright © 2012 SciRes.

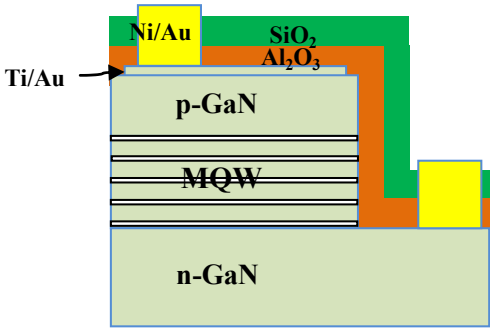

(a)

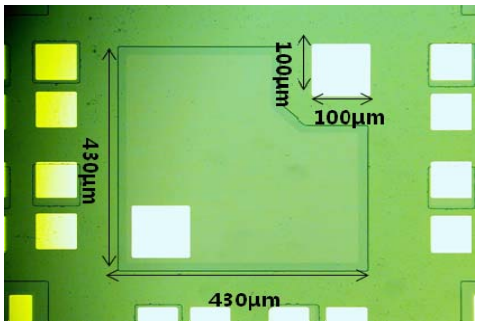

(b)

Figure 1. The schematic of the LED configuration investigated in this work (a); and the fabrication of the 430 μm × 430 μm size real LED chip (b).

mized for emission wavelength of ~460 nm. **Figure 1(b)** shows the fabricated LED chip with size of 430 μm × 430 μm.

The window for n-electrode was first defined by dry etching and a transparent electrode consisting of Ni/Au (50 Å/50 Å) was deposited on p-GaN layer, which was followed by rapid thermal annealing at 500˚C (at N_2/O_2 ambient) for ohmic contact between the transparent electrode and p-GaN top layer. Thick Ti/Au bonding pads with thickness of 300 Å/4000 Å was then deposited. The double dielectric stack layer, which consists of 5 nm-thick Al_2O_3 layer [15] deposited by plasma-enhanced atomic layer deposition (PEALD) and 50 nm-thick SiO_2 layer deposited by plasma-enhanced chemical vapor deposition (PECVD), was sequentially deposited on the surface of the LED to complete the fabrication process. The PEALD method has the advantages such as an excellent uniformity, a high quality film density, a controllability of atom level thickness and the perfect surface step coverage for the LED structure due to the self-limiting deposition characteristic. A gas phase reaction can be suppressed among the injected reactant. Therefore, a thin film layer is formed by a saturated surface reaction therefore the low temperature deposition is possible. In addition, to evaluate the interface trap density between SiO_2 or Al_2O_3 layer and p-GaN layer, the MOS capacitors with anode pattern of 300 μm diameter and virtual ground contact [16] were also fabricated. For comparison, three different LEDs were also prepared; 5 nm-thick single Al_2O_3-passivated, 50-nm thick single SiO_2-passivated, and non-passivated LED.

3. Optimization of Double Dielectric Stack Layer

To maximize the optical output power, the refractive index and the thickness of a dielectric layer, were estimated from the concept based on the Fresnel reflection for the antireflection. The Fresnel reflection at the interface can be reduced to zero, assuming normal incidence, when an anti-reflective dielectric layer is inserted between air and semiconductor, which has the following relations:

$$\text{Refranctive index}: n_{AR} = \sqrt{n_S \times n_A} \quad (1)$$

and

$$\text{thickness} = \frac{\lambda}{4} = \frac{\lambda_0}{4n_{AR}} \quad (2)$$

where n_{AR} is a refractive index of anti-reflection layer, n_S is a refractive index of semiconductor, n_A is a refractive index of air, and λ is wavelength, respectively. The estimated refractive index and the thickness of an anti-refraction layer is 1.55 and ~70 nm, respectively, when the semiconductor is GaN and the emission wavelength λ is 460 nm. To obtain n_{AR} of 1.55 with double dielectric stack layer, such as Al_2O_3 (refractive index of 1.77)/SiO_2 (refractive index of 1.46) investigated in this work, the thickness ratio between two dielectric layers is approximately 7(SiO_2):3(Al_2O_3), which approximately corresponds to the SiO_2 thickness of 50 nm and the Al_2O_3 thickness of 20 nm. However, the 5 nm-thick Al_2O_3 layer was used for the double layer in this work, instead of the calculated value of 20 nm because the reverse current characteristics of the Al_2O_3-passivated LED become rapidly degraded as the thickness increases as shown in **Figure 2(a)** (the leakage current of the 5 and 20 nm thick Al_2O_3 passivated layer were -3.46×10^{-11} A and the 2.21×10^{-8} A at –5 V, respectively).

The degradation in reverse characteristics is believed to be due to the time dependent plasma damage, where the surface damage increases as the exposure time of the LED surface to the plasma increases during the deposition of dielectric layers. The plasma damage may lead to the formation of lattice defects and/or dangling bonds at near-surface which results in the degradation in output power of LEDs as shown in **Figure 2(b)** [17,18].

The output power of the LED with 20 nm-thick Al_2O_3 layer is considerably decreased compared to other LEDs with thinner Al_2O_3 layer. For this reason, the 5 nm-thick Al_2O_3 layer was chosen to minimize the plasma damage. Additionally, the 5 nm-thick Al_2O_3 layer plays a role of not only very effective passivation layer of the LED sur-

Copyright © 2012 SciRes.

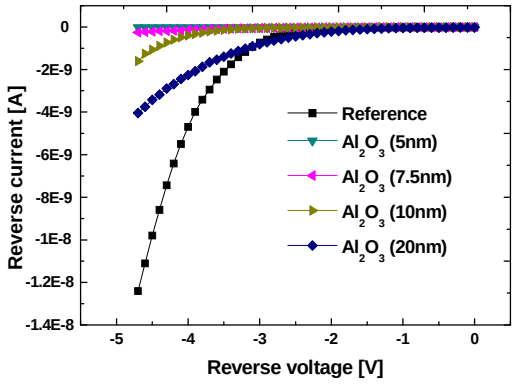

(a)

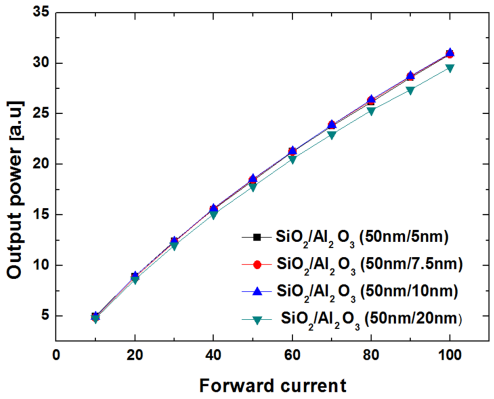

(b)

Figure 2. The the leakage current characteristics (a) and the output power characteristics (b) of the SiO_2 (50 nm)/Al_2O_3 (5 nm), SiO_2 (50 nm)/Al_2O_3 (7.5 nm), SiO_2 (50 nm)/Al_2O_3 (10 nm), and SiO_2 (50 nm)/Al_2O_3 (20 nm)-passivated LEDs, respectively.

face but also partially anti-reflective layer in combination with 50 nm-thick SiO_2 layer even though the thickness is thinner than the calculated value for the anti-reflective layer. As a result, the total thickness for the double dielectric stack layer was optimized as 55 nm to achieve an efficient operation of the LED even though the thickness is not optimized for the maximum anti-reflectivity.

4. Results and Discussion

The linear and semi-log I-V characteristics of all fabricated LEDs are shown in **Figures 3(a)** and **(b)**. The forward voltages measured at 20 mA were approximately 3.31, 3.33, 3.39 and 3.39 V for the non-passivated, the Al_2O_3-passivated, the SiO_2-passivated, and the SiO_2/Al_2O_3-passivated LED, respectively. The forward voltages of the Al_2O_3, the SiO_2 and the SiO_2/Al_2O_3-passivated LEDs are slightly higher than that of the non-passivated LED. It is a little difficult to observe the difference in slopes between LEDs. To clearly see the difference, we compared the I-V curves for only two LEDs in (c) of the figure with the non-passivated LED and the SiO_2/Al_2O_3 double

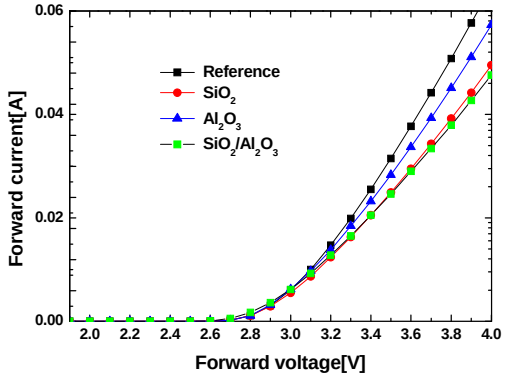

(a)

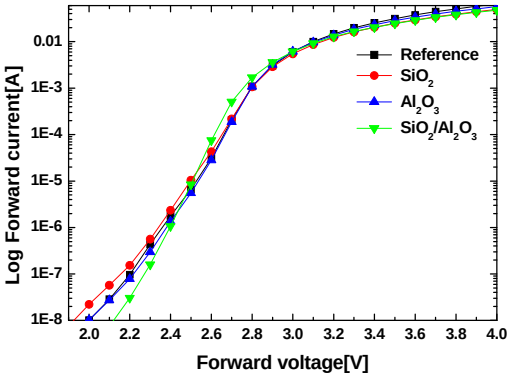

(b)

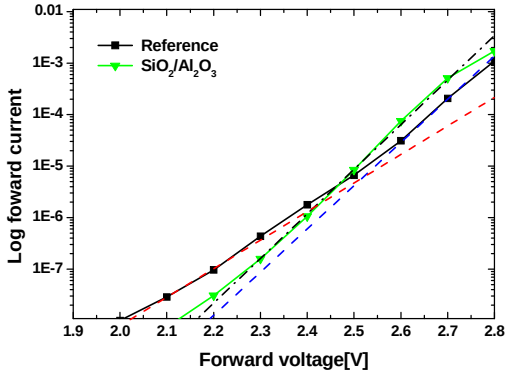

(c)

Figure 3. The linear and semi-log I-V characteristics for all investigated LEDs at forward bias (a) and (b). To clearly see the difference, we compared the I-V curves for only two LEDs in (b) of the figure with non-passivated LED and the SiO_2/Al_2O_3 double dielectric passivated LED.

dielectric passivated LED. It is apparent that the non-passivated LED exhibits two characteristic lines, with a small slope at relatively low bias (<2.5 V) caused by which is equivalent to the surface shunt resistance and parasitic diode showing the prematured turn-on [19] as described later. On the other hand, the SiO_2/Al_2O_3 double dielectric passivated LED shows almost one dominant characteristic line with large slope, but the line with small slope disappears except at very low bias below ~2.2 V.

Copyright © 2012 SciRes.

This explains that the I-V characteristic of the non-passivated LED is greatly affected by the existence of the shunt components at surface showing a hump in the curve, while that of the SiO_2/Al_2O_3 double dielectric passivated LED is less affected by these shunt components due to the effective surface passivation of the SiO_2/Al_2O_3 double dielectric layer. Therefore, the SiO_2/Al_2O_3 double dielectric passivated LED exhibits much more improved output power performance due to the decreased non-radiative recombination at surface. However, it is noticed that the SiO_2 passivated LED exhibits even worse I-V characteristic than that of the non-passivated one with even further prematured turn-on as shown in the figure. This is probably because the GaN surface becomes easily damaged when the surface is exposed to the plasma during the long deposition time, while the damage becomes minimized for the SiO_2/Al_2O_3 double dielectric passivation because the first thin Al_2O_3 layer deposited prior to the SiO_2 deposition prevents the GaN surface from being damaged. The GaN surface can be passivated with the deposition of the SiO_2 layer, which can be resulted in decrease of the effect of the shunt diode at surface. However, the plasma damage introduced during the deposition of the SiO_2 layer causes another surface leakage which is responsible for the worse I-V characteristic for the SiO_2 passivated LED. The passivation effect of the 5 nm-thick Al_2O_3 single dielectric layer is not remarkable compared to that of the double dielectric-passivation as shown in the **Figure 3(b)**. This is believed to be due to the insufficient surface passivation caused by nonuniform surface covering of the dielectric layer when the dielectric layer is very thin.

At a higher current level, however, the dielectric passivated LEDs exhibit larger series resistances than the non-passivated LED does as shown in the **Figure 4**.

The reason for the increased resistance with dielectric passivation can be understood by adopting an equivalent circuit model, as shown in **Figure 5(a)**, for the LED investigated in this work. The model consists of the main ideal bulk p-n diode (D_1), the contact resistance (R_C), the bulk series resistance (R_{SB}) mainly due to highly resistive p-type layer, the shunt resistance (R_{SS}), and the parasitic shunt diode (D_2) [19]. The shunt diode (D_2) and the shunt resistance (R_{SS}) are due to the surface leakage related to the surface states. The I-V characteristics of non-passivated LED can be inferred, considering all intrinsic and parasitic components. The I-V characteristics for D_1 (dotted-black line) can be degraded due to R_{SB} and R_C (dotted-blue line) as shown in **Figure 5(b)**. The curve for D_2 with R_{SS} is also shown as the dotted-green line in the figure. Therefore, the observable I-V characteristics for the non-passivated LED must be sum of the characteristics of the two diodes, shown as the dotted-red line in the figure.

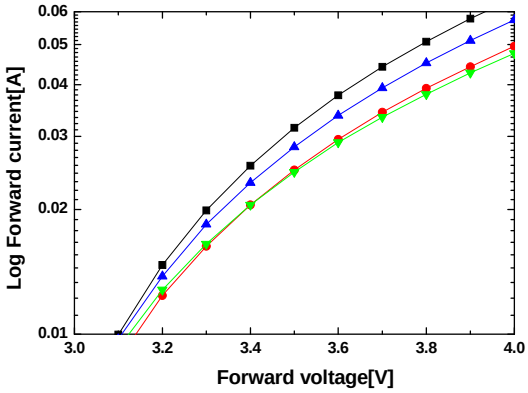

Figure 4. The semi-log I-V characteristics for all investigated LEDs at high forward bias.

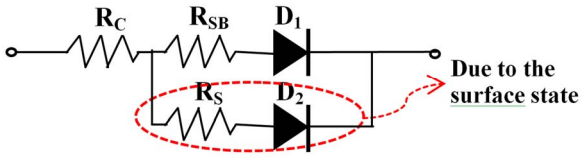

(a)

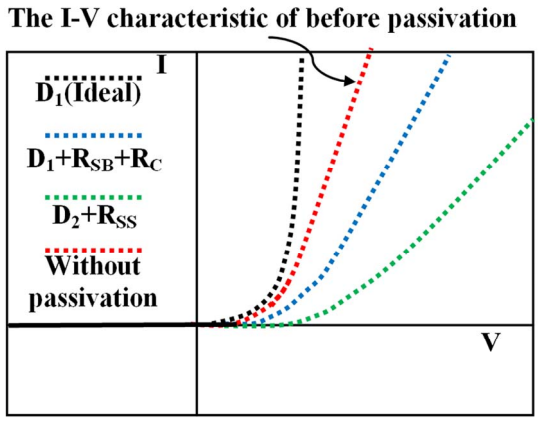

(b)

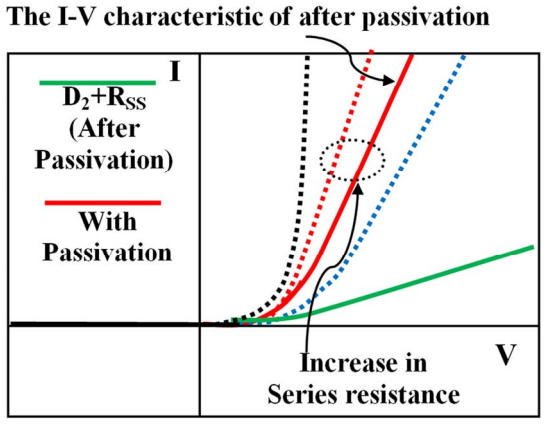

(c)

Figure 5. The Equivalent circuit model of the LED investigated in this work (a); the I-V characteristics of LEDs without (b); and with (c) passivation.

Copyright © 2012 SciRes.

The I-V characteristics for D_1 with R_C and R_{SB} do not change even after passivation. However, the portion of D_2 with R_{SS} in the I-V characteristics becomes much reduced because the passivation layer greatly decreases the surface state density. This means that the effect of D_2 and R_{SS} on the total diode characteristics becomes less which can be visualized as green line in **Figure 5(c)**. Therefore, the I-V characteristics for the passivated LED, obtained from the sum of the characteristics of the two diodes (the broken blue line + the green line), can be drawn as red line in the figure, where the slope of the I-V curve is smaller than that of the I-V curve before the passivation, indicating that the series resistance of the passivated LED is larger than that of the non-passivated LED. The premature turn-on observed for the passivated LED is probably due to the surface leakage, which cannot be fully eliminated by the passivation, and/or additional shunt resistance, caused by plasma damage.

Figure 6 shows the reverse leakage current characteristics for the fabricated LEDs. As shown in the figure, the leakage current of the Al_2O_3-passivated LED was -3.46×10^{-11} A at the –5 V, at least two and three orders lower in magnitude compared to that of the SiO_2-passivated LED (-7.14×10^{-9} A) and the non-passivated LED (-1.9×10^{-8} A), respectively.

This indicates that the Al_2O_3 layer is very effective in passivating the exposed GaN surface after dry etch and hence decreases the trap density near the surface, which minimizes the leakage current through the surface of the LED. The trap density at the GaN surface was obtained by estimating the flatband voltage shift of the metal-insulator-semiconductor (MIS) capacitors, which depends on the polarity and the density of charges in the oxide and at the interface [20]. The measured C-V data were compared to the theoretical values using the Equation (3) below and the flatband voltage shift can be calculated.

$$V_{FB} = \Phi_M - \chi_S - \left[\frac{E_g}{2} - \frac{kT}{q}\ln\frac{N}{n_i}\right] - \frac{Q_F}{C_{OX}} - \frac{Q_{IT}}{C_{OX}} \quad (3)$$

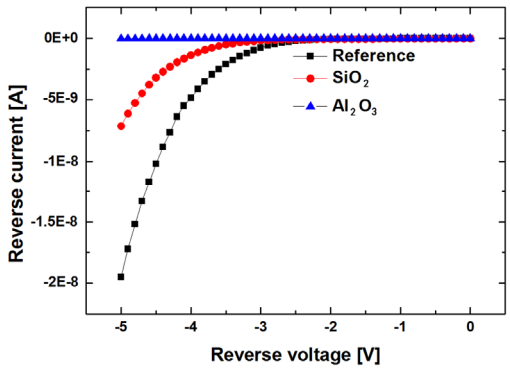

Figure 6. The LED with Al_2O_3 layer exhibits at least two and three orders lower in leakage current compared to that with SiO_2 layer and without dielectric layer, respectively.

where Φ_M is the metal work function, χ_S is the electron affinity of the semiconductor, E_g is the band gap energy, k is the Boltzmann constant, T is the temperature, q is the elementary charge, N is the doping density, n_i is the intrinsic carrier concentration, Q_F is the density of fixed charges, Q_{IT} is the density of interface trap charges, and C_{ox} is the oxide capacitance. The first three terms represent the ideal flatband valtage and the latter two causes the flatband voltage shift which depends on the polarity and the density of charges in the oxide and at the interface. The estimated interface trap density obtained from the Q_{IT} are shown in **Table 1**. The decreased trap density with Al_2O_3 passivation at the GaN surface leads to decrease in nonradiative surface recombination, which in turn increases the radiative efficiency and hence the output power from the LED.

Figure 7 shows the output powers versus currents for all LEDs studied in this work, which demonstrates the output powers of dielectric-passivated LEDs are higher than that of the non-passivated LED. The output power is 25.8, 26.5, 27.9, and 32.3 for the non-passivated, the SiO_2-passivated, the Al_2O_3-passivated, and the Al_2O_3/SiO_2-passivated LED at I_F = 100 mA, respectively.

The reason for the higher output power for the dielectric passivated LED is because an additional transparent layer with refractive index n on NiAu/GaN as well as on the etched LED surface results in a larger critical angle for the emitted light. It is also noticed that the output power of the Al_2O_3-passivated LED is slightly higher than

Table 1. Characteristics of interface charge density in GaN MIS structures.

material	value
Al_2O_3	2.6×10^{11} $eV^{-1}\cdot cm^{-2}$
SiO_2	6.2×10^{12} $eV^{-1}\cdot cm^{-2}$

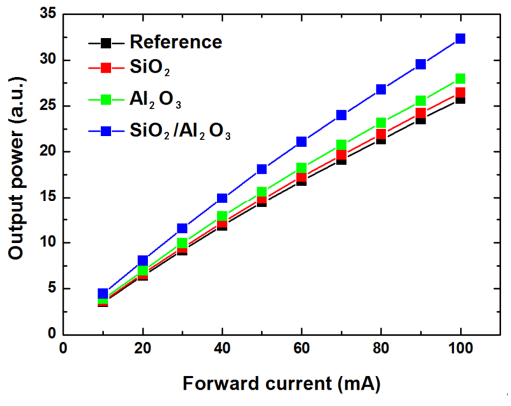

Figure 7. The output power characteristics of the non-passivated, the SiO_2-passivated, the Al_2O_3-passivated, and the Al_2O_3/SiO_2-passivated LED. The output power of the Al_2O_3/SiO_2-passivated LED exhibits about 25% higher than that of the non-passivated LED.

Copyright © 2012 SciRes.

that of the SiO_2-passivated LED, which is unexpected and must be discussed, and the double dielectric Al_2O_3/SiO_2-passivated LED exhibits further enhanced output power. The output power of the SiO_2-passivated LED must be higher than that of the Al_2O_3-passivated LED, because the lower index of the SiO_2 layer deposited on the LED plays a role of increasing the light extraction efficiency due to larger critical angle factor as shown in **Table 2**, which is contrary to the result observed in **Figure 7**. According to the Snell's law, the critical angle (θ_{crit}) of total internal reflection is given by

$$\theta_{crit} = \sin^{-1}\left(\frac{n_2}{n_1}\right) \quad (4)$$

where n_1 and n_2 are the refractive indices of the semiconductor and air, respectively.

The reason why the Al_2O_3-passivated LED exhibits higher output power can be explained as follow; the Al_2O_3 layer covers whole surface of the LED, as shown in **Figure 1**, including the side-wall surface near the edge of the active quantum well exposed after plasma etching, except the n- and p-type contact. This Al_2O_3 layer effectively passivates the surface of the LED, which not only improves the electrical property of the LED by effectively reducing surface leakage as described before, but also reduces probability of nonradiative recombination through the surface trap and increases the radiative recombination efficiency in the active quantum well near side-wall edge. Furthermore, this passivation layer prevents the reabsorption of the emitted light near the surface regions. The surface passivation with Al_2O_3 layer, therefore, leads to increase of overall the external efficiency of the LED, even though the extraction efficiency of the Al_2O_3-passivated LED itself is lower than that of the SiO_2-passivated LED.

The output power of the Al_2O_3-passivated LED can be further increased by depositing additional 50 nm-thick SiO_2 layer on the Al_2O_3 layer to form the SiO_2/Al_2O_3 double dielectric stack layer. The output power of the LED with the double dielectric stack layer exhibits an output power, about 25.4% higher than that of the non-passivated LED and 15.6% higher than that of the Al_2O_3-passivated LED, respectively. This remarkable enhancement in output power of the LED with double dielectric passivation is because the first Al_2O_3 layer plays a role of effectively passivating the p-GaN surface and the second lower index SiO_2 layer plays a role of increasing the critical angle of the light emitted from the LED surface. In addition, the effect of the Fresnel reflection are also responsible for this enhancement in output power of the double dielectric passivated LED. Assuming normal incidence of light, the Fresnel power transmittance between GaN and air without any dielectric layer is given by

$$T = 1 - R = 1 - \left(\frac{n_{GaN} - n_{air}}{n_{GaN} + n_{air}}\right)^2 = \frac{4n_{GaN}n_{air}}{\left(n_{GaN} + n_{air}\right)^2} \quad (5),$$

when thin dielectric layer, SiO_2 or Al_2O_3, is inserted between GaN and air, the transmittance can be expressed as below, neglecting multiple reflections between dielectric layers for simple calculation.

$$T = 1 - R = \frac{4n_{GaN}n_{SiO_2}}{\left(n_{GaN} + n_{SiO_2}\right)^2} \times \frac{4n_{SiO_2}n_{air}}{\left(n_{SiO_2} + n_{air}\right)^2}, \quad (6)$$

or

$$T = 1 - R = \frac{4n_{GaN}n_{Al_2O_3}}{\left(n_{GaN} + n_{Al_2O_3}\right)^2} \times \frac{4n_{Al_2O_3}n_{air}}{\left(n_{Al_2O_3} + n_{air}\right)^2}. \quad (7)$$

Similarly, when double dielectric stack layer, SiO_2/Al_2O_3, is inserted between GaN and air,

$$T = \frac{4n_{GaN}n_{Al_2O_3}}{\left(n_{GaN} + n_{Al_2O_3}\right)^2} \times \frac{4n_{Al_2O_3}n_{SiO_2}}{\left(n_{Al_2O_3} + n_{SiO_2}\right)^2} \times \frac{4n_{SiO_2}n_{air}}{\left(n_{SiO_2} + n_{air}\right)^2} \quad (8)$$

where n_{GaN}, $n_{Al_2O_3}$, n_{SiO_2}, and n_{air} are the refractive indices of the GaN, Al_2O_3, SiO_2 and air, respectively. The above equations can be formalized as below:

$$T = 1 - R = \Pi_{i=1}^{3} \frac{4n_i n_{i+1}}{\left(n_i + n_{i+1}\right)^2} \quad (9)$$

where i = 1 corresponds to the case without dielectric layer, i = 2 corresponds to the case with single dielectric layer (SiO_2 or Al_2O_3), and i = 3 corresponds to the case with double dielectric layer (SiO_2/Al_2O_3), respectively. From the above equation, the Fresnel power transmittances of the LED without a dielectric layer, with SiO_2, the Al_2O_3, and Al_2O_3/SiO_2 can be approximately calculated as 83.0%, 90.9%, 90.2%, and 93.5%, respectively. The calculated Fresnel power transmittance of the LED with double dielectric passivation, assuming normal incidence of the light, is approximately 10% higher than that that of non-passivated LED. This factor must be included in the improvement of the output power of the LED with double dielectric passivation, along with the contribution from the enhanced radiative recombination efficiency near side-wall edge as described before, which results in increase in the overall extraction efficiency from the LED.

Table 2. The critical angle calculated of dielectric deposited on GaN surface.

Passivation method	Critical angle
Al_2O_3	34.4 degrees
SiO_2	43.2 degrees
No dielectric	24.3 degrees

Copyright © 2012 SciRes.

5. Conclusion

We have proposed a new concept of surface passivation for the GaN-based LED to improve the light extraction efficiency by using SiO_2/Al_2O_3 double dielectric stack layer and investigated its effects on the output power of the LED. The double dielectric stack layer not only effectively passivates the surface of the LED, but also enhances the overall extraction efficiency of the LED. The LED with the SiO_2/Al_2O_3 double dielectric stack layer exhibited about a 25.4% increase in the output power compared to the non-passivated LED.

6. Acknowledgements

This work was supported by Kyungpook National University Research Fund 2012, 2008 Brain Korea 21 (BK21), the National Research Foundation of Korea (NRF) grant funded by the Korea government (MEST) (No. 2012-0005671, 2012-0000627), R & D program of MKE/KETEP (2011101050017B, "Development of high efficiency GaN power device for an power grid inverter system"), and WCU (World Class University) program through the Korea Science and Engineering Foundation funded by the Ministry of Education, Science and Technology (R33-10055), and the IT R & D program of MKE/KEIT (10038766, Energy Efficient Power Semiconductor Technology for Next Generation Data Center).

REFERENCES

[1] T. Fujii, Y. Gao, R. Sharma, E. L. Hu, S. P. Den Baars and S. Nakamura, "Increase in the Extraction Efficiency of GaN-Based Light-Emitting Diodes via Surface Roughening," *Applied Physics Letters*, Vol. 84, No. 6, 2004, pp. 855-857. doi:10.1063/1.1645992

[2] C. M. Yang, D. S. Kim, S. G. Lee, J. H. Lee, Y. S. Lee and J. H. Lee, "Improvement in Electrical and Optical Performances of GaN-Based LED with SiO_2/Al_2O_3 Double Dielectric Stack Layer," *IEEE Electron Device Letters*, Vol. 33, No. 4, 2012, pp. 564-566. doi:10.1109/LED.2012.2185675

[3] H.-W. Huang, C. C. Kao, J. T. Chu, S. C. Wang and C. C. Yu, "Improvement of InGaN-GaN Light-Emitting Diode Performance with a Nano-Roughened p-GaN Surface," *IEEE Photonics Technology Letters*, Vol. 17, No. 5, 2005, pp. 983-985. doi:10.1109/LPT.2005.846741

[4] C. M. Tsai, J. K. Sheu, W. C. Lai, Y. P. Hsu, P. T. Wang, C. T. Kuo, C. W. Kuo, S. J. Chang and Y. K. Su, "Enhanced Output Power in GaN-Based LEDs with Naturally Textured Surface Grown by MOCVD," *IEEE Electron Device Letters*, Vol. 26, No. 7, 2005, pp. 464-466. doi:10.1109/LED.2005.851243

[5] M. Y. Hsieh, C. Y. Wang, L. Y. Chen, T. P. Lin, M. Y. Ke, Y. W. Cheng, Y. C. Yu, C. P. Chen, D. M. Yeh, C. F. Lu, C. F. Huang, C. C. Yang and J. J. Huang, "Improvement of External Extraction Efficiency in GaNBased LEDs by SiO_2 Nanosphere Lithography," *IEEE Electron Device Letters*, Vol. 29, No. 7, 2008, pp. 658-660. doi:10.1109/LED.2008.2000918

[6] J. H. Lee, J. T. Oh, S. B. Choi, Y. C. Kim, H. I. Cho and J. H. Lee, "Enhancement of InGaN-Based Vertical LED with Concavely Patterned Surface Using Patterned Sapphire Substrate," *IEEE Photonics Technology Letters*, Vol. 20, No. 5, 2008, pp. 345-347. doi:10.1109/LPT.2007.915648

[7] J. H. Lee, J. T. Oh, Y. C. Kim and J. H. Lee, "Stress Reduction and Enhanced Extraction Efficiency of GaN-Based LED Grown on Cone-Shape-Patterned Sapphire," *IEEE Photonics Technology Letters*, Vol. 20, No. 18, 2008, pp. 1563-1565. doi:10.1109/LPT.2008.928844

[8] C. F. Shen, S. J. Chang, W. S. Chen, T. K. Ko, C. T. Kuo and S. C. Shei, "Nitride-Based High-Power Flip-Chip LED with Double-Side Patterned Sapphire Substrate," *IEEE Photonics Technology Letters*, Vol. 19, No. 10, 2007, pp. 780-782. doi:10.1109/LPT.2007.896574

[9] S. H. Huang, R. H. Horng, K. S. When, Y. F. Lin, K. W. Yen and D. S. Wuu, "Improved Light Extraction of Nitride-Based Flip-Chip Light-Emitting Diodes via Sapphire Shaping and Texturing," *IEEE Photonics Technology Letters*, Vol. 18, No. 24, 2006, pp. 2623-2625. doi:10.1109/LPT.2006.886823

[10] O. B. Shchekin, J. E. Epler, T. A. Trottier, T. Margalith, D. A. Steigerwald, M. O. Holcomb, P. S. Martin and M. R. Krames, "High Performance Thin-Film Flip-Chip InGaN-GaN Light-Emitting Diodes," *Applied Physics Letters*, Vol. 89, No. 7, 2006, Article ID: 071109. doi:10.1063/1.2337007

[11] S. J. Wang, K. M. Usang, S. L. Chen, Y. C. Yang, S. C. Chang, T. M. Chen, B. W. Liou and C. H. Chen, "Use of Patterned Laser Liftoff Process and Electroplating Nickel Layer for the Fabrication of Vertical-Structured GaN-Based Light-Emitting Diodes," *Applied Physics Letters*, Vol. 87, 2005, Article ID: 011111. doi:10.1063/1.1993757

[12] H. W. Huang, C. H. Lin, Z. K. Huang, K. Y. Lee, C. C. Yu and H. C. Kuo, "Improved Light Output Power of GaN-Based Light-Emitting Diodes Using Double Photonic Quasi-Crystal Patterns," *IEEE Electron Device Letters*, Vol. 30, No. 11, 2009, pp. 1152-1154. doi:10.1109/LED.2009.2029985

[13] M. F. Schubert, F. W. Mont, S. Chhajed, D. J. Poxson, J. K. Kim and E. F. Schubert, "Design of Multilayer An- tireflection Coatings Made from Co-Sputtered and Low-Refractive-Index Materials by Genetic Algorithm," *Optics Express*, Vol. 16, No. 8, 2008, pp. 5290-5298. doi:10.1364/OE.16.005290

[14] J.-Q. Xi, M. F. Schubert, J. K. Kim, E. F. Schubert, M. Chen, S.-Y. Lin, W. Liu and J. A. Smart, "Optical Thin-Film Materials with Low Refractive Index for Broadband Elimination of Fresnel Reflection," *Nature Photonics*, Vol. 1, No. 3, 2007, pp. 176-179.

[15] S.-J. So and C.-B. Park, "Improvement of Brightness with Al_2O_3 Passivation Layers on the Surface of InGaN/GaN-Based Light-Emitting Diode Chips," *Thin Solid Film*, Vol. 516, No. 8, 2008, pp. 2031-2034.

Copyright © 2012 SciRes.

doi:10.1016/j.tsf.2007.07.143

[16] C. Ostermaier, H.-C. Lee, S.-Y. Hyun, S.-I. Ahn, K.-W. Kim, H.-I. Cho, J.-B. Ha and J.-H. Lee, "Interface Characterization of ALD Deposited Al_2O_3 on GaN by CV Method," *Physica Status Solidi*, Vol. 5, No. 6, 2008, pp. 1992-1994.

[17] Y. Li, X. Y. Yi, X. D. Wang, J. X. Guo, L. C. Wang, G. H. Wang, F. H. Yang, Y. P. Zeng and J. M. Li, "Plasma Induced Damage in GaN-Based Light Emitting Diodes," *SPIE Proceedings*, Vol. 6841, 2007, Article ID: 68410x. doi:10.1117/12.759809

[18] H. S. Yang, S. Y. Han, K. H. Baik and S. J. Pearton, "Effect of Inductively Coupled Plasma Damage on Performance of GaN-InGaN Multiquantum-Well Light-Emitting Diodes," *Applied Physics Letters*, Vol. 86, 2005, Article ID: 102104. doi:10.1063/1.1882749

[19] E. F. Schubert, "Light-Emitting Diodes," 2nd Edition, Cambridge University Press, Cambridge, 2006. doi:10.1017/CBO9780511790546

[20] K. Matocha, R. J. Gutmann and T. P. Chow, "Effect of Annealing on GaN-Insulator Interfaces Characterized by Metal-Insulator-Semiconductor Capacitors," *IEEE Transactions on Electron Devices*, Vol. 50, No. 5, 2003, pp. 1200-1204. doi:10.1109/TED.2003.813456

Copyright © 2012 SciRes.

Optics and Photonics Journal, **2012, 2, 193-199**
doi:10.4236/opj.2012.23029 Published Online September 2012 (http://www.SciRP.org/journal/opj)

Primary Study of the Use of Laser-Induced Plasma Spectroscopy for the Diagnosis of Breast Cancer

Hisham Imam[1], Raeesa Mohamed[2,3], Ashraf A. Eldakrouri[1,4]
[1]National Institute of Laser Enhanced Sciences, Cairo University, Giza, Egypt
[2]College of Medicine, Cairo University, Giza, Egypt
[3]College of Medicine, King Saud University, Riyadh, KSA
[4]College of Applied Medical Science, King Saud University, Riyadh, KSA
Email: hishamimam@niles.edu.eg

Received June 20, 2012; revised July 17, 2012; accepted July 29, 2012

ABSTRACT

Breast cancer, or malignant breast neoplasm, is a type of cancer that originates from breast tissue, most commonly from the inner lining of the milk ducts or the lobules that supply the ducts with milk. It is one of the most widespread diseases, especially in women. Thus far, large efforts have been towards the early diagnosis of cancer in general, and breast cancer specifically. Most of these techniques deal with malignant tissues without inducing or increasing pathological tissue changes or causing major side effects for the patient. This paper proposes a new technique for diagnosing the presence or occurrence of cancer and assessing its grade early, accurately, and safely. The presented technique depends on the interaction between the laser and the soft tissue in order to induce plasma, and allows us to classify the cancer by studying the difference in the intensity ratio of the trace elements in normal and malignant tissues. The results presented here show that only four patients out of the total sample of 30 have erroneous trace elements and that this does not affect the overall decision. Hence, the performance of LIPS can be measured as 87%, while retaining 100% accuracy. Furthermore, LIPS technique is a simple and promising technique that is capable of diagnosing malignant cells and tissues.

Keywords: LIPS; Malignant; Breast

1. Introduction

Laser-Induced Plasma Spectroscopy (LIPS), also known as Laser-Induced Breakdown Spectroscopy, is a form of atomic emission spectroscopy. When the output from a (pulsed) laser focuses on a small spot of a solid surface, an optically induced plasma, frequently called a laser induced plasma, laser-ablated plasma, or laser spark is formed on this surface. Plasma, which is defined as "the fourth state of matter," occurs as an electrified gas with the atoms dissociated into positive ions and negative electrons. Further, it may be defined alternatively as a medium whose dielectric properties are determined only by free charges.

LIPS technique consists of three main parts, namely an ablation laser, a detector, and focusing and collection optics. This technique utilizes the high power densities obtained by focusing the radiation from a pulsed, fixed frequency laser (usually Nd:YAG) to generate a luminous micro-plasma in the focal region of an analyte. The energy density in the focal region can reach values up to GW/cm^2. Part of the laser pulse energy is used to ablate the sample of interest; subsequently, the material in the plasma core is vaporized and atomized. The plasma temperature can reach several electron volts and the plasma is typically highly ionized. In a good approximation, the plasma composition is representative of the analyte's elemental composition [1]. This technique has been used extensively for qualitative determinations with great success as well as successfully used for the elemental analysis of solids, liquids, gases, and aerosols, meaning that it is increasingly applied in basic and applied research [2].

Analyses for trace elements in biological tissue are uniquely susceptible to extreme errors unless special precautions are taken during collection, storage, and analysis. The integrity of the specimen can be compromised before it is analyzed, by contamination during collection and processing or by the attenuation of the analytic concentration during storage. If this happens, the determined values are not valid even though the method of analysis is extremely sensitive and highly accurate [3].

Breast cancer (also known as malignant breast neoplasm) is a type of cancer that originates from breast tissue, most commonly from the inner lining of the milk ducts (ductal carcinomas) or the lobules (lobular carcinomas) that supply the ducts with milk. It is a disease that afflicts hu-

Copyright © 2012 SciRes.

mans and other mammals. While the overwhelming majority of cases are women, men can also develop breast cancer [4].

Although most types of breast cancers are easy to diagnose through the microscopic analysis of a biopsy, rarer types of breast cancers require specialized examination. Further, while screening techniques are useful in determining the possibility of cancer, further testing is necessary to confirm whether a lump detected during a screening is cancerous as opposed to a benign alternative such as a simple cyst [5].

Both mammography and clinical breast examinations can indicate the approximate likelihood that a lump is cancerous, while both approaches can also detect other lesions. When the test results are inconclusive, however, fine needle aspiration cytology may be used. Other options for carrying out a biopsy include a core biopsy, where a section of the breast lump is removed, and an excisional biopsy, where the entire lump is removed. In addition, a vacuum-assisted breast biopsy may help diagnose breast cancer among selected female patients [6]. Further, carcinoma in situ is the growth of low-grade cancerous or precancerous cells within a particular tissue compartment such as the mammary duct without the invasion of the surrounding tissue. By contrast, invasive carcinoma is not confined to the initial tissue compartment.

Breast cancer can be graded by comparing the appearance of breast cancer cells with that of normal breast tissue. Whereas normal cells in an organ such as the breast are usually differentiated, meaning that they take on specific shapes and forms that reflect their function as part of that organ, cancerous cells lose that differentiation. In cancer, the cells that would usually line up in an orderly way to make up the milk ducts thus become disorganized, cell division becomes uncontrolled, and cell nuclei become less uniform. Pathologists describe cells as well differentiated (low grade), moderately differentiated (intermediate grade), and poorly differentiated (high grade) as the cells progressively lose the features seen in normal breast cells. Poorly differentiated cancers have a worse prognosis [7].

The calculation of electron density using the LIPS technique shows that differences between normal and malignant cells might be supported by the hypothesis that an alteration in glucose uptake within malignant cells may cause these tissues to have elevated electron density [8]. Indeed, previous studies have reported that the concentration of trace elements varies for cancerous and noncancerous cells [9,10]. This research has shown a clear distinction between intensity based on the concentration of trace elements in normal and malignant tissues, finding that the concentration of trace elements such as calcium, iron, and manganese is larger in normal cells in comparison with malignant cells. The ratio of the intensity of different atomic lines observed in the LIPS signal compared with that for the calcium line has also been compared.

The present research aims to distinguish between normal and malignant tumor cells from histological sections by using LIPS in order to measure in real time the concentrations of trace elements. The overall objective is for this technique to be incorporated with laser scalpels in order to monitor the cancer-affected area during surgery. We believe this technique has the potential to be an automated, real-time diagnostic procedure for cancer that would greatly facilitate the diagnosis and classification of tumors.

2. Materials and Methods

The plasma was formed with the aid of a Q-switched Nd:YAG laser (Continuum, Surellite II, USA) operating at the fundamental wavelength (1064 nm) with a pulse duration of 10 ns and a variable repetition rate in the range 1 - 10 Hz. The temporal history of the plasma was obtained by recording the emission features at predetermined delay times using a variable delay generator, which is triggered by the laser pulse. The laser beam with pulse energy of 350 mJ was used for sample ablation. Energy was adjusted using a suitable combination of beam splitters at a constant high voltage (1.3 kV) and a Q-switch delay to ensure spatial and temporal beam profile stability.

An energy meter (Nova, Ophir Optronics Ltd., USA) was employed to monitor the shot-to-shot pulse energy. The laser was a single pulse with an optimized delay time (td) of 1500 ns and an optimized gate width (tw) of 10,000 ns. The beam from the pulsed laser was passed through a quartz plano-convex lens (10 cm focal length) and focused on the sample in order to create a spark or breakdown in the medium. The light emission from the sample was collected and conveyed to the Echelle spectrometer (SE200PI-HO, Princeton, USA) by means of a 1 m long fused-silica optical fiber mounted on a micro-xyz translation stage. The Echelle spectrometer provided a constant spectral resolution of 3100 (CSR), over a wavelength range of 190 - 1100 nm, displayable in a signal spectrum.

A getable, intensified ICCD camera, (Princeton, IMAX) coupled to the spectrometer was used to detect the dispersed light. To avoid electronic interference and jitters, the intensifier high voltage was triggered optically. The Echelle grating spectrometer provides high resolution in a more compact size and covers a much wider spectral range compared with conventional grating spectrometers [11].

Emission spectra were analyzed using the commercial GRAMS Spectroscopic Data Analysis software (version 8.0; Galactic Industrial Salem, NH, USA), which reads data from the chip and reconstructs the spectrum. This makes it possible to measure a large wavelength range simultaneously with a high spectral resolution. In addition to the atomic database used by the mentioned soft-

Copyright © 2012 SciRes.

ware, spectral lines were identified by the latest electronically published database [http://webbook.nist.gov]. Both malignant and normal tissue cells were exposed to Nd:YAG laser pulses of a sufficient energy level to induce the plasma at 1064 nm. No real sample preparation was needed to take the LIPS measurements, because the malignant and normal tissue cells were placed on a glass plate and the laser light was focused in such a way that not only the base glass but also the ablation of the cells took place.

Atomic absorption spectroscopy was used to estimate the concentrations of the studied elements (*i.e.*, zinc, copper, iron, manganese, and calcium concentrations) and then the same samples in normal and malignant breast tissues were measured using the LIPS technique. The samples of known weight were first prepared. Each sample was kept in a dry clean vial and maintained until analyzed. Tissue samples were then digested using the dry weight technique, which is a simple and efficient digestion method for rapid sample preparation and quantification-assisted acid digestion by concentrated nitric acid. After digestion, the samples were diluted using distilled water and then assayed by an atomic absorption spectrophotometer.

The emission intensities of each element were normalized to the emission intensity of the calcium line (393.36 nm) in order to reduce the effect of instrument signal fluctuation and matrix interference effects, where calcium was considered to be a constant constituent of the analyzed samples. The steps necessary to analyze the sample using the LIPS technique were also straightforward, namely exposing the malignant and normal tissue cells to the focused laser pulses as shown in the experimental setup in **Figure 1**.

The light emitted from the laser-produced plasma on the sample surface was collected by an optical fiber cable and fed to the Echelle spectrometer. The dispersed light was then transformed into its corresponding emission spectrum in the ICCD camera and displayed on a PC for further analysis using the GRAMS software.

Each sample was measured five times at five different spots on the malignant and normal tissue cell samples. These five obtained spectra were then averaged to obtain the final spectrum, as shown in **Figure 2**. The concentration of each element was calculated by replacing its relative intensity in its specific calibration curve equation [12].

Thirty surgical specimens of breast cancer cases were randomly obtained from patients aged from 30 to 65 years old. Sixteen surgical specimens were obtained by excisional biopsy and 14 by radical mastectomy operation. All specimens were fixed in formalin (10% formaldehyde in

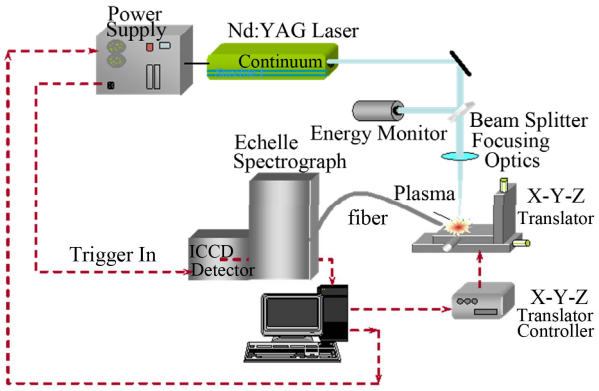

Figure 1. The experimental setup for the LIPS technique.

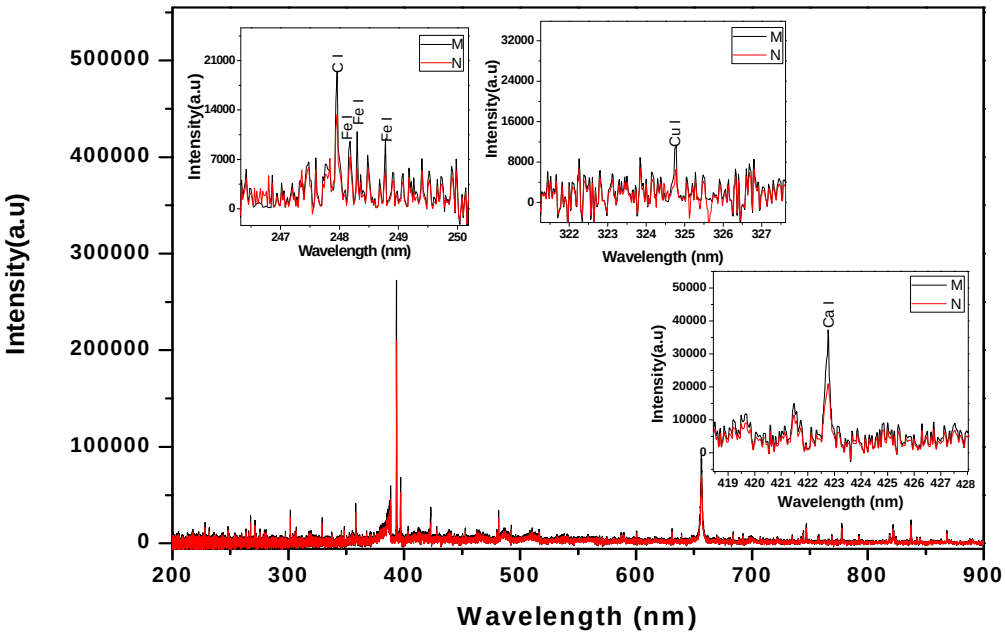

Figure 2. LIBS spectrum of malignant and normal tissues, with zoomed segments of Ca, Cu, C and Fe lines.

Copyright © 2012 SciRes.

water) and then histologically processed to form paraffin blocks, which were sectioned at 4 μm using a microtome. These sections were layered on a glass slide for staining and the slides were embedded for 2 minutes in hematoxylin (which stains the nuclei blue) and then eosin (which stains the cytoplasm and the extracellular connective tissue matrix pink). The histological slides were finally examined under a microscope.

3. Results and Discussion

The 30 reports classified each breast cancer case into two types: lobular and/or ductal. Examples of a pathology photo of a ductal carcinoma and a lobular carcinoma are presented in **Figure 3**. This classification of the cases yielded 27 (90%) ductal carcinoma cases and three cases (10%) of lobular carcinoma (**Figure 3**).

As mentioned in the Materials and Methods, each sample was measured five times after its exposure to the Nd:YAG laser beam in order to create a plasma on the surface of the tissue. The five spectrum segments of the normal and malignant samples were then recorded, where five laser shots on each sample were accumulated with a delay time (t_d) of 1500 ns and a gate width (t_w) of 10,000 ns. The wavelengths of interest were 393.6 nm and 422.6 nm for Ca, 388.6 nm for Fe, 324.75 nm for Cu, 334.5 nm for Zn, and 259.37 nm for Mn. The results of the Ca concentrations in malignant and normal samples are presented in **Figure 4**. The concentrations of Zn, Cu, Mn, and Fe in each sample were normalized to that of Ca in the same sample. These measurement results are presented in **Figures 5-8**. The results obtained using the LIPS technique showed an enhancement in the concentration levels of the tested trace elements (Ca, Zn, Cu, Mn, and Fe) in the malignant breast tissue samples compared with the levels of the normal ones. Voting as a decision-level fusion method is the simplest approach to fusing the outputs of multiple estimates or predictions by emulating the way in which humans reach consensus. The fused output decision is thus based on majority rule (*i.e.*, the maximum number of votes wins). Variations in voting techniques include weighted voting (*i.e.*, in which sensors are given relative weights), plurality, and consensus methods.

To implement this structure, each classification or prediction, *i*, outputs a binary vector, X*i*, with D elements (*i.e.*, the number of hypothesized output decisions). The binary vectors are combined into a matrix X, with row *i* representing the input from sensor *i*. The voting fusion structure then sums the elements in each column as described by the following equation:

$$y(j) = \sum_{i=1}^{N} \mathrm{X}(i, j) \quad \text{For } j = 1 : \mathrm{D}$$

The output, $y(j)$, is a vector of length D, where each element indicates the total number of votes for output class *j*. At time k, the decision rule selects the output, D (k), as the class that carries the majority vote, according to the following Equation:

$$\mathrm{D}(\mathrm{k}) = \arg j \ \max y(j)$$

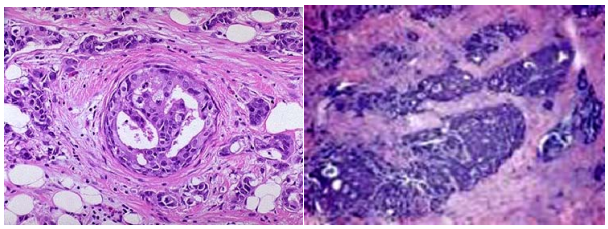

Figure 3. Example of pathology photos of a ductal and a lobular carcinoma.

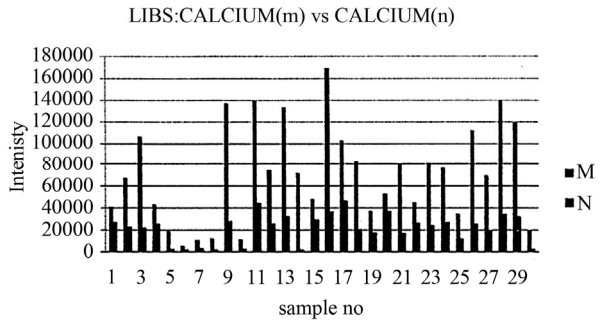

Figure 4. Relation between calcium in malignant and normal tissues using LIPS.

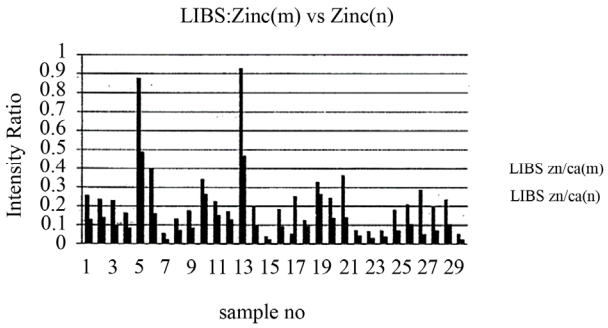

Figure 5. Relation between zinc to calcium ratio in malignant and normal tissues.

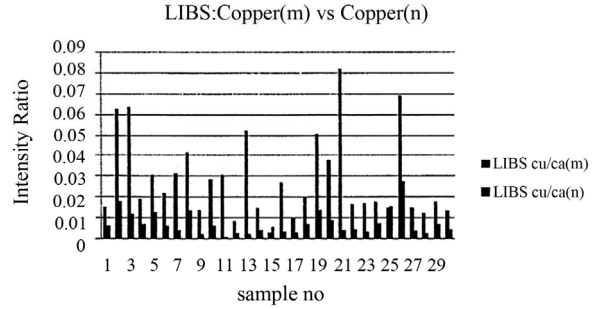

Figure 6. Relation between copper/calcium ratio in malignant and normal tissues.

Copyright © 2012 SciRes.

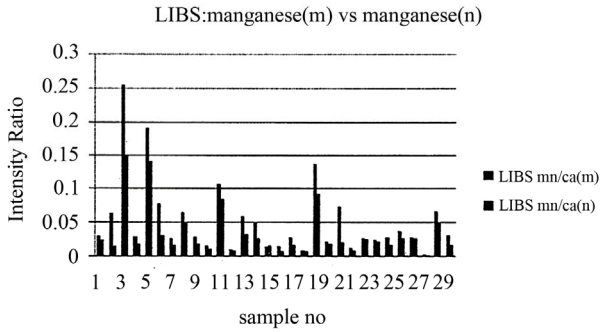

Figure 7. Relation between magnesium/calcium ratio in malignant and normal tissues.

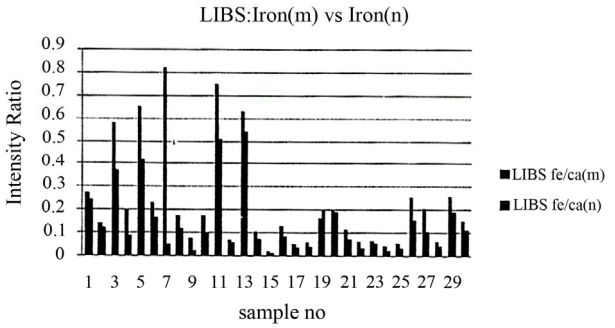

Figure 8. Relation between iron/calcium ratio in malignant and normal tissues.

The voting algorithm generates a decision for a certain problem by taking the votes of more than one decision element. The decision is then taken by considering the majority of votes as a global decision. In the breast cancer diagnostics using LIPS, five factors were thus measured and considered to be decision members. These factors were the normalized traces elements, namely copper, zinc, calcium, manganese, and iron.

One of the advantages of the LIPS approach is the ease of collecting data on a computer in a standardized form. These data sheets are picked up instantaneously by the voting algorithm and run against it to quickly decide whether cells are normal or malignant. The voting algorithm runs once for every trace element and "votes" for each element as normal or malignant. A counter is then started to tally the number of votes for each case, with a final decision taken at the end of the algorithm, namely after the last trace element has been tested. The malignant/normal decision-making flowchart used in this study is presented in **Figure 9**.

The data collection phase of the testing procedure yielded differences in the intensity values of malignant and normal tissue samples (**Table 1**). If the difference was a positive value (*i.e.*, the malignant intensity was higher than the normal intensity), an increment in the malignant counter occurred, and vice versa. The voting algorithm yielded accurate results for the 30 investigated samples. As expected,

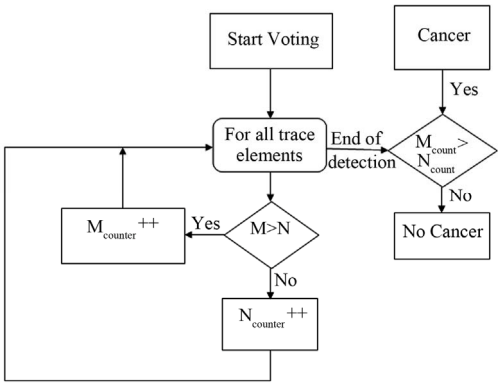

Figure 9. Voting algorithm for malignant/normal decision making.

Table 1. Differences between malignant and normal samples.

Ser.	Ca	Zn/Ca	Cu/Ca	Fe/Ca	Mn/Ca	Malignant Votes
1	1467.05	0.12911	0.009044	0.028954	0.00673	5
2	590.8444	0.098722	0.045062	0.020025	0.05016	5
3	1364.88	0.12688	0.052093	0.213208	0.10411	5
4	5162.47	0.08004	0.0123	0.116513	0.011505	5
5	247.83	0.38793	0.01783	0.237205	0.05082	5
6	656.35	0.23675	0.015903	0.06623	0.04668	5
7	2576.443	0.031895	0.027123	0.772881	0.0108	5
8	406.7111	0.05753	0.027773	0.0544	0.01671	5
9	301.5877	0.09417	0.011495	0.05344	0.01063	5
10	927.3522	0.08011	0.022256	0.073763	0.005732	5
11	7183.167	0.07072	0.029818	0.240977	0.02213	5
12	4997.667	0.0439	0.006009	0.01026	0.001867	5
13	240.2	0.458	0.050526	0.089778	0.026903	5
14	890.28	0.10277	0.010736	0.031029	0.0225	5
15	987	0.0152	–0.00227	0.004166	–0.00106	3
16	6039.5	0.09253	0.023716	0.046852	0.006475	5
17	2246.722	–0.1993	0.00721	0.01381	0.0119	4
18	2541.067	0.033709	0.012709	0.01933	0.00171	5
19	886.2857	0.064396	0.037233	-0.03843	0.046007	4
20	4014.129	0.10652	0.029349	0.01161	0.00329	5
21	1064.891	0.224968	0.078325	0.042095	0.05366	5
22	4000.595	0.02634	0.012494	0.029305	0.00389	5
23	3161.52	0.035655	0.013799	0.01303	0.00114	5
24	2433.032	0.03058	0.010442	0.023535	0.003071	5
25	3065.071	0.106235	–0.00063	0.023153	0.010648	4
26	1942.01	0.104033	0.042007	0.09971	0.01077	5
27	1702.48	0.235912	0.011101	0.102586	0.00104	5
28	1302.133	0.123355	0.00984	0.02057	0.001049	5
29	1663.357	0.134442	0.010629	0.0662	0.01683	5
30	5970.927	0.026662	0.009211	0.03806	0.015	5

Copyright © 2012 SciRes.

an almost 100% decision factor was achieved for all samples except for the cases in which the cancer grades were Stage I (where a 50% decision factor was still achieved). **Table 2** presents the decision factors using the voting algorithm. The results show that only four patients out of the total sample of 30 have erroneous trace elements and that this does not affect the overall decision. Hence, the performance of LIPS can be measured as 87%, while retaining 100% accuracy.

The LIPS technique is used to distinguish normal and malignant tumor cells from histological sections by measuring the concentrations of trace elements in real time. Previous studies have observed that the concentration of trace elements such as Zn, Cu, Fe, Mn, and Ca in normal and malignant cells vary significantly. For example, the concentration of calcium, iron, and zinc is larger in malignant cells in comparison with normal cells. The present study showed that the trace elements copper, iron, manganese, zinc, and calcium were all significantly higher in cancerous tissues than they were in their normal counterparts. However, the relevance of such elevated concentrations of these elements in breast cancer tissue remains a matter of conjecture.

Table 2. Decision factor using the voting algorithm.

Ser.	Stage	Decision Factor	Erroneous Elements	Decision
1	II	100%	-	Malignant
2	II	100%	-	Malignant
3	II	100%	-	Malignant
4	II	100%	-	Malignant
5	III	100%	-	Malignant
6	II	100%	-	Malignant
7	I	100%	-	Malignant
8	II	100%	-	Malignant
9	II	100%	-	Malignant
10	II	100%	-	Malignant
11	II	100%	-	Malignant
12	II	100%	-	Malignant
13	III	100%	-	Malignant
14	II	100%	Cu, Mn	Malignant
15	I	60%	-	Malignant
16	II	100%	Zn	Malignant
17	I	80%	-	Malignant
18	II	100%	Fe	Malignant
19	I	80%	-	Malignant
20	II	100%	-	Malignant
21	II	100%	-	Malignant
22	I	100%	-	Malignant
23	II	100%	-	Malignant
24	II	100%	-	Malignant
25	I	80%	Cu	Malignant
26	II	100%	-	Malignant
27	II	100%	-	Malignant
28	II	100%	-	Malignant
29	II	100%	-	Malignant
30	I	100%	-	Malignant

Evidence has suggested a relation between cellular activity/blood supply and the formation of micro calcifications in malignant breast tissues. It would seem reasonable, therefore, to assume that these elements might influence the carcinogenic process in malignant breast tissues. The present data raise the possibility that relatively high levels of copper, iron, zinc, manganese, and calcium in benign breast tissue may be associated with a modest increase in the risk of subsequent breast cancer. The results described herein indicated that a relatively high concentration of iron in benign breast tissue was positively associated with a subsequent breast cancer risk.

However, because we were unable to separate our measure of iron levels into free iron and iron in conjugation with enzymes, we could not differentiate between two possible explanations for this finding. The first explanation is that high levels of free iron in benign breast tissue might increase breast cancer risk because of the catalytic effect of iron in mutagenic radicals and the suppressant effect on the host's immune function. The second explanation is that both benign breast tissue and breast cancer cells might demand high levels of iron in order to sustain their power of proliferation given that iron is required for ribonucleotide reductase, a key enzyme in DNA synthesis [6,13].

The LIPS technique is a promising technology because of its simplicity, low degree of sample preparation, and low possibility of contamination. It is also minimally invasive, since a small-sized sample can generate good results. Further, because data are easily interpretable, skilled analysts are not required, while the necessary instruments are rugged and portable. This technique is similar to discharge/arc emission spectroscopy, in which elements are excited to a higher energy state by an electric discharge.

Many previous studies have indicated that metal ions can interact with nucleic acids to influence base-pairing and conformation. Such effects have been known to cause somatic mutations, a consequence of base-pairing errors or frame-shift mutations by deletion, leading to cellular transformation. For example, magnesium, manganese, and zinc are cofactors of many enzymes, especially RNA and DNA polymerases [14]. A comparison of trace element levels in normal and neoplastic human breast tissues has shown a relatively consistent and characteristic pattern of elevation for calcium, vanadium, copper, zinc, selenium,

Copyright © 2012 SciRes.

and rubidium [15].

4. Conclusions

The presented findings suggest an association between the elemental composition of breast tissues and the formation of breast particles. In other words, increases in the elemental concentrations and clustered calcifications in the breast may be related. Specifically, we can draw the following five conclusions about the LIPS technique:

- A simple and promising technique is capable of diagnosing malignant cells and tissues;
- It minimizes tissue preparation and human effort and error;
- It reduces the possibility of contamination as well as standard errors;
- It is minimally invasive, since a small-sized sample can generate good results;
- It gives online quantification for all trace elements in a tissue simultaneously.

Future work should include enhancing the voting algorithm in order to assess the degrees of deviation of malignant cells from normal cells and thus deduce the cancer grade. The enhancing mechanism could also include the study of building combined techniques that use more complex algorithms that could avail the advantage of LIPS results in confusing and fuzzy cases.

REFERENCES

[1] B. K. Abraham, C. Justenhoven, B. Pesch, *et al.*, "Investigation of Genetic Variants of Genes of the Hemochromatosis Pathway and Their Role in Breast Cancer," *Cancer Epidemiology Biomarkers and Prevention*, Vol. 14, 2005, pp. 1102-1107. doi:10.1158/1055-9965.EPI-05-0013

[2] B. Shane, A. Kumar, J. P. Singh and F. Y. Yueh, "Characterization of Malignant Tissue Cells by Laser-Induced Breakdown Spectroscopy," *Applied Optics*, Vol. 43, No. 28, 2004, pp. 5399-5403. doi:10.1364/AO.43.005399

[3] Z. Martin, S. Wullschleger, A. Palumbo, O. West, J. Smith, B. Evans, H. O'Neill and J. Woodward, "Applications of Laser Induced Breakdown Spectroscopy to Environmental and Biological Sample Analysis," *Proceedings of 54th Pittsburgh Conference & Exposition on Analytical Chemistry & Applied spectroscopy Pittcon* 2003 *Spectroscopy Society of Pittsburgh*, Orlando, 9-14 March 2003.

[4] J. Sariego, "Breast Cancer in the Young Patient," *The American Surgeon*, Vol. 76, No. 12, 2010, pp. 1397-1401.

[5] D. Saslow, J. Hannan, J. Osuch, M. H. Alciati, C. Baines, M. Barton, J. K. Bobo, C. Coleman, *et al.*, "Clinical Breast Examination: Practical Recommendations for Optimizing Performance and Reporting," *CA*: *A Cancer Journal for Clinicians*, Vol. 54, No. 6, 2004, pp. 327-344. doi:10.3322/canjclin.54.6.327

[6] Y. H. Yu, C. Liang and X. Z. Yuan, "Diagnostic Value of Vacuum-Assisted Breast Biopsy for Breast Carcinoma: A Meta-Analysis and Systematic Review," *Breast Cancer Research and Treatment*, Vol. 120, No. 2, 2010, pp. 469-479. doi:10.1007/s10549-010-0750-1

[7] Merck Manual, "Professional Edition, Section; Gynecology and Obstetrics, Ch. 253, Breast Cancer," Merck Sharp & Dohme Corp., Whitehouse Station, 2010.

[8] E. A. Ryan, M. J. Farquharson and D. M. Flinton, "The Use of Compton Scattering to Differentiate between Classifications of Normal and Diseased Breast Tissue," *Physics in Medicine and Biology*, Vol. 50, No. 14, 2005, pp. 3337-3348. doi:10.1088/0031-9155/50/14/010

[9] W. B. Lee, J. Y. Wu, Y. I. Lee and J. Sneddon, "Recent Applications of Laser-Induced Breakdown Spectroscopy: A Review of Material Approaches," *Applied Spectroscopy Review*, Vol. 39, No. 1, 2004, pp. 27-97. doi:10.1081/ASR-120028868

[10] J. G. Liehr and J. S. Jones, "Role of Iron in Estrogen-Induced Cancer," *Current Medicinal Chemistry*, Vol. 8, No. 7, 2001, pp. 839-849.

[11] W. O. John, "Trace Analysis by Infrared Spectroscopy," *Spectroscopy*, Vol. 14, No. 10, 1991, pp. 27-30.

[12] D. A. Cremers and L. J. Radziemski, "Handbook of Laser-Induced Breakdown Spectroscopy," John Wiley & Sons, Hoboken, 2006. doi:10.1002/0470093013

[13] D. A. Cremers and L. J. Radziemski, "Handbook of Laser-induced Breakdown Spectroscopy," John Wiley & Sons, Hoboken, 2007.

[14] I. B. Weinstein, "Current Concepts in Mechanisms of Clinical Carcinogenesis," *Bulletin of the New York Academy of Medicine*, Vol. 54, No. 4, 1978, pp. 366-383.

[15] S. L. Rizk and H. H. Sky-Peck, "Comparison between Concentrations of Trace Elements in Normal and Neoplastic Human Breast Tissue," *Cancer Research*, Vol. 44, No. 11, 1984, pp. 5390-5394.

Copyright © 2012 SciRes.

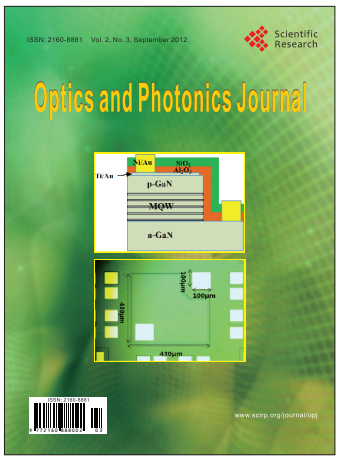

Call for Papers

Optics and Photonics Journal (OPJ)

ISSN: 2160-8881 (Print) 2160-889X (Online)
http://www.scirp.org/journal/opj

Optics and Photonics Journal (OPJ) is an international, specialized, English-language journal devoted to publication of original contributions in all areas of optics and photonics. The Journal disseminates new results in the theory, design, applications, fabrication, performance and characterization of optics and photonics materials including bio-related functions such as bio-optics, bio-photonics and also optoelectronics. The journal is also devoted to challenging and innovating methods and techniques related to the development of optics and photonics materials, characterization and applications.

Subject Coverage

The journal publishes original papers including but not limited to the following fields:

- All related associated materials and characterization techniques development
- Bio-induced optical materials and applications
- Bio-photonics
- Imaging processes
- Laser spectroscopy
- Light wave communication systems
- Nanophotonics
- Nonlinear optics
- Optical fibers
- Photonic crystals
- Quantum optics
- Waveguides

We are also interested in: 1) Short reports—2-5 page papers where an author can either present an idea with theoretical background but has not yet completed the research needed for a complete paper or preliminary data; 2) Book reviews—Comments and critiques.

Notes for Intending Authors

The journal publishes the highest quality original full articles, communications, notes, reviews, special issues and books, covering both the experimental and theoretical aspects including but not limited to the above materials, techniques and studies. Papers are acceptable provided they report important findings, novel insights or useful techniques within the scope of the journal. All manuscript must be prepared in English, and are subjected to a rigorous and fair peer-review process. Accepted papers will immediately appear online followed by prints in hard copy.

Website and E-Mail

http://www.scirp.org/journal/opj **E-mail: opj@scirp.org**

Optics and Photonics Journal, 2012, 2, 135-199
Published Online September 2012 in SciRes (http://www.scirp.org/journal/opj/).

TABLE OF CONTENTS

Volume 2 Number 3 **September 2012**

Copyright©2012 SciRes.